Materials Horizons: From Nature to Nanomaterials

Mrityunjay Doddamani
H. S. Bharath
Pavana Prabhakar
Suhasini Gururaja

3D Printing of Composites

Springer

Materials Horizons: From Nature to Nanomaterials

Series Editor

Vijay Kumar Thakur, School of Aerospace, Transport and Manufacturing, Cranfield University, Cranfield, UK

Materials are an indispensable part of human civilization since the inception of life on earth. With the passage of time, innumerable new materials have been explored as well as developed and the search for new innovative materials continues briskly. Keeping in mind the immense perspectives of various classes of materials, this series aims at providing a comprehensive collection of works across the breadth of materials research at cutting-edge interface of materials science with physics, chemistry, biology and engineering.

This series covers a galaxy of materials ranging from natural materials to nanomaterials. Some of the topics include but not limited to: biological materials, biomimetic materials, ceramics, composites, coatings, functional materials, glasses, inorganic materials, inorganic-organic hybrids, metals, membranes, magnetic materials, manufacturing of materials, nanomaterials, organic materials and pigments to name a few. The series provides most timely and comprehensive information on advanced synthesis, processing, characterization, manufacturing and applications in a broad range of interdisciplinary fields in science, engineering and technology.

This series accepts both authored and edited works, including textbooks, monographs, reference works, and professional books. The books in this series will provide a deep insight into the state-of-art of Materials Horizons and serve students, academic, government and industrial scientists involved in all aspects of materials research.

Review Process

The proposal for each volume is reviewed by the following:

1. Responsible (in-house) editor
2. One external subject expert
3. One of the editorial board members.

The chapters in each volume are individually reviewed single blind by expert reviewers and the volume editor.

Mrityunjay Doddamani · H. S. Bharath ·
Pavana Prabhakar · Suhasini Gururaja

3D Printing of Composites

Springer

Mrityunjay Doddamani
School of Mechanical and Materials Engineering
Indian Institute of Technology Mandi
Mandi, Himachal Pradesh, India

Pavana Prabhakar
Department of Mechanical, Civil and Environmental Engineering
University of Wisconsin–Madison
Madison, WI, USA

H. S. Bharath
Department of Mechanical Engineering
Siddaganga Institute of Technology
Tumakuru, Karnataka, India

Suhasini Gururaja
Department of Aerospace Engineering
Auburn University
Auburn, AL, USA

ISSN 2524-5384 ISSN 2524-5392 (electronic)
Materials Horizons: From Nature to Nanomaterials
ISBN 978-981-99-1729-7 ISBN 978-981-99-1730-3 (eBook)
https://doi.org/10.1007/978-981-99-1730-3

This Springer imprint is published by the registered company Springer Nature Singapore Pte Ltd.
The registered company address is: 152 Beach Road, #21-01/04 Gateway East, Singapore 189721, Singapore

Contents

About the Authors

Dr. Mrityunjay Doddamani is Associate Professor in the Department of Mechanical and Materials Engineering at the Indian Institute of Technology (IIT), Mandi, Himachal Pradesh, India, where he leads the Advanced Manufacturing Lab with research focused on 3D printing of lightweight composites. His research focus is on structure–property correlation of lightweight composites. His expertise includes advanced manufacturing and structural analysis of composites, understanding the effect of mechanical loading (static and dynamic) on the microstructure and mechanical properties, and failure analysis therein. Dr. Mrityunjay has published more than 75 journal articles in journals of international repute. He is featured in the top 2% scientist "Updated Science wide author database of standardized citation indicators" published by Elsevier 2021, 2022. Mrityunjay's research has been supported by various funding agencies in India and abroad. He is Recipient of Visiting Scientist Fellowship from the Office of Naval Research Global, Singapore. He is serving as Editorial Board Member of the *Materials Circular Economy Journal* by Springer-Nature. He is Inventor of two Indian patents.

Dr. H. S. Bharath is Assistant Professor at the Department of Mechanical Engineering, Siddaganga Institute of Technology, Tumakuru, Karnataka, India. He obtained his B.E. (Mechanical) and M.Tech. (Manufacturing Science and Engineering) from Visvesvaraya Technological University, Belagavi. He completed his Ph.D. at the National Institute of Technology Karnataka (NITK), Surathkal, Mangaluru. His major research interests include 3D printing, sandwich composites, and syntactic foams. He has published ten papers in reputed international journals.

Dr. Pavana Prabhakar is Charles G. Salmon Assistant Professor in the Departments of Mechanical Engineering and Civil and Environmental Engineering at the University of Wisconsin–Madison, where she leads the Manufacturing and Mechanics Lab (MaMeL) with research focused on advanced manufacturing and mechanics of lightweight composite materials. Her work involves conducting foundational

research on mechanics-based materials designs (computationally and experimentally) of composites and their fabrication by advancing relevant manufacturing techniques. Her research occurs at the intersection of solid mechanics, advanced manufacturing, materials science, and computational science. Her current and previous research involves extensive computational and experimental investigation of failure and damage in lightweight composites for structural applications. Her expertise includes micromechanical and structural analysis of composites using computational modeling, understanding the effect of extreme environments on the microstructure and mechanical properties, and failure analysis of structural materials using novel approaches. Dr. Prabhakar has published more than 30 journal articles in highly regarded journals. She received prestigious awards like NSF CAREER in 2021, ONR Young Investigator Program Award in 2019, and AFOSR Young Investigator Program Award in 2015. She also received the Destech Young Composites Research Award in 2019 and Ph.D. Research Scholarship Award in 2012, both from the American Society for Composites, for outstanding composite materials research focused on composite materials.

Dr. Suhasini Gururaja is Associate Professor in the Department of Aerospace Engineering at Auburn University, USA. Prof. Suhasini's research focuses on a major theme in advanced composites that correlates the material microstructure with its performance. Prof. Suhasini's research group—Advanced Materials and Processing Laboratory (AMPL)—explores issues at the intersection of composite microstructure, composite manufacturing, and structural integrity. She has achieved this through developing and leading intertwined research activities in damage development and progression, process modeling, and advanced manufacturing of composites. Before joining academia, Dr. Suhasini worked at GE Global Research (Bengaluru, India) and Boeing Commercial Airlines (Everett, WA, USA).

List of Figures

List of Tables

Chapter 1
Introduction

1.1 Composite Materials

New materials are necessitated by the increasing performance expectations of modern technological applications. It is challenging to meet much higher and more detailed quality criteria with single materials. As a result, composite materials are created by combining two or more conventional materials to generate a unique combination of qualities. According to the ASM Handbook [1], composite materials are a macroscopic mixture of two or more distinct materials with a visible interface. By decreasing the weight of the components, these materials improve the overall efficiency of the construction. Composite materials offer a wide range of applications in demanding sectors such as space vehicles, wind power generators, and rail transit due to their superior features, such as higher specific modulus, higher strength, and structural designability [2]. Composite materials are used extensively in airplanes; for example, composite materials account for approximately half of the Boeing 787's total weight. Furthermore, composite materials account for 53% of Airbus's current model, the A350 [3]. Composite features, such as directional and structural properties, can be modified to fulfill specific design needs. Numerous researchers are designing hybrid composites to attain better qualities by modifying the orientation of fibers, volume fraction, and other factors [4–7]. The matrix and reinforcing materials define the composite material [8]. The matrix phase is continuous, whereas the reinforcement phase might be either continuous or discontinuous. The interface between the matrix and reinforcement is the composite's third phase. Based on the matrix material, composites are categorized as Polymer matrix composites (PMC—250–310 °C), Ceramic matrix composites (CMC—1200–1400 °C), and Metal matrix composites (MMC-450–550 °C). In recent years, the rapid development of PMCs has been fueled by the increased need for lightweight materials [9] in all industries. PMCs are becoming a potential material for numerous structural and automotive applications due to their favorable mix of mechanical properties [10]. Because of their lower density, good thermal/electrical characteristics, improved chemical inertness, and easier manufacturing techniques, PMCs are widely employed in aircraft, electronics

M. Doddamani et al., *3D Printing of Composites*, Materials Horizons: From Nature to Nanomaterials, https://doi.org/10.1007/978-981-99-1730-3_1

engineering, and everyday consumer electronics. Figure 1.1 shows how composites are classified according to the type of reinforcements used [11]. The two most common types of polymers are thermoset and thermoplastic. Thermosetting polymers are insoluble and infusible during cure because the chains are rigidly connected with stronger covalent bonds. Phenolic, melamine, vinyl esters, vulcanized rubber, epoxy resin, and silicones are common thermoplastics in everyday life. Polyvinyl chloride, polybenzimidazole, polyethylene, acrylic, polypropylene, Teflon, and nylon are all examples of thermoplastics. PMCs are made up of a thermoplastic or thermosetting resin with fillers such as fibers, particles, and other materials. Due to the decreased density of the constituent elements, PMCs have good specific characteristics. Polymers have low strength and stiffness when compared to metals and ceramics. Nonetheless, reinforcing fillers can improve their characteristics. PMCs may also be easily molded into a range of forms and sizes because their processing does not require high pressure or temperature. In comparison with composites with other matrices, PMCs have fewer issues with reinforcement deterioration during manufacture. In addition, the equipment required for PMCs is less complicated.

Recent research in TPC manufacturing and joining techniques has encouraged its use by lowering production costs and enabling the effective assembly of basic components to create massive and intricate structures [12]. This is a significant achievement because one of the primary challenges until now has been that the fabrication of TPC is limited to fairly simple geometries due to the high resin melt viscosity of thermoplastic polymers and the fiber restrictions [13, 14]. Additionally, the high melt viscosity makes it difficult to saturate the fiber bundles and wet the fibers, hindering continuous-fiber TPC production. Continuous fiber arrangements are preferred for structural applications as they produce a significantly higher modulus and strength [15]. This is especially true for TPC, as thermoplastic polymers typically have lower strength and stiffness than thermoset ones due to their lower cross-link density [16]. In this situation, unidirectional prepreg tapes made of thin sheets of continuous reinforcement fibers impregnated with thermoplastic resin and obtained straight from the

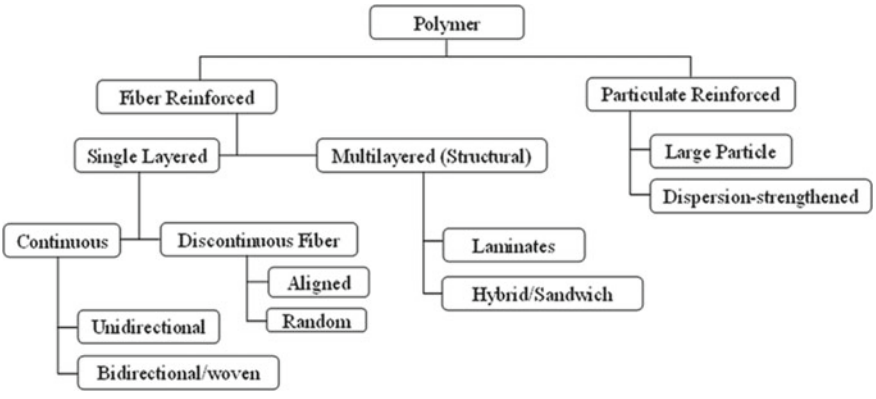

Fig. 1.1 Composites based on the nature of reinforcement

fiber roving and thermoplastic melt should be used to create TPC parts with continuous fiber reinforcement [17]. The capacity of TPC to melt is their main advantage. Due to a unique property of thermoplastic polymers, TPC may be "reprocessed," which makes them completely recyclable and well suited to joining and repairing processes involving local melting and re-consolidation employing fusion bonding techniques [18]. Given that it complies with the present environmental standards, many people view this feature as the next development in composite scientific materials [17, 19, 20]. Fusion bonding, which occurs at several interfaces, specifically between various yarns and plies of a laminate, is another technique utilized to make TPC pieces [21]. A huge heat-impacted zone would result from external volumetric heating using a hot instrument or infrared radiation because polymers often do not conduct heat well. Internal heat generation is hence more appropriate for joining and repairing TPC-damaged sections [22].

Syntactic foam (SF) composites are unquestionably superior to other traditional composites for weight savings without compromising structural performance, especially with a focus on lightweight materials. SFs are classified as a particular kind of structural composite. They have grown increasingly popular in recent years due to their higher specific strength, low moisture absorption, bending stiffness, and outstanding damping qualities. Because of its lower density, SF is an excellent material for space, marine, sports, and aeronautical applications [12]. SFs are porous lightweight composites used as buoyancy support systems in deep-sea scenarios [13]. They are used in airplanes, spacecraft, and ship structures, among other things [14]. Because of their larger porosity fractions, SFs can also be used to insulate gas and oil pipelines. Because of their reduced thermal expansion coefficient and dimensional integration at higher temperatures, SFs are also employed in electronic packaging, composite tooling, and thermoforming plug aids. The ability to customize the mechanical and thermal properties of SFs by careful material selection, hollow particle wall thickness, and particle volume % has aided in the rapid growth of these applications. Syntactic foams provide several advantages over typical particle and fiber composites, including the capacity to design and build according to the application's physical and mechanical property requirements [15].

1.1.1 Filler/Reinforcement

Behavioral requirements and intended usage influence filler choice. In the thermoplastic industry, organic and inorganic fillers are widely used [16–19]. Particulate reinforcements provide various advantages, like lower resin prices and more freedom in tailoring characteristics [20, 21]. Fillers can change surface, mechanical, magnetic, and electrical properties [22, 23]. Ceramics, mineral particles, metal, polymer, and various industrial by-products can all be used as reinforcements in polymers [24]. The commonly explored fillers are alumina [25], glasses [26], iron particulates [27], glass microballoons, and carbon fibers [28]. The target composite qualities play a significant role in filler selection. The form of the filler particles has a considerable

influence on the characteristics of the composite. Filler particles come in various forms, including spherical, blocks, cubical, flaky, and fibrous. Because of their regular shape, better crushing strength, low surface area-to-volume ratio, improved rheology, tightly controlled particle size, and control of surface qualities, spherical particulate fillers are more common than other types [29]. The usage of hollow particles such as glass microballoons (GMBs) and cenospheres (fly ash) in the production of high damage-tolerant and low density composites has increased dramatically in recent years [30–33]. The use of hollow fillers in the reinforcing matrix reduces the matrix volume percent, resulting in lightweight composite structures known as SFs. They have superior mechanical qualities and can generate complicated functioning parts that can replace expensive resin, reducing carbon emissions [34, 35]. Compared to manufactured glass microballoons, accessible fly ash cenospheres contain various surface flaws [36]. As a result, GMBs are the most widely used filler. These hollow GMB particle fillers can drastically reduce a matrix's weight and be used efficiently for weight-sensitive structures. GMBs are a free-flowing powder that originated in the 1960s from the manufacturing of solid glass beads. GMBs are commercially created in a variety of methods. Due to growing process technology and raw material supply in many places, GMBs are less expensive than polymeric ones [37]. GMBs are made in a vertical tube furnace that is fired with a propane-butane combination.

A powder combining glass and a porofor is sprayed at the tube's bottom. Porofor is a chemical blowing agent that inflates partially fused monolithic particles by producing gas at the glass melting point. The heated gas then propels the microspheres to the tube's top, where they are cooled and cleaned with water to remove any defective microspheres. After that, they are acid-treated to improve their chemical resistance and softening temperature [37]. Sodium silicate microballoons are made by mixing sodium silicate with ammonium pentaborate and spray-drying the mixture to create hollow microballoons [38]. The micrograph of as-received glass micro balloons is shown in Fig. 1.2.

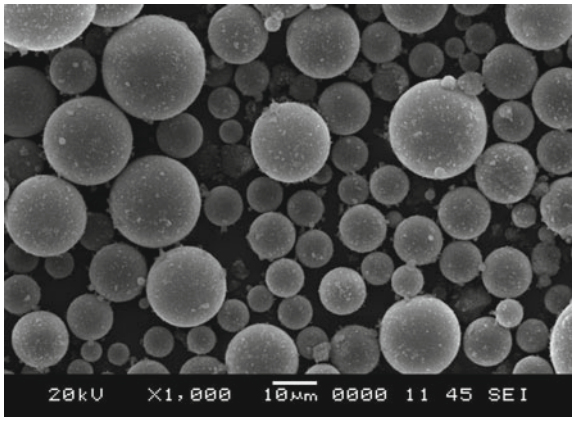

Fig. 1.2 GMB micrograph

GMBs are categorized into grades based on physical characteristics, including crushing strength, wall thickness, and density. The major factors for selecting hollow GMBs for a certain application are their strength, density, chemical stability, water resistance, and alkalinity. The material qualities of weight (density) and strength are critical for aeronautical, naval, and automotive components. GMBs are candidate fillers with promising behavior in manufacturing low-cost, lightweight thermoplastics without affecting the material's mechanical characteristics [23]. Developing newer and useful material systems using glass microballoons with near isotropy will be interesting.

1.1.2 Matrix

Polymers are materials made up of lengthy chains of molecules that are repeated. Monomers are repeating structural units bonded together by covalent bonds, and the process is called polymerization. Ductility, formability, and corrosion resistance are all desirable features of polymers [24]. Polymer characteristics are determined by the sort of molecules and their bonding. Continuous chilling and heating can be used to remold thermoplastic polymers (rubber, polyester, etc.) without affecting their properties [25]. While thermosetting polymers (epoxies, glass, and so on) are tough and long lasting, they remain stiff when heated unless they are charred [25]. A widely explored thermoplastics like PMMA [26], polylactide [27], ABS [28], PC [29], and PEA [30]. Thermoplastics are utilized for semi-structural and many functional applications, as they exhibit processing flexibility through different routes and are environmentally friendly. Plastics that can efficiently substitute metals like aluminum in small devices and structures with limited mechanical qualities have been dubbed engineering plastics. Compared to traditional materials, engineering plastic is the primary source for manufacturing composites with enhanced stiffness, specific strength, atmospheric, and chemical inertness [31]. Polymer matrices are often employed in composite materials due to their inherent characteristics. The cost of PMCs can be reduced by reinforcing the plastic with low-cost fillers like hollow GMBs. Plastic demand grew in India because of the widespread usage of plastic products in daily life. Grocery bags, soda and water bottles, cloth fabrics, tablets, computers, food containers, automotive components, and toys are all made of polymers. In 1997, India's estimated per capita plastic usage was 0.800 kg, one of Asia's lowest usages [32–35]. In the year 2000 A.D., the estimated demand was 2.16 kg/capita [36]. Because of economic liberalization, India has seen an upsurge in plastic usage since 1991. India's plastic use has increased from 0.85 million tons in 1990–91 to 1.79 million tons in 1995–96. Demand for commodity plastics is growing at 15% per year. The overall capacity to produce polyvinyl chloride (PVC), polystyrene (PS), polypropylene (PP), and polyethylene (PE) was 1.39 million mega tons (MMT) in 1995, according to the All-India Plastic Manufacturers Association, with demand increasing to 1.8–1.9 million mega tons in 1996–97. According to Plastindia reports, this is split into three major sectors: infrastructure, which accounts for

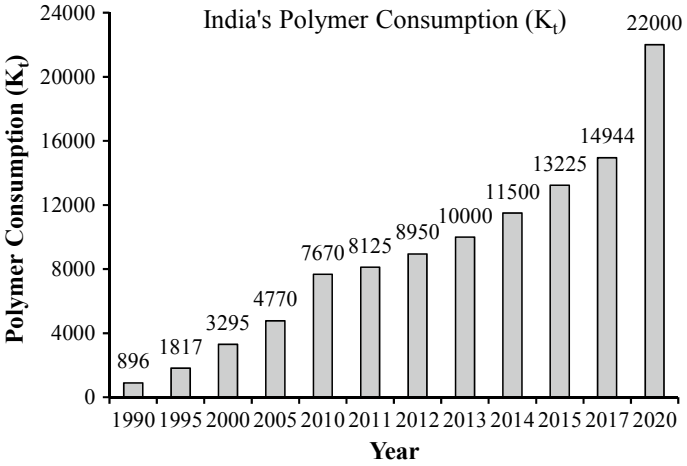

Fig. 1.3 Polymer consumption in India

30% of the total and includes bridges, buildings, electricity, roads, and telecommunications; packaging, which accounts for 25% of the total; and water and agriculture, which accounts for 24% [37]. Figure 1.3 depicts India's polymer consumption in kilo tons (Kt). Polymers used in packaging account for about half of this consumption.

Containing the present pace of plastic use, thermoplastic syntactic foam composites with fillers like hollow GMBs can help with plastic management and environmental concerns. When a matrix is reinforced with fillers, the function of the interface between them and any associated compatibility issues must also be addressed.

1.2 Syntactic Foams

Syntactic foams are particle composites developed in the 1960s and employed in marine structures because of their inherent buoyancy and low moisture absorption. Because of these foams, a wide variety of mechanical properties have been widely utilized in the core material for sandwich composites envisaged for lightweight applications [38]. Mixing hollow filler particles (micro balloons/microspheres/cenospheres) with the matrix material creates syntactic foams. Depending on the working conditions, various thermoplastic and thermosetting polymers are used as matrix resin [39]. Similarly, depending on availability, silicone, ceramic, or metal microballoons can be used [40]. Low heat conductivity and high specific strength characterize these foams [41]. For weight-sensitive structural applications, the buoyancy provided by SFs with higher compression strengths and modulus is critical [42]. One of the most significant benefits of such closed cellular materials is their capacity to form composites with the characteristics needed for

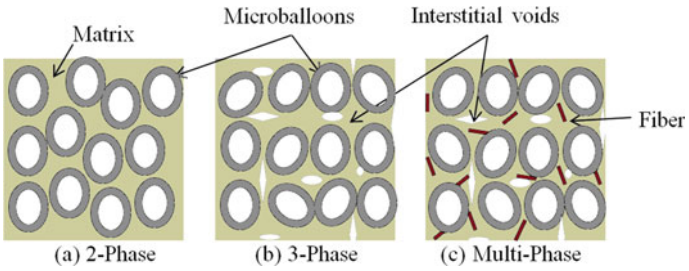

Fig. 1.4 Schematic representation of two, three, and multiphased syntactic foams

specific needs. There are two phases in the structure of SF: matrix resin and microballoons. Open-cell and closed-cell foams are the two forms of foam. Because of their low compressive modulus and strength, open-cell foams are cellular materials that are constantly limited [43]. Syntactic foams are closed-cell foams that have been created to address these concerns [44]. Nonetheless, some air gets trapped in the structure during the creation of SFs and is present as open-cell structural porosity. Voids are the imprisoned air that makes these foams three-phase structures (matrix, microballoons, and voids). When SFs are reinforced with fibers, they produce a multiphase structure. Figure 1.4 represents SF structure.

Closed-cell foams, also known as syntactic foams, offer more design flexibility in structural applications. As a result, tailor-made qualities for a variety of applications can be created by varying the vol. percent of such hollow filler in matrix material [45, 46]. The particle survivability in these lightweight foams and the processing procedures utilized to synthesize them is key to achieving these qualities [23, 47]. As a result, it is important to characterize these materials for mechanical behavior when they are created using modern manufacturing techniques like 3D printing.

1.2.1 Processing of Syntactic Foams

Physical, mechanical, and processing qualities are unique to each material system. A suitable manufacturing procedure must be chosen to turn the material into its final shape. In the twentieth century, the technologies for fabricating composite parts shifted from skilled labor operations to complex microprocessor systems that automatically run the equipment. Early researchers used manual lay-up techniques or spray-up in open molds to construct the finished sculpture by mixing raw materials and drying them at room temperature. The advantages of PMCs have pushed them into practically every other industry on the planet, from consumer goods to automotive and marine to fundamental structural components of planes and bridges. Material technology, design processes, and production procedures had to be developed quickly to keep up with the rapid increase in product applications [48]. To

reinforce hollow particles into the resin while generating SFs efficiently, the manufacturing route must be properly planned. It is feasible to prevent particle breakage and the inevitable result of increasing matrix porosity by stabilizing gas bubbles in the polymer matrix. Wetting homogenous reinforcement dispersion in the resin material, minimizing clusters without affecting the reinforcement, and avoiding hollow particle breaking are all requirements of the manufacturing procedures. Figure 1.5 [49] displays a typical reinforced SF production process.

This procedure uses a three-step mixing approach. In the first stage, the reinforcement is mixed with pure resin. After the reinforcement has been thoroughly combined and agitated until a slurry of constant viscosity has been achieved, hollow particles are inserted. The hardener or catalyst is added to the resin and mixed carefully in the final stage. The liquid is poured into molds and allowed to cure in accordance with the resin's specifications. The reinforcement is properly blended before hollow particles are added to limit the danger of hollow particle breakage during processing. Hand layup, autoclave, and oven cured are three open mold methods that are routinely employed on the factory floor. Closed mold methods include compression, injection, transfer, and heat stamping. Figure 1.6 depicts the fabrication possibilities for thermoplastics and thermosets.

Compression and injection molding are commonly used to manufacture Particulate Reinforced Thermoplastics, as seen in Fig. 1.6. Nonetheless, fused filament fabrication/fused deposition modeling (FFF/FDM)-based additive manufacturing has taken a giant leap recently to process PMCs.

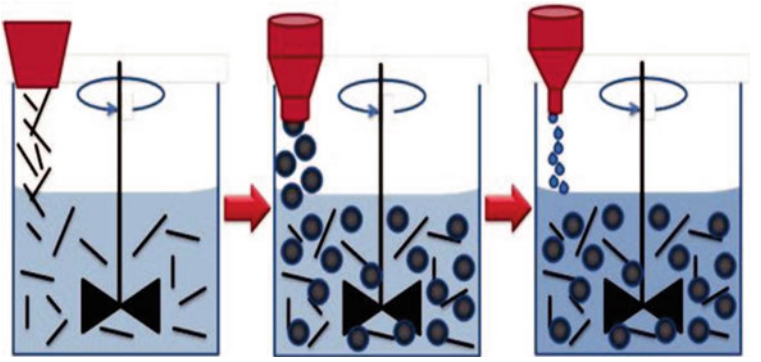

Fig. 1.5 Schematic of reinforced SF processing [50]

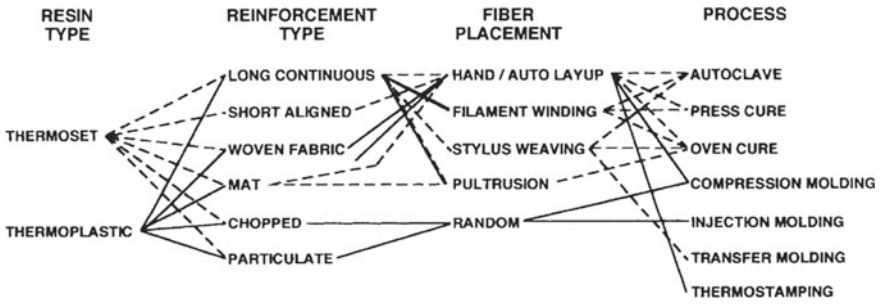

Fig. 1.6 Constituents of PMCs and manufacturing options

1.3 Sandwich Composites

Two thin, stiff face sheets are joined to either side of low density core material or structure Fig. 1.7 in a sandwich structure. The separation of the facings by a lightweight core significantly improves the second moment of area of the material cross-section. It thus increases the bending stiffness with only a little increase in weight. The "sandwich effect" is the name for this phenomenon. Sandwich composites are widely used in marine, civil, wind, aerospace, automobile, and other associated fields, owing to the several benefits over conventional material systems, like higher specific strengths, stiffnesses, higher damping response, excellent corrosion, and fatigue resistance [51–54]. The theory of sandwiches can be dated as earlier as 1849 CE [55]. During World War II, however, the possibility of sandwich design is recognized. The necessity for lightweight, high-strength, and damage-resistant constructions arose because of aerospace innovations wherein weight-saving potential without compromising the mechanical properties is crucial.

Sandwich composites are made up of a core, which is a thick lightweight slab, and two skins, which are thin and stiff face sheets [56]. The required qualities and

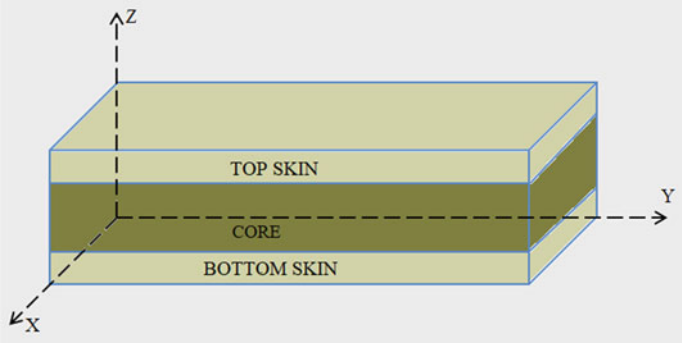

Fig. 1.7 The structure of a sandwich composite

associated applications determine the core and skin thicknesses. The materials used in sandwich composites are chosen based on the stress circumstances, cost, quality, availability of constituent materials, and functional needs. In aircraft constructions, multilayered carbon epoxy and graphite facings are widely employed, whereas vinyl esters or glass epoxy are commonly used in marine and civil system frames [51]. The damping and load-bearing capabilities of sandwiches are influenced by the thickness, design, and materials of the core-skins, as well as the material orientation [51]. The selection of appropriate filler and matrix materials, and volume/weight fractions of constituent elements makes them achieve tailored behavior. Depending on the application and performance requirements, a variety of materials can be employed as cores [57]. Lower density materials, such as closed- and open-cell foam morphologies, higher density cellular forms, such as honeycombs, and corrugated forms, such as trusses, are all common core materials. The core structure affects the contact between the skin and the core, resulting in the building of sandwiches based on the needs of the operating scenarios. In sandwich composites, the closer cell foamed core structures enable higher moduli, improved strength, decreased moisture absorptions, and impact, blast, and flexure resistance [58–61]. Tailor-made responses can be achieved based on shape, size, and pores composition. To construct sandwich composites, it is crucial to control the pore shape and size in the foams. Because of the need for high stiffness and strength in sandwiches, two different routes [62] of the closed-cell foams have been developed: first, sandwiching between stiff face sheets to increase flexural strengths [63, 64]. Secondly, porosity integrations using hollow microspheres provide effective reinforcing effects based on their thickness (wall) and volume %. As previously mentioned, these foams embedded with hollow balloons are known as SFs. Because of the wide variety of mechanical properties of these foams, they are utilized used as cores in sandwiches for lightweight applications [38, 65, 66]. Nonetheless, the freedom of sandwich processing is not effectively exploited [58]. To date, only a very few standard configurations, such as honeycomb [67–69], BCC lattice [70], pyramidal lattices, square honeycombs, tetrahedral lattices [71], and diamond honeycombs [72], are being synthesized using conventional approaches of manufacturing. Due to production constraints, traditional sandwich production procedures are limited to simple geometries [73]. To handle severe stresses under impact conditions, elaborate geometrical sandwich patterns are required. Traditional production, multistage production, and tooling present obstacles in creating functionally integrated complex-shaped sandwiches. Furthermore, the standard manufacturing procedure needs a complex and expensive bonding process that comprises adhesive joining of the skin and core generated separately [74–76]. The interfaces between the skin and the core are critical for load transfer. Sandwiches become weak across the skin–core interfaces due to parent material's absence and differential pressures acting across the interface bonding, resulting in debonding/delamination and shear failures. Sandwiches' inherent failing can thus be eliminated if they are developed as a concurrent material system. This can be accomplished efficiently by using a good processing technology, such as 3D printing, to create a sandwich structure at the same time (skin–core-skin).

1.4 Additive Manufacturing (AM)

For global competitiveness, advanced manufacturing is driven by rapid expansion and advances in the manufacturing area. The development of novel materials and manufacturing techniques to manufacture next-generation items is critical to any country's economic prosperity. In comparison with traditional processing technologies, AM technology has grown significantly in recent years, steadily changing the focus away from traditional application methods and attracting attention to boost manufacturing sector competitiveness [52, 77]. AM allows for more customization options, increased productivity, greater flexibility, and lower production costs. AM also eliminates traditional part geometry limitations by swiftly manufacturing highly complicated components with less material and resources. It removes the need for expensive tooling and complicated drawings, cutting the time from concept to commercialization in half, and enhances the renewable energy economy by lowering energy intensity, resulting in a paradigm change in the design-to-manufacture process. Traditional reductive processes, such as milling or lathing, remove material to create a component, whereas AM creates a part by adding material progressively. AM allows for rapid prototyping and, in some cases, can be utilized directly in manufacturing for small-scale production. It also allows for low-volume output to be produced quickly and cost-effectively, as well as adaptive enhancements. This might be highly valuable for designers, as a physical sense of an object can reveal details difficult to discern from 3D representations on a computer screen. Because of the rapid evolution of AM's methodology, its uses are no longer limited to rapid prototyping. Rapid advancements in additive manufacturing techniques have propelled them beyond prototypes to actual product development in the aerospace, automotive, and medical industries [78]. The AM/3DP process chain is depicted in Fig. 1.8 [79]. Individual ideas/imaginations are transformed into concrete CAD models utilizing Computer-Aided Design, Computer Tomographic (CT) scanning, or 3D laser scanning processes. These are then optimized by software to a final shape and size. The stereolithography (STL)/Standard Tessellation Language format is used to save the CAD model. The STL file is loaded into slicing software, which acts as a conduit between the computer and the 3D printer. It also enables the setting of various printing process parameters, the generation of structure geometry, and the slicing of the CAD model into thin layers. The machine's operating system runs the G-code created by the software, which describes each layer's printing route. The printing process begins with applying the first layer to the bed/substrate, followed by depositing the next layer to the previous layer as per the model description. The procedure is repeated until the complete model has been printed. After the part has been completely printed, it is taken from the bed or substrate and subjected to additional post-processing procedures such as priming and painting. Various AM techniques have distinct methods for separating the support structure from the actual component due to variances in method and materials employed. Even though unique AM techniques differ substantially, they all have one thing in common: all fabricated parts are created using a fast, precise, fully automated, and customizable manner directly from a 3D CAD model.

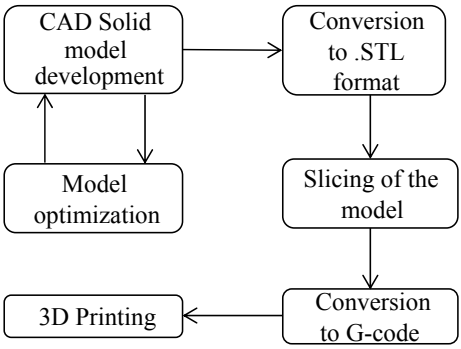

Fig. 1.8 Workflow of AM/3DP

There is a plethora of AM systems available in the business market right now. The ASTM F42 committee divides AM processes into seven categories, as shown in Table 1.1. Fused Deposition Modeling (FDM) or fused filament fabrication (FFF), Stereolithography (SLA), Selective Laser Sintering (SLS), and Multi-jet/Poly-jet modeling (MJM) are four of the seven AM classes that are frequently utilized in the processing of polymers [80]. The amount of area required, the cost, the layer heights, and the materials utilized vary among these systems. The FFF approach is an AM process in the advanced manufacturing domain that can create items with no geometric limits and has several advantages, including lower costs, a wider range of materials, minimal environmental impact, and simple post-processing [81–83]. S. Scott Crump invented the FFF technology in the late 1980s, and Stratasys Inc., which he cofounded, commercialized it in 1990 [84].

In the recent past, studies on fused filament fabricated product characteristics such as build quality [86–89], dimensional quality [90–92], and surface roughness [90, 93–98]. Using 3DP processes, the FFF process is the most frequent technique to reduce lead times. The FFF approach is depicted schematically in Fig. 1.9.

The present study uses FFF technology to 3D print a thermoplastic-based syntactic foam core and sandwich composite. In weight-sensitive components, the composites 3DP are based on polymer matrices exhibiting higher specific stiffnesses [99]. FFF is a layer deposition of material addition method that creates 3D things by digitally slicing computationally planned virtual 3D objects to generate the desired printing path [85, 100]. Slicing software includes KISSlicer, Simplify 3D, and Slice3r. This data is used by the slicing program to generate G-code, which is subsequently executed by the machine. After being unwound from a spool, the filaments are pulled through electromechanical feeding units. The heat from the heated nozzle would be sufficient to melt the plastic. The semi-molten material is deposited in raster's/roads on the bed, and the entire component is printed layer by layer as time passes [101]. The adherence of the polymer layers deposited, their liquid–solid conversion, and the ease with which prints can be removed post-printing are all crucial factors for generating defect-free components in the FFF process. Due to differential shrinkage (volumetric), solidification, crystallization, and adhesion at the skin–core interfaces, printing multimaterial systems at the same time, such

Table 1.1 AM process classifications [85]

Process type	Brief description	Related technology	Companies	Materials
Binder jetting	Liquid bonding agent is selectively deposited to join powder material	Powder Bed and Inkjet Head (PBIH), plaster-based 3D printing	3D system (USA), ExOne (USA)	Polymer, foundry sand, metals
Direct energy deposition	Focused thermal energy to fuse material by melting as the material is being deposited	Laser Metal Deposition (LMD)	Optomec (USA), POM (USA)	Metals
Material extrusion	Material is selectively dispensed through a nozzle or orifice	Fused Filament Fabrication (FFF)/Fused Deposition Modeling (FDM)	Stratasys (Israel), Bits from bytes	Polymers
Material jetting	Droplets of build material are selectively deposited	Multi-Jet Modeling (MJM)	Objet (Israel), 3D system (USA)	Polymer, waxes
Powder bed fusion	Thermal energy selectively fuses regions of powder bed	Electron Beam Melting (EBM), Selective Laser Sintering (SLS), Selective Heat, Sintering (SHS), and Direct Metal Laser Sintering (DMLS)	EOS (Germany), 3Dsystem (US), Arcam (Sweden)	Metals, polymers
Sheet lamination	Sheets of material are bonded to form an object	Laminated Object Manufacturing, Ultrasonic Consolidation (UC)	Fabrisonic (USA), Mcor (Ireland)	Paper, metals
Vat photo polymerization	Liquid photopolymer in a vat is selectively cured by light-activated polymerization	Stereolithography (SLA), Digital Light Processing (DLP)	3D system (USA), EnvisionTEC (Germany)	Photopolymers

as in sandwiches (core and skin), is difficult. The fused filament fabrication-based three-dimensional printing can be used to actualize sandwich production in a single step. The 3DP process may be used to print sandwich composites in which the skin and core feedstock filaments are fed separately by utilizing a 3D printer for layered and controlled deposition, allowing for good skin and core bonding. Developing

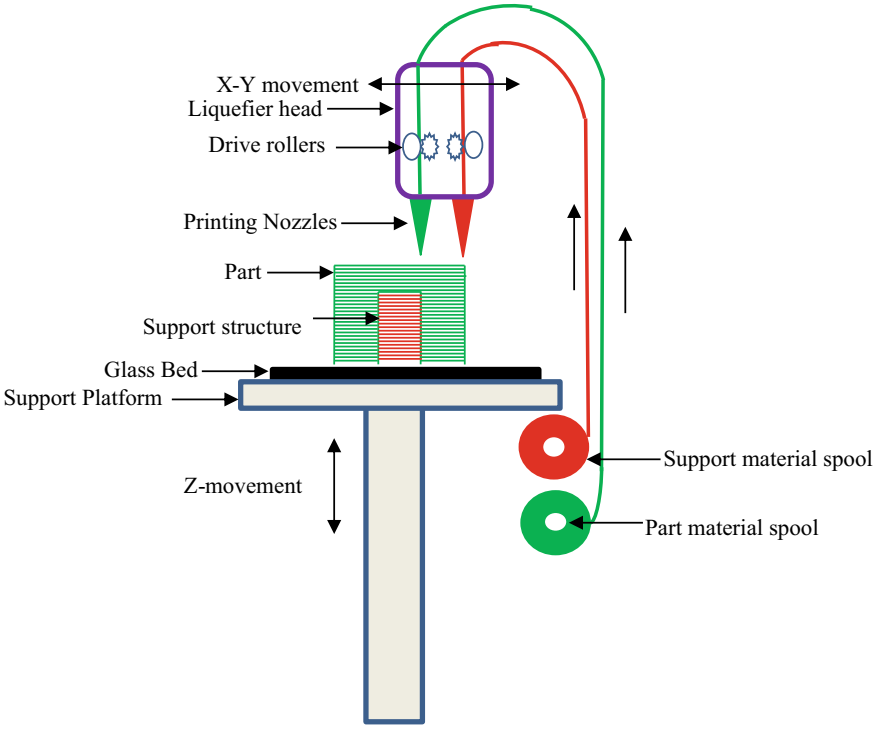

Fig. 1.9 Schematic of FFF process

the lightweight closed-cell foam filament with minimized particle breakage shall enhance the specific response in prints for weight-critical regimes like nose cones for autonomous underwater modules or even 3DP the entire tubular designed body with all the internal structures details at once. If produced through 3D printing, automotive and aerospace components with no connections (integrated components) can provide structural integrity while improving performance. In a marine environment, pressurization/depressurization causes foam fracture. Hence, adhesive junctions are the weakest elements in the structure. Foams with 3DP can remove adhesive bonding between several blocks, making them suitable for deep-sea applications. The ever-demanding need for automotive, marine, and aerospace functional components is to make complex shapes and contours without the use of adhesives, foamed printing, and the production of specific weight-sensitive filaments. Most AM activities use polymers and metal systems as input feed materials due to numerous material and processing problems, while SF filaments are still in their infancy. There has been very little research and development into 3D printing GMB-based SF core and sandwich composites, and no data on the characteristics of sandwich composites fabricated all at once has been reported (skin–core-skin). Novel material compositions with appropriate properties and processing parameters must be devised and optimized for AM of lightweight components using the 3DP technology. This book chapter addresses

these concerns and lays the groundwork for the use of additive manufacturing to create SF core and sandwich composites. The proposed technology in this paper can be directly implemented or used by the 3D printing industry to create sophisticated integrated parts that do not require joints or adhesive bonding. This research aims to find ways to reduce costs and increase efficiency by implementing large-scale AM systems. The goal of the project was to assist POLYMER INDUSTRIES that make high density polyethylene (HDPE) components with injection molding machines that require expensive equipment. HDPE is reinforced with GMBs to create a cost-effective yet relatively pricey matrix for developing SF filament in widely available 3D printers. The recent research effectively proved the development of lightweight feedstock filament, expanding the material options accessible for commercially available 3D printers. The SF core and their sandwiches are 3D printed successfully, all at one go (concurrently), with no flaws. Mechanical assessment of filaments and 3D printed samples is performed to determine their adaptability and feasibility for 3DP in weight-sensitive applications.

1.5 Issues for 3D Printable Materials

The 3DP polymeric composites are commercially successful due to the relatively inexpensive printer. These thermoplastics can be combined with the right fillers to improve their mechanical qualities. Al2O3 [102], glass [103, 104], iron particle [105], fly ash cenospheres [104–108], carbon, and glass fiber [109] are a few of the fillers that are frequently employed in the manufacture of blends. These composite blends can produce prints with improved structural responsiveness. There are significant attempts being made to comprehend and evaluate the quality of the printed components by adjusting the various processing factors. The extruded polymeric strands adherence, deposited layers solidification with adequate raster diffusions, and component removal post-printing are the main requirements for creating goods with no defects in the FFF-based 3DP. However, because of differential volumetric contraction and adhesion difficulties, realizing the 3D printed semi-crystalline thermoplastic sandwich composite all in one go is quite a challenging task. The realization of seamlessly connected components can be greatly improved with the help of a developing technology called composite printing, which also significantly shortens the production lead time [110]. Researchers are interested in 3D printing because of its design flexibility and because it opens new possibilities for composite development [111–114]. The incorporation of hollow microspheres into the matrix results in composite foams (also known as syntactic foams). One of the materials with low density and more damage-tolerant morphologies is foam [115–117]. Open- and closed-cell foams are two types of syntactic foams, often known as cellular materials. Open-cell foams have interconnected cells with higher porosity levels because of struts [117]. Open-cell foams have poor stiffness and strength, which reduces their load-bearing capacity. If the skin is wounded, the foam will absorb more moisture. As a result, sandwich architectures frequently use closed-cell/syntactic foams

as their core [38, 118–121]. Due to their superior load-bearing capacity and dimensionally and thermally stable design, synthetic foams have begun to take the role of conventional materials in automotive, marine, aerospace, and civil structures [122, 123]. By proper selection of the hollow particle type, the wall thickness, and the volume % of filler particles, these closed-cell foams can have specific features [45, 124, 125]. Syntactic foam is produced using a lot of hollow particles, such as carbon, glass, phenol, alumina, and silicon carbide. For a particular application, these microspheres are tailored to achieve a defined range of wall thickness diameters. Glass micro balloons (GMBs), which are hollow glass particles, are frequently used as fillers in SFs and are the fillers in the current study. Sandwich composites are unusual material groups made up of a lightweight core and often two thin, stiffer skins [126]. Low density, greater bending stiffnesses, damage-tolerant architecture, etc., are key sandwich properties. The right choice of core and peel makes sandwiches more flexible to a larger range of applications and various climatic scenarios. The choice of skin is essential since it will be in close touch with the load and the surrounding environment. Extrusion, expansion, and corrugation are used to create the core, but only for core designs with simpler geometrical patterns [127]. It is necessary to make development efforts toward 3DP because these traditional procedures do not permit geometrically complex integrated core fabrication [128–130]. Sandwich composites produced using traditional methods as opposed to 3D printed ones have weaknesses at the skin–core interface and cannot produce cores with intricate geometrical designs.

References

1. ASTM, Standard terminology for composite materials. D3878-18. ASTM International. West Conshohocken, PA, USA
2. Zhu F, Chou CC, Yang KH (2011) Shock enhancement effect of lightweight composite structures and materials. Compos B Eng 42(5):1202–1211
3. Tang X, Jian W, Huang J, Zhao F, Li C, Xiao X, Yao X, Luo S (2018) Spall damage of a Ta particle-reinforced metallic glass matrix composite under high strain rate loading. Mater Sci Eng, A 711:284–292
4. Gangil B, Kukshal V, Sharma A, Patnaik A, Kumar S (2019) Development of hybrid fiber reinforced functionally graded polymer composites for mechanical and wear analysis. AIP Conf Proc 2057(1):020059
5. Hemath M, Mavinkere Rangappa S, Kushvaha V, Dhakal HN, Siengchin S (2020) A comprehensive review on mechanical, electromagnetic radiation shielding, and thermal conductivity of fibers/inorganic fillers reinforced hybrid polymer composites. Polym Compos 41(10):3940–3965
6. Laishram R, Bisheshwar H, Shivakumar N, Amrutur B, Reddy T (2019) A study on the effects of fiber orientation on woven glass fiber composite structures. 2nd international conference on research in science, engineering and technology. Oxford, United Kingdowm, pp 23–34
7. Sachinkumar, Narendranath S, Chakradhar D (2020) Studies on microstructure and mechanical characteristics of as cast AA6061/SiC/fly ash hybrid AMCs produced by stir casting. Mater Today: Proc 20:A1–A5
8. Chawla KK (2001) Composite materials. Springer, New York

9. Matli PR, Krishnan AV, Manakari V, Parande G, Chua BW, Wong SCK, Lim CYH, Gupta M (2020) A new method to lightweight and improve strength to weight ratio of magnesium by creating a controlled defect. J Market Res 9(3):3664–3675
10. Benchekchou B, Coni M, Howarth H, White R (1998) Some aspects of vibration damping improvement in composite materials. Compos B Eng 29(6):809–817
11. Agarwal BD, Broutman LJ (1980) Analysis and performance of fiber composites. J Polym Sci: Polym Lett Ed 18(10):689–690
12. Ageorges C, Ye L (2002) Fusion bonding of polymer composites. Springer Science & Business Media
13. Tao W, Su X, Wang H, Zhang Z, Li H, Chen J (2019) Influence mechanism of welding time and energy director to the thermoplastic composite joints by ultrasonic welding. J Manuf Process 37:196–202
14. Ahmed TJ, Stavrov D, Bersee HEN, Beukers A (2006) Induction welding of thermoplastic composites—an overview. Compos A Appl Sci Manuf 37(10):1638–1651
15. Mallick P (2021) Thermoplastics and thermoplastic–matrix composites for lightweight automotive structures. Materials, design and manufacturing for lightweight vehicles. Elsevier, pp 187–228
16. Crosky A, Soatthiyanon N, Ruys D, Meatherall S, Potter S (2014) Thermoset matrix natural fibre-reinforced composites. Nat Fibre Compos:233–270
17. Marsh G (2014) Reinforced thermoplastics, the next wave? Reinf Plast 58(4):24–28
18. Villegas IF, Moser L, Yousefpour A, Mitschang P, Bersee HEN (2012) Process and performance evaluation of ultrasonic, induction and resistance welding of advanced thermoplastic composites. J Thermoplast Compos Mater 26(8):1007–1024
19. Schell JSU, Guilleminot J, Binetruy C, Krawczak P (2009) Computational and experimental analysis of fusion bonding in thermoplastic composites: influence of process parameters. J Mater Process Technol 209(11):5211–5219
20. Mathijsen D (2015) The black magic of carbon fiber reinforced thermoplastics. Reinf Plast 59(4):185–189
21. Bourban PE, Bernet N, Zanetto JE, Månson J-AE (2001) Material phenomena controlling rapid processing of thermoplastic composites. Compos A Appl Sci Manuf 32(8):1045–1057
22. Xiao X, Hoa SV, Street KN (1994) Repair of thermoplastic resin composites bt fusion bonding. Compos Bond 1227:30
23. Jayavardhan M, Kumar BB, Doddamani M, Singh AK, Zeltmann SE, Gupta N (2017) Development of glass microballoon/HDPE syntactic foams by compression molding. Compos B Eng 130:119–131
24. Srinivasan NK, Ramakrishnan SS (1983) The science of engineering materials. New Delhi, Oxford & IBH
25. Arzamasov B (1989) Material science. Mir Publishers, Moscow
26. Bourell D, Stucker B, Espalin D, Arcaute K, Rodriguez D, Medina F, Posner M, Wicker R (2010) Fused deposition modeling of patient-specific polymethylmethacrylate implants. Rapid Prototyping J 16(3):164–173
27. Spoerk M, Arbeiter F, Cajner H, Sapkota J, Holzer C (2017) Parametric optimization of intra- and inter-layer strengths in parts produced by extrusion-based additive manufacturing of poly (lactic acid). J Appl Polym Sci 134(41):45401
28. Dul S, Fambri L, Pegoretti A (2016) Fused deposition modelling with ABS–graphene nanocomposites. Compos A Appl Sci Manuf 85:181–191
29. Domingo-Espin, M, Puigoriol-Forcada JM, Garcia-Granada AA, Llumà J, Borros S, Reyes G (2015) Mechanical property characterization and simulation of fused deposition modeling Polycarbonate parts. Mater Des 83:670–677
30. Arivazhagan A, Saleem A, Masood S, Nikzad M, Jagadeesh K (2014) Study of dynamic mechanical properties of fused deposition modelling processed ULTEM material. Am J Eng Appl Sci 7:307–315
31. John B, Nair CR (2014) 13 - Syntactic foams. In: Dodiuk H, Goodman SH (eds) Handbook of thermoset plastics (Thied Edition). William Andrew Publishing, Boston, pp 511–554

32. Burgiel J, Butcher W, Halpern R, Oliver D, Tangora P (1994) Cost evaluation of automated and manual post-consumer plastic bottle sorting systems. Final report. Beck (RW), Orlando, FL (United States)
33. Burgueno R, Quagliata MJ, Mohanty AK, Mehta G, Drzal LT, Misra M (2004) Load-bearing natural fiber composite cellular beams and panels. Compos A Appl Sci Manuf 35(6):645–656
34. Esha S, Rajaram (1997) Plastic recycling in Bangalore—India. Urban Waste Expertise Programme (UWEP), CS-Plast India, p 8–10
35. Scott GG (2000) Polymers. Polym Degrad Stab 68:1–7
36. KSSPMA (1992) A guide to plastics. Bangalore
37. Nanavaty K (1997) Recycling of plastics: Indian experience. In: 3rd international plastics exhibition and conference on environment/recycling of plastics. New Delhi
38. Breunig P, Damodaran V, Shahapurkar K, Waddar S, Doddamani M, Jeyaraj P, Prabhakar P (2020) Dynamic impact behavior of syntactic foam core sandwich composites. J Compos Mater 54(4):535–547
39. Doddamani M, Kulkarni S (2011) Dynamic response of fly ash reinforced functionally graded rubber composite sandwiches-a Taguchi approach. Int J Eng Sci Technol 3(1):166–182
40. Gupta N, Pinisetty D, Shunmugasamy VC (2013) Reinforced polymer matrix syntactic foams: effect of nano and micro-scale reinforcement, 1 edn. SpringerBriefs in Materials. Springer, Cham
41. Gupta N, Maharsia R, Jerro HD (2005) Enhancement of energy absorption characteristics of hollow glass particle filled composites by rubber addition. Mater Sci Eng, A 395(1–2):233–240
42. Kulkarni S, Kumar SS, Kumar SS, Sinha UK, Shah B, Kumar KS, Mithran AS, Pillai KM (2012) Vibration reduction in indigenous wankel rotary combustion engine with structured layer damping. In: Proceedings of the 6th national symposium on rotor dynamics. Springer
43. Gupta N, Woldesenbet E (2004) Microballoon wall thickness effects on properties of syntactic foams. J Cell Plast 40(6):461–480
44. Puterman M, Narkis M, Kenig S (1980) Syntactic foams I. Preparation, structure and properties. J Cell Plast 16(4):223–229
45. Gupta N, Ricci W (2006) Comparison of compressive properties of layered syntactic foams having gradient in microballoon volume fraction and wall thickness. Mater Sci Eng, A 427(1–2):331–342
46. Jayavardhan M, Doddamani M (2018) Quasi-static compressive response of compression molded glass microballoon/HDPE syntactic foam. Compos B Eng 149:165–177
47. Kumar BB, Doddamani M, Zeltmann SE, Gupta N, Ramesh M, Ramakrishna S (2016) Processing of cenosphere/HDPE syntactic foams using an industrial scale polymer injection molding machine. Mater Des 92:414–423
48. Arza S (2012) Fillers, in encyclopedia of polymer science and technology, 4th edn. Wiley, New York
49. Labella M, Zeltmann SE, Shunmugasamy VC, Gupta N, Rohatgi PK (2014) Mechanical and thermal properties of fly ash/vinyl ester syntactic foams. Fuel 121:240–249
50. Gupta N, Pinisetty D, Shunmugasamy VC (2013) Processing and microstructure of syntactic foams. In: Reinforced polymer matrix syntactic foams. SpringerBriefs in Materials. Springer, Cham. https://doi.org/10.1007/978-3-319-01243-8_3
51. Birman V, Kardomateas GA (2018) Review of current trends in research and applications of sandwich structures. Compos B Eng 142:221–240
52. Mohamed OA, Masood SH, Bhowmik JL (2015) Optimization of fused deposition modeling process parameters: a review of current research and future prospects. Adv Manuf 3(1):42–53
53. Elamin M, Li B, Tan KT (2018) Impact damage of composite sandwich structures in arctic condition. Compos Struct 192:422–433
54. Thomsen OT (2009) Sandwich materials for wind turbine blades—present and future. J Sandwich Struct Mater 11(1):7–26
55. Noor AK, Burton WS, Bert CW (1996) Computational models for sandwich panels and shells. Appl Mech Rev 49(3):155–199

56. Gupta N, Zeltmann SE, Luong DD, Doddamani M (2018) Testing of foams. In: Schmauder S et al (eds) Handbook of mechanics of materials. Springer, Singapore, pp 1–40
57. Vinson J (1999) The behavior of sandwich structures of isotropic and composite materials, 1edn, p 363. CRC, Routledge
58. Doddamani MR, Kulkarni SM, Kishore (2011) Behavior of sandwich beams with functionally graded rubber core in three point bending. Polym Compos 32(10):1541–1551
59. Zhang J, Qin Q, Ai W, Li H, Wang T (2014) The failure behavior of geometrically asymmetric metal foam core sandwich beams under three-point bending. J Appl Mech 81(7):071008
60. Zhang J, Qin Q, Xiang C, Wang TJ (2016) Dynamic response of slender multilayer sandwich beams with metal foam cores subjected to low-velocity impact. Compos Struct 153:614–623
61. Zhang J, Zhou R, Wang M, Qin Q, Ye Y, Wang TJ (2018) Dynamic response of double-layer rectangular sandwich plates with metal foam cores subjected to blast loading. Int J Impact Eng 122:265–275
62. Yaseer Omar M, Xiang C, Gupta N, Strbik OM, Cho K (2015) Syntactic foam core metal matrix sandwich composite: compressive properties and strain rate effects. Mater Sci Eng, A 6431:56–168
63. Qin Q-H, Zhang J-X, Wang Z-J, Li H-M, Guo D (2014) Indentation of sandwich beams with metal foam core. Trans Nonferrous Metals Soc China 24(8):2440–2446
64. Rajaneesh A, Sridhar I, Rajendran S (2014) Relative performance of metal and polymeric foam sandwich plates under low velocity impact. Int J Impact Eng 65:126–136
65. Waddar S, Pitchaimani J, Doddamani M, Gupta N (2018) Buckling and free vibration behavior of cenosphere/epoxy syntactic foams under axial compressive loading. Mater Perform Charact 7(1):532–546
66. Waddar S, Pitchaimani J, Doddamani M, Barbero E (2019) Buckling and vibration behaviour of syntactic foam core sandwich beam with natural fiber composite facings under axial compressive loads. Compos B Eng 175:107133
67. Petras A (1999) Design of sandwich structures. University of Cambridge
68. Wang D (2009) Impact behavior and energy absorption of paper honeycomb sandwich panels. Int J Impact Eng 36(1):110–114
69. Yasui Y (2000) Dynamic axial crushing of multi-layer honeycomb panels and impact tensile behavior of the component members. Int J Impact Eng 24(6):659–671
70. Mines RAW, Tsopanos S, Shen Y, Hasan R, McKown ST (2013) Drop weight impact behaviour of sandwich panels with metallic micro lattice cores. Int J Impact Eng 60:120–132
71. Kooistra GW, Queheillalt DT, Wadley HNG (2008) Shear behavior of aluminum lattice truss sandwich panel structures. Mater Sci Eng, A 472(1):242–250
72. Wang A-J, McDowell D (2004) In-plane stiffness and yield strength of periodic metal honeycombs. J Eng Mater Technol 126(2):137–156
73. Dikshit V, Nagalingam AP, Goh GD, Agarwala S, Yeong WY, Wei J (2019) Quasi-static indentation analysis on three-dimensional printed continuous-fiber sandwich composites. J Sandwich Struct Mater 23(2):385–404
74. Jakobsen J, Bozhevolnaya E, Thomsen OT (2007) New peel stopper concept for sandwich structures. Compos Sci Technol 67(15):3378–3385
75. Karlsson KF, TomasÅström B (1997) Manufacturing and applications of structural sandwich components. Compos A Appl Sci Manuf 28(2):97–111
76. Shariyat M (2007) Thermal buckling analysis of rectangular composite plates with temperature-dependent properties based on a layerwise theory. Thin-Walled Struct 45(4):439–452
77. Rezayat H, Zhou W, Siriruk A, Penumadu D, Babu SS (2015) Structure–mechanical property relationship in fused deposition modelling. Mater Sci Technol 31(8):895–903
78. Vijayavenkataraman S, Fuh JY, Lu WF (2017) 3D printing and 3D bioprinting in pediatrics. Bioengineering 4(3):63
79. Yang C, Tian X, Li D, Cao Y, Zhao F, Shi C (2017) Influence of thermal processing conditions in 3D printing on the crystallinity and mechanical properties of PEEK material. J Mater Process Technol 248:1–7

80. Kazmer D (2017) 28—Three-dimensional printing of plastics. In: Kutz M (ed) Applied plastics engineering handbook, 2nd edn. William Andrew Publishing, p 617–634
81. Griffiths CA, Howarth J, De Almeida-Rowbotham G, Rees A (2016) A design of experiments approach to optimise tensile and notched bending properties of fused deposition modelling parts. Proc Inst Mech Eng, Part B: J Eng Manuf 230(8):1502–151
82. Rinaldi M, Ghidini T, Cecchini F, Brandao A, Nanni F (2018) Additive layer manufacturing of poly (ether ether ketone) via FDM. Compos B Eng 145:162–172
83. Wu P, Wang J, Wang X (2016) A critical review of the use of 3-D printing in the construction industry. Autom Constr 68:21–31
84. Perez B (2013) Printing pioneer Scott crump's kitchen experiment. South China Morning Post
85. Turner BN, Gold SA (2015) A review of melt extrusion additive manufacturing processes: II. Materials, dimensional accuracy, and surface roughness. Rapid Prototyping J 21(3):250–261
86. Caminero MA, Chacón JM, García-Moreno I, Reverte JM (2018) Interlaminar bonding performance of 3D printed continuous fibre reinforced thermoplastic composites using fused deposition modelling. Polym Test 68:415–423
87. Gordeev EG, Galushko AS, Ananikov VP (2018) Improvement of quality of 3D printed objects by elimination of microscopic structural defects in fused deposition modeling. PLoS ONE 13(6):e0198370
88. Narahara H, Shirahama Y, Koresawa H (2016) Improvement and evaluation of the interlaminar bonding strength of FDM parts by atmospheric-pressure plasma. Procedia CIRP 42:754–759
89. Yuan M, Bourell D (2016) Quality improvement of optically translucent parts manufactured from LS and SL. Rapid Prototyping J 22(1):87–96
90. Boschetto A, Bottini L, Veniali F (2016) Finishing of fused deposition modeling parts by CNC machining. Robot Comput-Integr Manuf 41:92–101
91. Chen H, Zhao YF (2016) Process parameters optimization for improving surface quality and manufacturing accuracy of binder jetting additive manufacturing process. Rapid Prototyping J 22(3):527–538
92. Prüß H, Vietor T (2015) Design for fiber-reinforced additive manufacturing. J Mech Des 137(11):111409
93. Durgun I, Ertan R (2014) Experimental investigation of FDM process for improvement of mechanical properties and production cost. Rapid Prototyping J 20(3):228–235
94. Lalehpour A, Barari A (2018) A more accurate analytical formulation of surface roughness in layer-based additive manufacturing to enhance the product's precision. Int J Adv Manuf Technol 96(9):3793–3804
95. Es-Said OS, Foyos J, Noorani R, Mendelson M, Marloth R, Pregger BA (2000) Effect of layer orientation on mechanical properties of rapid prototyped samples. Mater Manuf Processes 15(1):107–122
96. Hwang S, Reyes EI, Moon K-S, Rumpf RC, Kim NS (2015) Thermo-mechanical characterization of metal/polymer composite filaments and printing parameter study for fused deposition modeling in the 3D printing process. J Electron Mater 44(3):771–777
97. Torres J, Cotelo J, Karl J, Gordon AP (2015) Mechanical property optimization of FDM PLA in shear with multiple objectives. JOM 67(5):1183–1193
98. Tsouknidas A, Pantazopoulos M, Katsoulis I, Fasnakis D, Maropoulos S, Michailidis N (2016) Impact absorption capacity of 3D-printed components fabricated by fused deposition modelling. Mater Des 102:41–44
99. Patil B, Bharath Kumar BR, Doddamani M (2019) Compressive behavior of fly ash based 3D printed syntactic foam composite. Mater Lett 254:246–249
100. Turner BN, Strong R, Gold SA (2014) A review of melt extrusion additive manufacturing processes: I. Process design and modeling. Rapid Prototyping J 20(3):192–204
101. Dakshinamurthy D, Gupta S (2018) A study on the influence of process parameters on the viscoelastic properties of ABS components manufactured by FDM process. J Inst Eng (India): Ser C 99(2):133–138
102. Singh R, Singh S, Fraternali F (2016) Development of in-house composite wire based feed stock filaments of fused deposition modelling for wear-resistant materials and structures. Compos B Eng 98:244–249

103. Spoerk M, Arbeiter F, Raguž I, Weingrill G, Fischinger T, Traxler G, Schuschnigg S, Cardon L, Holzer C (2018) Polypropylene filled with glass spheres in extrusion-based additive manufacturing: effect of filler size and printing chamber temperature. Macromol Mater Eng 303(7):1800179
104. Singh AK, Saltonstall B, Patil B, Hoffmann N, Doddamani M, Gupta N (2018) Additive manufacturing of syntactic foams: part 2: specimen printing and mechanical property characterization. JOM 70(3):310–314
105. Masood S, Song W (2004) Development of new metal/polymer materials for rapid tooling using fused deposition modelling. Mater Des 25(7):587–594
106. Patil B, Kumar BB, Doddamani M (2019) Compressive behavior of fly ash based 3D printed syntactic foam composite. Mater Lett 254:246–249
107. Patil B, Kumar BB, Bontha S, Balla VK, Powar S, Kumar VH, Suresha S, Doddamani M (2019) Eco-friendly lightweight filament synthesis and mechanical characterization of additively manufactured closed cell foams. Compos Sci Technol 183:107816
108. Singh AK, Patil B, Hoffmann N, Saltonstall B, Doddamani M, Gupta N (2018) Additive manufacturing of syntactic foams: part 1: development, properties, and recycling potential of filaments. JOM 70(3):303–309
109. Brenken B, Barocio E, Favaloro A, Kunc V, Pipes RB (2018) Fused filament fabrication of fiber-reinforced polymers: a review. Addit Manuf 21:1–16
110. Hofmann DC, Kolodziejska J, Roberts S, Otis R, Dillon RP, Suh J-O, Liu Z-K, Borgonia J-P (2014) Compositionally graded metals: a new frontier of additive manufacturing. J Mater Res 29(17):1899–1910
111. Yap Y, Yeong W (2014) Additive manufacture of fashion and jewellery products: a mini review: this paper provides an insight into the future of 3D printing industries for fashion and jewellery products. Virtual Phys Prototyping 9(3):195–201
112. Lee JM, Zhang M, Yeong WY (2016) Characterization and evaluation of 3D printed microfluidic chip for cell processing. Microfluid Nanofluid 20(1):1–15
113. Yeong WY, Chua CK, Leong KF, Chandrasekaran M, Lee MW (2005) Development of scaffolds for tissue engineering using a 3D inkjet. In: Virtual modelling and rapid manufacturing: advanced research in virtual and rapid prototyping proceedings of 2nd international conference on advanced research in virtual and rapid prototyping, 28 Sep–1 Oct 2005. CRC Press, Leiria, Portugal
114. Garcia CD, Shahapurkar K, Doddamani M, Kumar GM, Prabhakar P (2018) Effect of arctic environment on flexural behavior of fly ash cenosphere reinforced epoxy syntactic foams. Compos B Eng 151:265–273
115. Shahapurkar K, Chavan VB, Doddamani M, Kumar GCM (2018) Influence of surface modification on wear behavior of fly ash cenosphere/epoxy syntactic foam. Wear 414–415:327–340
116. Ashrith H, Doddamani M, Gaitonde V, Gupta N (2018) Hole quality assessment in drilling of glass microballoon/epoxy syntactic foams. JOM 70(7):1289–1294
117. Doddamani M (2020) Influence of microballoon wall thickness on dynamic mechanical analysis of closed cell foams. Mater Res Express 6(12):125348
118. Doddamani M (2020) Dynamic mechanical analysis of 3D printed eco-friendly lightweight composite. Compos Commun 19:177–181
119. Doddamani M, Kulkarni S (2011) Behavior of sandwich beams with functionally graded rubber core in three point bending. Polym Compos 32(10):1541–1551
120. Gupta N, Zeltmann SE, Luong DD, Doddamani M (2018) 7—core materials for marine sandwich structures. Marine Compos Des Perform:187
121. Waddar S, Pitchaimani J, Doddamani M (2020) Effect of thermal loading on syntactic foam sandwich composite. Polym Compos 41(5):1774–1784
122. Mondal D, Jha N, Badkul A, Das S, Khedle R (2012) High temperature compressive deformation behaviour of aluminum syntactic foam. Mater Sci Eng, A 534:521–529
123. Orbulov IN (2013) Metal matrix syntactic foams produced by pressure infiltration—the effect of infiltration parameters. Mater Sci Eng, A 583:11–19

124. Taherishargh M, Sulong M, Belova I, Murch G, Fiedler T (2015) On the particle size effect in expanded perlite aluminium syntactic foam. Mater Des (1980–2015) 66:294–303
125. Yu M, Zhu P, Ma Y (2012) Experimental study and numerical prediction of tensile strength properties and failure modes of hollow spheres filled syntactic foams. Comput Mater Sci 63:232–243
126. Gibson LJ, Ashby MF (1999) Cellular solids: structure and properties. Cambridge university press
127. Bitzer T (1997) Honeycomb technology: materials, design, manufacturing, applications and testing. Springer Science & Business Media
128. Bonnard J-C (2004) Thermoplastic honeycomb core: an innovative continuous process. JEC composites 7:73–75
129. Zuhri M, Guan Z, Cantwell W (2014) The mechanical properties of natural fibre based honeycomb core materials. Compos B Eng 58:1–9
130. Rashed M, Ashraf M, Mines R, Hazell PJ (2016) Metallic microlattice materials: a current state of the art on manufacturing, mechanical properties and applications. Mater Des 95:518–533

Chapter 2
Material Systems and Methods

2.1 Constituents

To make lightweight thermoplastic syntactic foam composites, hollow glass microballoons (GMBs) are employed as fillers, and high density polyethylene (HDPE) is used as a matrix. The sections that follow go over these components in further depth.

2.1.1 Glass Microballoons

Hollow glass microballoons of grade iM30K are procured from 3 M Corporation, Singapore. GMBs are used under as-received conditions (Fig. 2.1a), without surface treatment. Table 2.1 shows properties of GMBs in as-received condition.

2.1.2 Matrix

IOCL-supplied HD50MA180 is used as the matrix. The resin is in granular form (~3 mm diameter). Table2.2 presents the details of the matrix used. HDPE (Fig. 2.1b) is also used in the as-received condition.

M. Doddamani et al., *3D Printing of Composites*, Materials Horizons: From Nature to Nanomaterials, https://doi.org/10.1007/978-981-99-1730-3_2

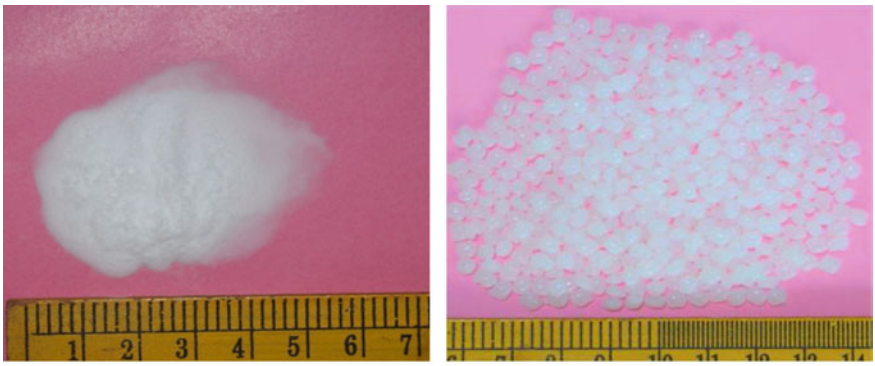

Fig. 2.1 As received **a** GMB in powder form and **b** HDPE granules [1]

Table 2.1 Properties of iM30K hollow glass microballoons[a]

Shape	Thin-walled hollow spheres		
Composition	Soda-lime-borosilicate glass		
Appearance	Off-white, powdery		
Particulars	Typical value	Unit	Test method
True density	0.60	(g/cc)	3 M QCM 14.24.1
Isostatic crush strength	27,000	(psi)	3 M QCM 14.1.8
Packing factor	63	%	–
Oil absorption	33.5	g oil/100 cc	ASTM D282–84
Softening point	600	°C	–
Flotation (density < 1.0 g/cc)	90	% (in volume)	3 M QCM 37.2
Volatile content (by weight)	Max. 0.5	%	3 M QCM 1.5.7
Alkalinity	< 0.5	Milliequivalents/gram	3 M QCM
pH (5% loading in water)	9.5	–	ASTM D3100—1982
Diameter (average)	18	microns	3 M QCM 193.0
Softening temperature	600	°C	–
Thermal conductivity	0.05–0.20	$Wm^{-1}\ K^{-1}$	@20 °C
Dielectric constant	1.2–1.9	–	@100 MHz
Minimum fractional survival	90	%	–

[a] Supplier data

2.2 Blend Preparation and Filament Extrusion

To combine HDPE and GMB, a 16CME SPL Brabender is utilized. The blender's speed is set at 10 rpm, whereas 160 °C temperature is maintained consistently, based

Table 2.2 Characteristics of HDPE grade HD50MA180*

Property	Test method	Typical value	Unit
Melt flow index (190^0C/2.16 kg)	ASTM D 1238	20.0	gm/10 min
Density @ 23°C	ASTM D 1505	0.950	gm/cm^3
Tensile strength at yield	ASTM D 638	22	MPa
Elongation at yield	ASTM D 638	12	%
Flexural modulus	ASTM D 790	750	MPa
Hardness	ASTM D 2240	55	Shore D
Vicat softening point	ASTM D 1525	124	°C

[a] As Provided by the supplier

on the results of pilot tests to avoid GMB breaking [2, 3]. As demonstrated in Fig. 2.2, the GMB and HDPE are plasticized in a Brabender. Figure 2.2b shows that mixing occurs in a restricted chamber with two screws. The material is fed into a feeder, which melts in the heating zone before being moved to twin screws/lobes (Fig. 2.2b). The pelletized blend of GMB/HDPE from Brabender is displayed in Fig. 2.2c. H20, H40, and H60 are the blend compositions, with H denoting the high density polyethylene and 20–60 denoting the volume percent of GMB present in the HDPE matrix. The GMB volume percent is fixed in the 20–60 range, as mechanical properties do not change significantly below 20%. Further, above 60% blend viscosity rises significantly [2]. Figure 2.3 presents a flow chart of the envisaged work as part of this work.

The stiffer GMB particles in HDPE can produce dimensionally stable prints. The 20, 40, and 60% GMBs by volume % are combined with an HDPE matrix before being extruded as filament form. A single-screw extruder is also used to extrude neat HDPE from their pellets. Filaments are extruded using a single-screw extruder. Barrel and die temperatures, screw, and take-off unit speeds affect the quality of extruded filament. Solid pellets are transformed into semi-solid and extruded from the die without material blockage at the proper barrel and die temperatures. The screw speed and take-off speed affect filament size. To create the filament with a diameter of 2.85 ± 0.05 mm, HDPE and foam pellets are fed into the extruder with a temperature profile of 145–150-155–145 °C from the feed to the die section, screw, and take-off unit speed, respectively. These factors include the HDPE melting temperature, the uniform and homogenous mixing of GMB in HDPE without breakage, the rheological behavior of blends, and the presence of porosity, if any, during extrusion, have been taken into account. For extruded H-H60 filaments, void % increases as GMB content increases. If these extra porosities are transferred to printed samples, they could create a three-phase syntactic foam that could improve damping properties. These filaments are fed into an FFF-based 3DP for the immediate fabrication of a sandwich with a syntactic foam core, HDPE skin, and GMB/HDPE core. The key factors affecting print quality are the extrusion temperature, nozzle and bed temperatures, print orientation, infill percentage, raster width, and layer height.

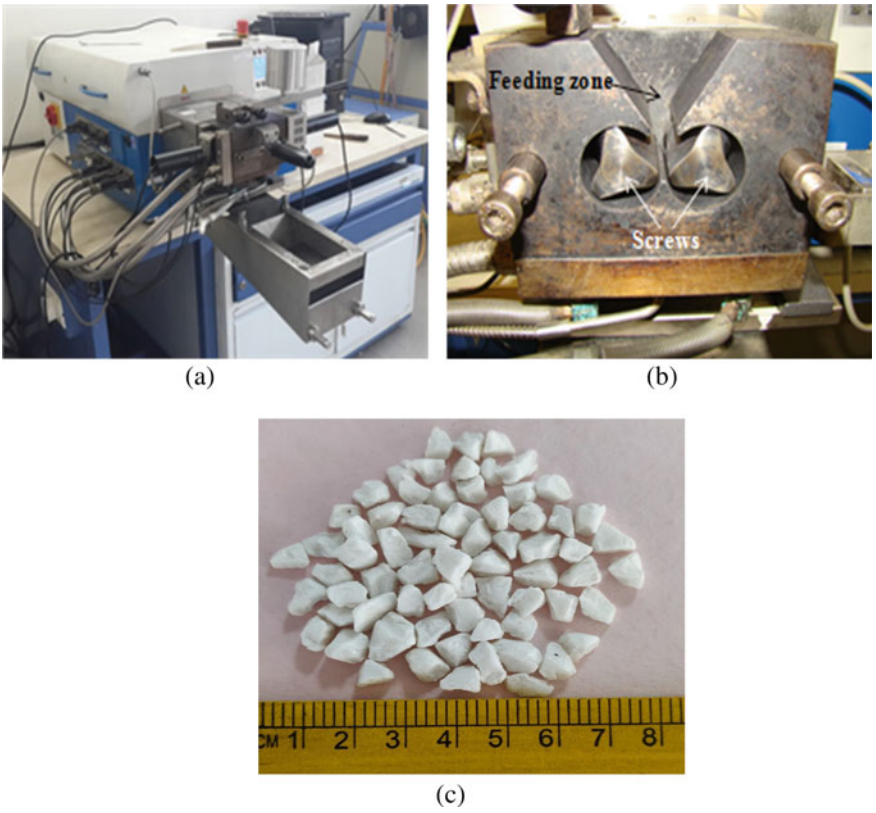

Fig. 2.2 **a** Plasticizer **b** mixing chamber and **c** GMB/HDPE blend [4]

2.3 Physical Properties

2.3.1 Density

According to ASTM D792-13 [5], experimental densities of all the samples are given by,

$$\rho_c = \rho_f V_f + \rho_m V_m \tag{2.1}$$

where ρ_c, V, f, and m are the density of composite, volume fraction, filler, and matrix, respectively. The theoretical density of sandwich composites is determined by,

$$\rho_{th} = V_s \rho_s + V_c \rho_c \tag{2.2}$$

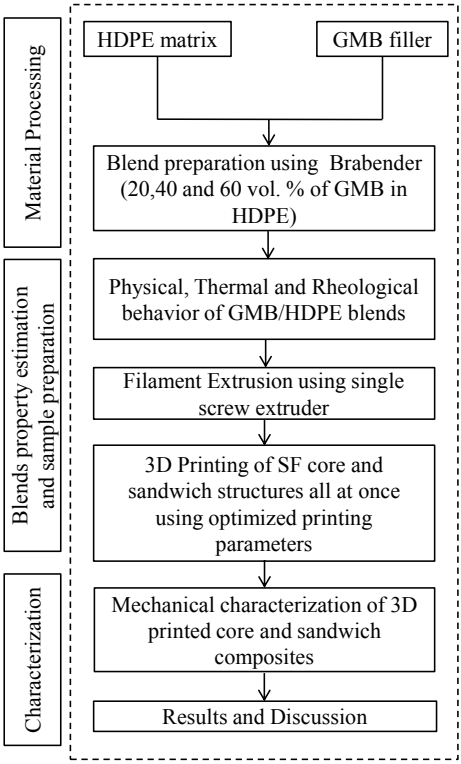

Fig. 2.3 Flow chart of the present study

where s and c are skin and core of sandwich composite. Furthermore, the difference in ρ^{th} (theoretical) and ρ^{exp} (experimental) density gives $\Delta_V\%$ (void), which is deduced as [6],

$$\Phi_V = \frac{\rho^{th} - \rho^{exp}}{\rho^{th}} \tag{2.3}$$

References

1. Bonthu D, Bharath HS, Gururaja S, Prabhakar P, Doddamani M (2020) 3D printing of syntactic foam cored sandwich composite. Composites Part C: Open Access, 3: p. 100068
2. Jayavardhan M, Kumar BB, Doddamani M, Singh AK, Zeltmann SE, Gupta N (2017) Development of glass microballoon/HDPE syntactic foams by compression molding. Compos B Eng 130:119–131
3. Jayavardhan M, Doddamani M (2018) Quasi-static compressive response of compression molded glass microballoon/HDPE syntactic foam. Compos B Eng 149:165–177
4. Bharath HS, Bonthu D, Prabhakar P, Doddamani M (2020) Three-dimensional printed lightweight composite foams. ACS Omega 5(35):22536–22550

5. ASTM, *Standard Test Methods for Density and Specific Gravity (Relative Density) of Plastics by Displacement*. D792–13, ASTM International: PA, USA
6. Gupta N, Woldesenbet E, Mensah P (2004) Compression properties of syntactic foams: effect of cenosphere radius ratio and specimen aspect ratio. Compos A Appl Sci Manuf 35(1):103–111

Chapter 3
Conventional Processing Routes

In this study, GMB/HDPE blend filler contents are made and tested for rheology and melt flow index (MFI). Tensile tests and differential scanning calorimetry (DSC) are used to analyze the extruded mix filaments. Lightweight filaments that have been extruded are then fed into a 3D printer, where the printed objects are examined using tests for DSC, coefficient of thermal expansion (CTE), rheology, flexural behavior, and tensile strength. In order to compare the GMB/HDPE composite foam results produced via 3D printing to other composite outcomes produced using traditional fabrication techniques, a property map is then created. Such a comparison serves as a compass for choosing materials in accordance with particular end-product specifications.

3.1 Polymers

3.1.1 Compression Molding

Compression molding (CM) is the oldest and most widely used process for molding plastic components into near-net form pieces [3]. Because of its simple process, compression molding has been a typical production method of polymer composites for a very long time. Initially used to fabricate thermoset polymers and rubber compounds, this technique is predominantly used in the automobile sector to create massive, thin, and durable parts. The lower portion of the heated mold, which typically covers approximately half of the mold surface area, is initially filled with the necessary proportion of raw material, known as a charge. The material is then steadily compressed as the top half of the mold quickly rises to the top of the charge. The strong pressure during mold closing causes the polymer to deform and fill the mold cavity. When the compressed charge has filled the hole, the mold is held closed while the pressure is kept constant to allow the material to cure and solidify. Finally, the hardened component is removed from the mold and cooled outside. It is a closed mold

M. Doddamani et al., *3D Printing of Composites*, Materials Horizons: From Nature to Nanomaterials, https://doi.org/10.1007/978-981-99-1730-3_3

technique that uses two matched metal molds, one of which is fixed and the other of which is moveable. Within the mold, a thermoplastic composite layup is introduced, which is preheated to a specific temperature depending on the constituent materials. Furthermore, pressure is delivered to the mold via a hydraulic system to form the desired shape. The curing occurs in the oven, where the pressure of mold is kept constant. In a compression molding process, a combination of heat and pressure results in little void formation and a good surface finish on the finished product. Complex and high-strength fiberglass reinforcements can be molded with CM. It is also possible to use unidirectional tapes, woven fabrics, a randomly oriented fiber sheet, or chopped strands in advanced composite thermoplastics. Compression molding is a more cost-effective solution than injection molding and stamping. For thermosets, the mold remains heated throughout the compression molding process. As soon as a molded component is evacuated, a new charge of molding powder should be supplied. Unlike thermosets, thermoplastics must be cooled before they harden. Compression-molded HDPE composites are investigated for impact and wear properties [4]. Compression molds are usually fabricated from hardened tool steels, like injection molds. To resist raw material abrasion and provide a good surface finish, a high level of hardness and polish are necessary. The production rate is relatively high, with a standard cycle time varying between 1 and 3 min depending on the size and thickness of the products because the polymers are typically treated below their melting temperatures. On the other side, the restricted raw material flow limits the geometric complexity of the produced pieces, and surface flaws like pitting and waviness may develop.

The mechanical properties of multi-walled carbon nanotube-reinforced HDPE/cenosphere sheets compression molded at 15 MPa pressure and 160 °C are investigated [5]. Deepthi and colleagues investigated the mechanical properties of HDPE reinforced with silicon nitride and nano clay. Compression molding is less efficient than injection molding regarding cycle time, part complexity, and yield volume.

3.1.2 Injection Molding

The most extensively used manufacturing technique for producing plastic parts is injection molding. It is also utilized to make a variety of sizes, designs, levels of complexity, and applications. A long screw is installed within a barrel, a hopper is used to send material in the form of pellets/granules into the barrel, and a heater is used to melt the material inside the barrel. With the help of a moving screw, the material inside the barrel is melted and pumped into the mold, where it cools and hardens into the finished product. The material is fed into the split mold using a sprue gate feeding mechanism, and the part is subsequently extracted from the mold. One of the most frequent thermoplastic production technologies is injection molding. It is viewed as a great alternative for bulk manufacture of polymer micro/nano-tailored surfaces due to its fast production rate, low material cost, and variety of material

options. Injection-molded items have superior thermal, acoustic, and mechanical qualities over their compression-molded equivalents. Thermoplastic materials like low and high density polyethylene are widely used in the injection molding process [1, 6]. Injection molding makes it possible to produce quality plastic parts in various shapes and geometries at a reasonable cost. Using these resins to manufacture SFs could result in weight savings in current applications and the development of novel material systems [2, 7]. The flexibility to use quick production industrial procedures is one of the advantages of using thermoplastic resins for SF components. On the other hand, current research has not used such widely used industrial production processes to create these SFs. Using such rapid production procedures, the cost of lightweight syntactic foam components can be decreased [8]. Physical and mechanical property study on cenosphere/HDPE-based syntactic foams developed using injection molding is carried out by [9]. Although this approach of producing fly as cenosphere/HDPE SFs using injection molding is successfully explained, the weight decrease is not accomplished due to greater particle failures during processing. Due to higher particle failures inside the matrix resin, mechanical characteristics are less influenced. The available research on thermoplastic syntactic foams normally produces high-quality SFs by processing materials in a laboratory under controlled conditions. On the other hand, material manufacturing at the industrial level will not be able to produce foams of the same grade. Though injection molding is a quick processing method, tooling is quite expensive (molds). 3D printing is an alternative to this, as it allows for more flexibility in the creation of complicated shapes. The number of low-cost additive manufacturing equipment accessible for home usage has exploded in recent years. The media's attention and interest have been drawn to additive manufacturing machines because of this. There has recently been a slew of low-cost desktop printers released, and the industry has sparked a wave of innovation.

Complex goods with precise dimensions can be produced with high yields using injection molding, and the three-dimensional shapes are made possible by integrating numerous voids. Flexible rubbers to stiff plastics can be used to create the parts, and the surfaces have highly repeatable surface details. High pressure in injection molding is the main drawback. Additionally, the stock temperature must be higher than the polymer's glass transition temperature to ensure flow, which could cause material degradation from heat exposure.

3.1.3 Blow Molding

Blow molding is most frequently employed to fabricate hollow plastic components, particularly plastic bottles, and containers. A wide variety of thermoplastics can be used in the molding process because the tube of the molten polymer is enlarged by airflow and then solidifies during the melt's cooling. The most common thermoplastics are polyethylene (PE), polypropylene (PP), polyvinylchloride (PVC), and polyethylene terephthalate (PET). As hydrophobic polymers, PE and PP exhibit high water barrier properties but cannot halt oxygen migration. On the other hand, PVC

and PET can serve as materials that operate as barriers against moisture but not against oxygen. Extrusion blow molding can be used to create large and relatively complex hollow objects. A die head extrudes a molten polymer tube vertically into an open mold. The head controls the tube size, and the melt expands and drops as it emerges from the extrusion die. As a result, the viscous material must be strong enough to maintain its shape and have consistent swell and sag characteristics. Extrusion should happen quickly as well. The mold is shut, and the tube bottom is pressed after it has reached the proper length. The material is then inflated to fill the mold's cavity using compressed air provided by the head. After blowing, the sections with large diameters will exhibit a thin wall in a straightforward tube with uniform wall thickness. In contrast, the ones with small diameters will exhibit a thick wall. Certain die changes can produce a tube with varied wall thickness throughout their length, enhancing the finished part's strength and wall thickness uniformity. Most of the cycle time is spent when the polymer makes contact with the mold surface and begins to cool and solidify under the force of the air. The finished item is ejected from the mold in the final stage.

3.2 Metals

Costs for all processes developing MMCs are still costly because MMC technology is currently barely out of the R&D stage. The matrix and reinforcement must be well bonded during manufacturing, and there must be no unfavorable interactions between the matrix and fiber. Primary and secondary processing techniques can be used in MMC production, albeit these divisions are not as clear-cut as they are with monolithic metals. Combining and consolidation operations are two subsets of primary processes first utilized to generate the material. Shape-changing or joining procedures are both examples of secondary processes. Net-shape procedures are crucial production processes, just like with ceramics. Due to the fact that MMCs are extremely abrasive and require diamond tools, machining MMCs is both difficult and expensive. In addition, given the high cost of the raw materials, it is preferable to decrease the amount of scrap generated during the machining process. The matrix's main job in composite materials is to distribute stress among the reinforcing fibers and shield them from mechanical harm. The strain at the break of a matrix material must be greater than the strain of the fibers it is retaining. The two most well-known production methods for metal matrix composites are in the liquid and solid states. The number and distribution of the reinforcing components, the composition of the matrix alloy, and the application are all significantly influenced by choice of the best technique. A metal matrix composite can be produced by including the reinforcing phase in the matrix. Although the composition and quantities of the components remain the same, different characteristic profiles can be obtained by modifying the manufacturing process, the finishing, and the form of the reinforcement components. Reinforcing particles are injected into a solid or liquid matrix as part of the materials' strengthening mechanisms, either via a powder metallurgy technique or a liquid metallurgical

route via casting or another. Fabrication methods for MMCs are classified into three main groups: liquid-state fabrication, solid-state fabrication, and in situ fabrication. To create metal matrix composites, a reinforcing phase is added to the matrix using one of the following methods: powder metallurgy processing, spray atomization and co-deposition, plasma spraying, stir casting, or squeeze casting. The most widely utilized liquid-state method for making MMCs is stir casting. It offers a reasonably equal dispersal of particles while being modest in action and cost-efficient. The most often used solid-state manufacturing process is powder metallurgy. Although more expensive than stir casting, it ensures homogeneous particle distribution. Due to the increased properties of metal matrix composite, such as strength-to-weight ratio, hardness, stiffness, wear resistance, abrasion resistance, and many more, its replacement of conventional materials is growing exponentially. MMCs' qualities can be tailored and tuned to match specific applications, which has led to an increase in their use in a variety of applications. Therefore, to manufacture MMCs and meet demand in various sectors, researchers are developing new, cutting-edge technologies such as continuous binder powder coating (CBPC), metal injection molding (MIM), and mechanical alloying.

References

1. Benchekchou B, Coni M, Howarth H, White R (1998) Some aspects of vibration damping improvement in composite materials. Compos B Eng 29(6):809–817
2. Gupta N, Woldesenbet E, Mensah P (2004) Compression properties of syntactic foams: effect of cenosphere radius ratio and specimen aspect ratio. Compos A Appl Sci Manuf 35(1):103–111
3. Manas C, Salil R (2006) Plastic Technology. Handbook. CRC Press, NewYork, pp 2–6
4. Chand N, Sharma P, Fahim M (2010) Correlation of mechanical and tribological properties of organosilane modified cenosphere filled high density polyethylene. Mater Sci Eng, A 527(21–22):5873–5878
5. Divya V, Khan MA, Rao BN, Sailaja R (2015) High density polyethylene/cenosphere composites reinforced with multi-walled carbon nanotubes: Mechanical, thermal and fire retardancy studies. Mater Des 65:377–386
6. Alkan C, Arslan M, Cici M, Kaya M, Aksoy M (1995) A study on the production of a new material from fly ash and polyethylene. Resour Conserv Recycl 13(3–4):147–154
7. Bunn P, Mottram J (1993) Manufacture and compression properties of syntactic foams. Composites 24(7):565–571
8. Shunmugasamy VC, Zeltmann SE, Gupta N, Strbik OM (2014) Compressive characterization of single porous SiC hollow particles. JOM 66(6):892–897
9. Bharath Kumar BR, Doddamani M, Zeltmann SE, Gupta N, Uzma, Gurupadu S, Sailaja RRN (2016) Effect of particle surface treatment and blending method on flexural properties of injection-molded cenosphere/HDPE syntactic foams. J Mater Sci 51(8):3793–3805

Chapter 4
3D Printing Approach

4.1 Blend Characterization

4.1.1 Melt Flow Index (MFI)

MFI estimates material flowability. Melt flow rate refers to the rate at which thermoplastics are extruded through an orifice at a specified temperature and load. ASTM D1238 is used to estimate MFI of H-H60 pellets by using Dynisco LMI5000 (Fig. 4.1). The MFI values are utilized for choosing the multiplier (flow rate) in 3D printer. The flow rate is varied based on the compositions avoiding the temperature variable.

MFI measures the flowability of a system. Due to filler resistance to polymer flow, increasing GMB concentration reduces MFI [1]. The MFI of neat HDPE is noted to be 17.94 gm/10 min, whereas H20 (13.77), H40 (8.12), and H60 (4.85) have exhibited a declining trend. MFI reduced by 23.29, 54.79, and 72.97%, respectively, whereas GMB increased by 20, 40, and 60% [1, 2]. Particularly for foams with larger filler loadings, reduced MFI should be properly investigated, either by boosting the printing temperature or increasing the print extrusion multiplier. To reduce warpage, the printing temperature is maintained between H and H60; as a result, the multiplier factor is adjusted for greater GMB%.

4.1.2 Rheological Study of GMB/HDPE Blends

The rheological characteristics investigation is necessary to understand how fillers influence manufacturing processes. The effect of filler on the rheology of the manufactured blends is examined using an Anton Paar MCR 502 rotational rheometer. For frequency and temperature sweep, specimens with a 25 mm dia. and thickness of 1 mm are employed. The frequency sweep is conducted at 0.1–10 Hz, 150 °C, and

M. Doddamani et al., *3D Printing of Composites*, Materials Horizons: From Nature to Nanomaterials, https://doi.org/10.1007/978-981-99-1730-3_4

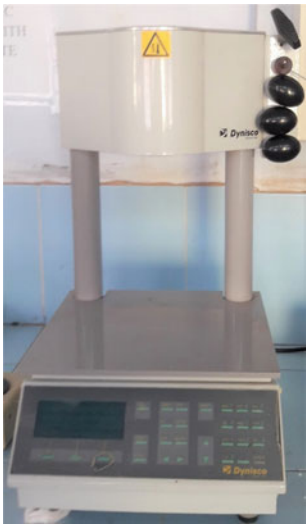

Fig. 4.1 Melt flow indexer (Dynisco LMI5000)

5% loading rate. The effect of frequency and GMB content on ɳ' (complex viscosities), G' (storage), and G" (loss moduli) is investigated. Similarly, in the temperature range of 130–150 °C, a temperature sweep is performed at 1 Hz. An average of five replicates is considered for all the experiments.

4.1.2.1 Frequency Sweep

Increased filler infusion raises the polymer's melt viscosity, which can be seen throughout the frequency sweep [3] (Fig. 4.2a). HDPE has a shear-thinning zone at higher frequencies. The restriction of polymer chain motions by GMBs causes H20–H60 to behave similarly, with a minor increase in complex viscosity (ɳ'). H60 has the highest of all the foams. Complex viscosities for H to H60 are 1080.52–636.75, 2045.4–1048, 2729.6–1324.2, and 4331.5–1701.6 Pa-s, respectively, at 0.1 and 50 rad/sec. SFs have larger storage moduli (G') than H (11,808 Pa at 50 rad/sec) due to the existence of a large number of stiff particulate matter (Fig. 4.2b). The G' of H20–H60 foams rises from 20,019 to 32,163 Pa. Due to the complete relaxation of polymer chains, high density polyethylene and H20 exhibit normal homopolymer-like terminal behavior at low frequencies [4]. The modulus of H20 is higher than that of pure HDPE. For H40 and H60, the Plateau region is seen less frequently, indicating viscoelasticity. For all samples, the loss modulus (G") rises with higher frequency and % filler amount (Fig. 4.2c). At 0.1 rad/sec, the loss moduli for H and H60 are 107.55–429.57 Pa, respectively, which is ~ 4 times higher for H60 than for H. The constrained matrix flow circumventing the stiff intact microspheres might lead to such a multifold rise in G".

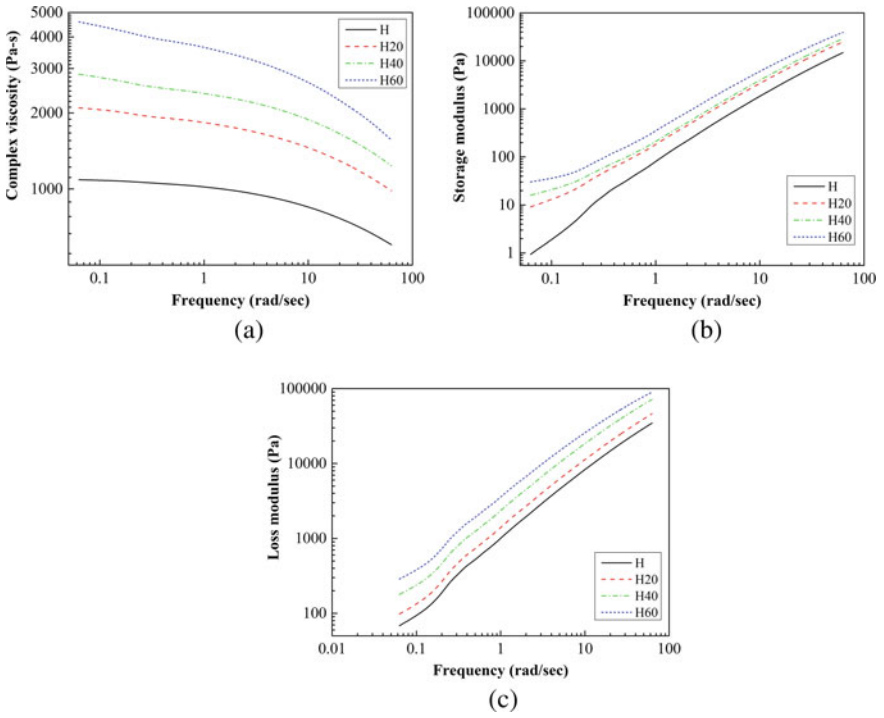

Fig. 4.2 **a** Complex viscosities, **b** storage, and **c** loss moduli of HDPE and blends [5]

4.1.2.2 Temperature Sweep

Figure 4.3 shows temperature sweep plots of HDPE and associated foams at 1 Hz. Throughout the temperature sweep, the storage moduli of neat HDPE and foams fall as the temperature rises, as seen in Fig. 4.3a. As temperature rises, the distance between storage modulus curves narrows. This means that at higher temperatures, GMB content has a smaller impact on storage modulus than at lower temperatures. The distance between storage modulus curves widens at low temperatures, and all curves become widely separated. Since the storage modulus in viscoelastic materials represents the molecular elastic response, its effect decreases as the temperature increases. Reduced storage modulus at higher temperatures could be explained by lower bonding strength and increased mobility of polymer chains. Loss modulus yields a similar result, as seen in Fig. 4.3b. The loss modulus is higher than the storage modulus, implying more viscous segmental friction between GMB and the polymer melt, leading to higher viscosity. Tan δ results are displayed versus temperature in Fig. 4.3c. The viscous (loss modulus) ratio to elastic section is called tan δ. The melting behavior is determined by tan δ values (liquid or solid). The viscous component contributes the most to the temperature sweep, as shown by the tan δ

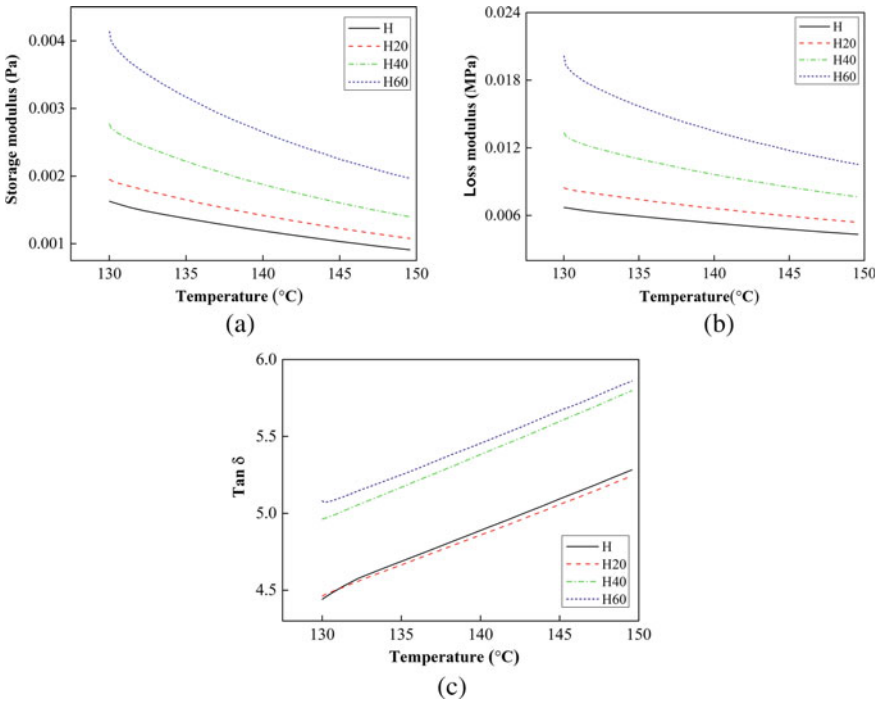

Fig. 4.3 **a** Storage, **b** loss moduli, and **c** tan δ of H-H60

curve. It is also clear from previous discussions that an increase in GMB content also increases melt viscosity.

MFI and rheological responses render selection criteria for choosing suitable printing parameters for sound-quality prints. As a result, processing parameters must be carefully studied based on rheological and MFI investigations.

4.2 Filament Development

The most popular process for shaping polymers is extrusion. It is an uninterrupted process that employs a screw/barrel operation to drive polymer melt through a die to make products, including films, pipes, plates, tubes, profiles, etc. It can be used for compounding or palletizing polymerization. An extruder comprises an Archimedean screw that rotates inside a heated barrel, eventually melting polymeric granules or powder and delivering it to a die for shaping. The polymer is melted by a combination of electrical heaters along the length of the barrel and frictional heat produced by the melt being sheared by the screw rotation. Solids conveying or feeding, melting or transition, and metering or pumping are the three-primary functional/geometrical

zones of an extruder screw. To develop a good quality GMB/HDPE syntactic foam filament, the issues related to particle breakage, formation of voids, and improper mixing must be carefully considered. For clarification, a schematic representation and a photograph of a single-screw extruder used to develop HDPE and foam filament are depicted, respectively, in Fig. 4.4a and b. The single-screw extruder's specifications are listed in Table 4.1 for reference.

To extrude HDPE and foam filaments, a 25SS/MF/26 type single-screw extrusion system was procured from Aasabi, India, and had a 25:1 L/D ratio. The HDPE granules and H20–H60 blends are dried in an oven for 24 h at 80 °C to remove moisture, if any, prior to feeding into the extrusion hopper. Extruded filament quality is influenced by the barrel and die temperatures and screw and take-off speeds. Solid pellets are converted to a semi-molten state and are subsequently extruded without

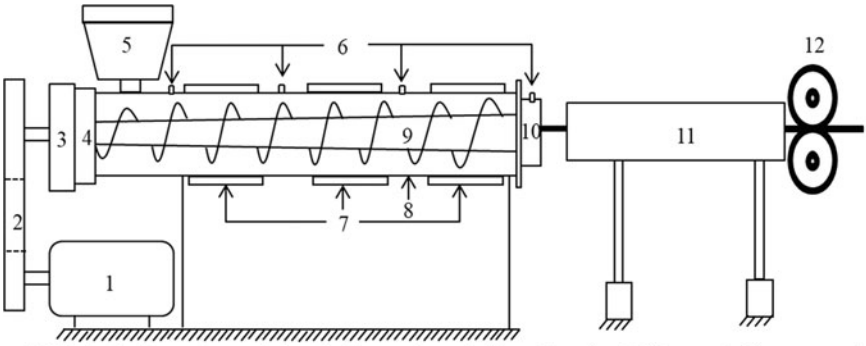

1. Motor 2. Power transmission 3. Gear reducer 4. Thrust bearing 5. Hopper 6. Thermocouple 7. Heater 8. Barrel 9. Screw 10. Die 11. Water trough 12. Take-up unit.

(a)

(b)

Fig. 4.4 **a** Schematic representation of the industrial-scale single-screw extruder and **b** experimental setup

Table 4.1 Single-screw extruder specifications

Specification	Details
Cooling	Water cooling
Die sizes	1.75, 2.5, and 3 mm
Drive	3 HP ACVF Drive, Max. RPM 60
Heaters	Ceramic in SS cover, 4 nos. with load up to 5 Kw
Heating control panel	PID controllers with 5 zones, Accuracy ± 1 °C, Max. Temp. 450 °C
Hopper	Min. 3 kg, SS sheet with discharge chute
Make and model	Aasabi Machinery (P) Ltd. Dombivli, Mumbai, India. (25SS/MF/26, L/D ratio of 25:1)
Pelletizer	Helical type, minimum 4″ dia. × 4″ L with 0.5HP ACVF drive
Screw	High tensile nitride hardened alloy steel to sustainable up to 450 °C, Dia. 25 mm with length 26D having uniform discharge
Spooling arrangement	Take up rollers with 0.5 HP ACVF drive with height adjustments and castor wheels

material blockage from the die at the appropriate barrel and die temperatures. The semi-viscous material post-extrusion is made to pass through a water bath before being pulled over by the take-off assembly. The diameter of the filament is determined by the extruding rate (screw/take-off speeds). The screw of the extruder rotates at a rate of 25 rpm. The filaments from the extruder are spooled using an 11.5 rpm take-off device. The 2.85 ± 0.05 mm dia. filaments are extruded using all the aforementioned parameters to realize the representative filament, as depicted in Fig. 4.5. In addition to speed limits, the distance (radial) between the pair of rollers on the take-off assembly of the extruder can be adjusted to reduce the ovality of the extruded filaments. All these values were determined based on high density polyethylene's temperature of melting, homogeneous and uniform GMB mixing in a matrix having minimized breakage, blend rheological behavior, and the existence of porosity, if any, while extruding the filament. The filler-matrix interactions, filler percent, and matrix porosities influence the performance and behavior of extrusion of the foamed filaments. Spooling strength and stiffness are required for filaments to be utilized in 3D printers. As a result, testing to determine the density, morphology (in this section), and tensile properties of extruded filament are carried out prior to printing to ensure that the filament has the quality, stiffness, and strength required for usage in a commercially available printer.

Density estimates, void percent, and the weight reduction potential of filament (F) and print (Pnt) are listed in Table 4.2. Due to their hydrophobicity, the observed (experimentally computed) and theoretical density of H filaments deviate in a narrow range, indicating low void formations. Voids affect the mechanical response of HDPE and their foams as the effective load-bearing area decreases. GMB % raises void contents in filament (2.50–7.70%) and improves print quality (6.14–9.73%). The presence of more voids in prints than in filaments indicates a transfer of the void

Fig. 4.5 Representative extruded H60 feedstock filament [5]

Table 4.2 Filament (F) and Prints (Pnt)—Physical properties [5]

Material	Φ_f (vol. %)	ρ th (kg/m^3)	ρ^{exp} (kg/m^3)		Φ_f (%)		Weight-saving potential (%) w.r.t H	
			F	Pnt	F	Pnt	F	Pnt
H	0	950	942 ± 8	927 ± 12	0.84	2.42	–	–
H20	20	880	858 ± 15	826 ± 13	2.50	6.14	8.92	10.90
H40	40	810	780 ± 11	746 ± 18	3.70	7.90	17.20	19.53
H60	60	740	683 ± 12	668 ± 10	7.70	9.73	27.49	27.94

space from the extruded filament to the prints. In addition, H-H60 prints have additional porosities of 1.58, 3.64, 4.2, and 2.03%, respectively. Air gaps (residual microporosity) between the raster cause porosity additions in 3D prints with an infill of 100%. These extra porosities combine to generate 3-phase SFs (GMB, HDPE, and raster gaps), which improve damping even more.

Even after 24 h of immersion in liquid nitrogen, the extruded filaments did not break. As a result, micrographs are sliced with a knife. The material flow lines are apparent in the micrographs due to the use of the knife (Fig. 4.6). Figure 4.6a shows a circular cut section of a sample, H20 filament, which confirms the suitable extrusion setting's adequacy. Figure 4.6b presents a lower magnification micrograph of H60, which exhibits a consistent distribution of undamaged GMBs in the HDPE-compliant matrix and few voids. In case these voids get transferred during 3D printing, such pores/voids may further increase three-phase SFs compliancy, ultimately leading to the increased damping. In a higher H60 micrograph magnification, poor interfacial bonding between HDPE and GMB can be seen (Fig. 4.6c). It is clear because constituent materials are employed in their natural state, without any surface modifications, to save time, money, and the difficulty of matching attributes with inconsistently coated layer thickness.

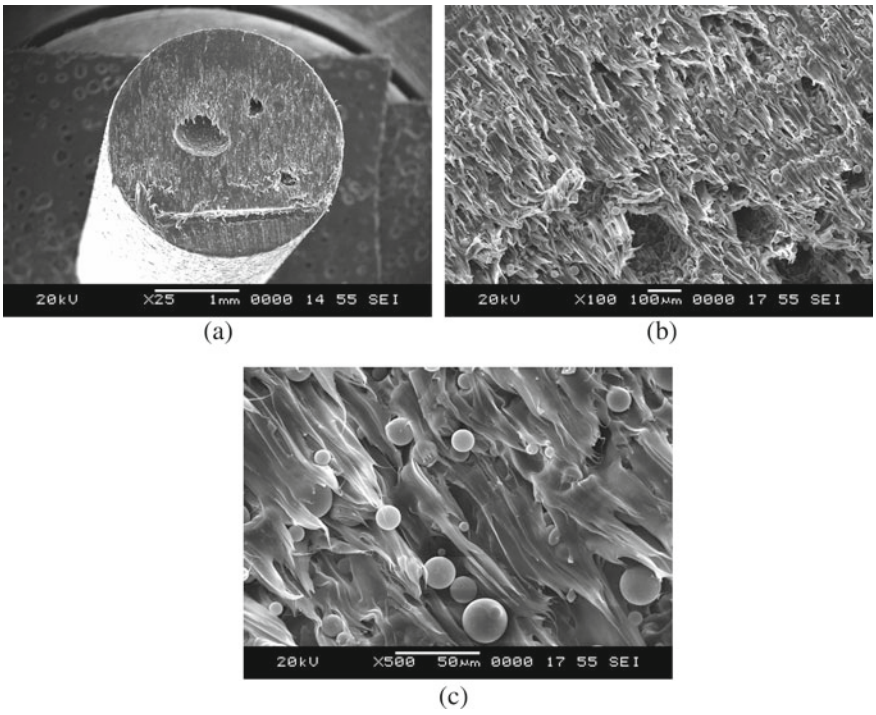

Fig. 4.6 Filaments SEM **a** cross-sections of H20 and H60 at **b** low and **c** high magnification [5]

4.3 3DP of SF Core and Their Sandwiches

An industrial-scale FFF 3D printer is depicted in Fig. 4.7a and b, respectively. The printer has dual brass nozzles and an overhead gantry with an extrusion/printing head that includes a melting unit and two nozzles, one for part material and the other for support material. The heating block above the nozzle provides the heat needed for filament melting. Appropriate built-in heating elements can maintain the temperature of the enclosed printing chamber. A fixed glass bed with embedded heating components is used in the chamber. The loading spools of part and support material are facilitated through a hanger arrangement. The machine control unit uses individual stepper motors to monitor the movement of the printing head in the X, Y, and Z directions. The technical characteristics of the 3D printer utilized in this study are listed in Table 4.3.

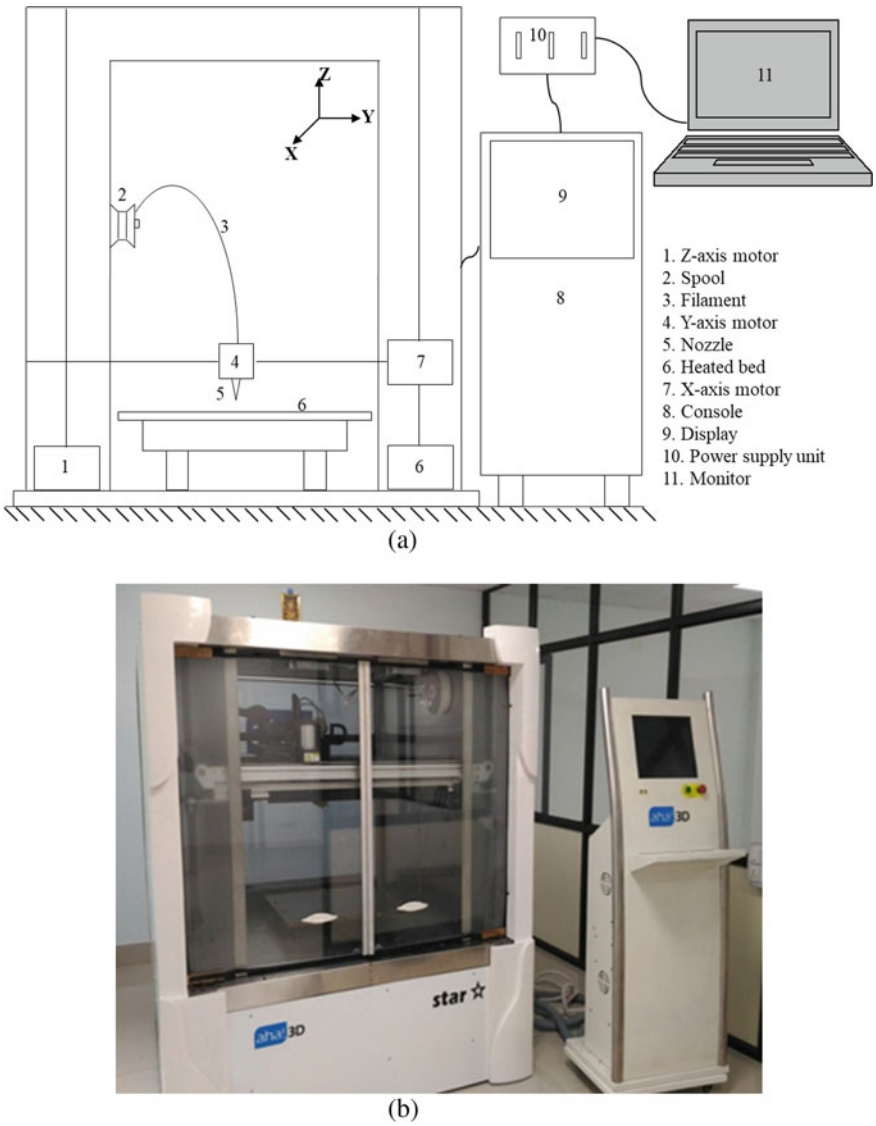

Fig. 4.7 **a** Schematics of FFF printer and **b** FFF printer utilized in the present work

4.3.1 3DP of SF Cores

H-H60 filaments were obtained and used as an input material for 3D printing core and sandwiches. AHA 3D, India, had developed a customized FFF-based Star series 3D printer with two 0.5-mm-diameter nozzles. Pilot experiments (Table 4.4) are conducted to determine the best printing parameters for core and sandwich printing.

Table 4.3 Specifications of FFF-based 3D printer

Specification	Details
Build chamber	Up to 100 °C
Build platform	Up to 150 °C
Build volume	500 × 500 × 500 mm^3
Data import format	STL, AMF, OBJ
Filament diameter	3 mm (Standard)
Layer height	100 to 500 μ
Make and model	Aha 3D Innovations Pvt. Ltd., Jaipur, Model: Star
Max. extrusion temp	Basic tool head: 300 °C, Standard tool head: 500 °C
Number of extruders	2
Positional accuracy	50 μ (stepper), 20 μ (servo), 4 μ (dual servo)
Power requirement	220 V AC, three phases
Printing materials	All engineering thermoplastic and plastic composites, ABS, HIPS, PC, Nylon, TPU, TPE, carbon fiber composite, etc
Rate of production	Basic tool head: up to 15 cm^3/hr., standard tool head: Up to 150 cm^3/hr
Screw	High tensile nitride hardened alloy steel to sustainable up to 450 °C. Suitable compression ratio (at least Dia. 25 mm with length 26D) having a uniform discharge at metering zone
Technology	Fused filament fabrication (FFF)
Tool head cooling	Liquid cooled
Workstation compatibility	Windows XP, Windows 7, Linux

Compared to totally dense molded components, the appropriate temperatures and flow rate are established per the pilot trials to obtain an entirely stiff complete solid (infill−100). Printing at high temperatures can assist produce uniform temperature distribution and the annealing effects, resulting in improved layer adhesions and dimensional stabilities. Incorrect material flow via the nozzle and non-uniform bonding of the bottommost layer with the high density polyethylene plate put on the printer's bed occurred when the nozzle and bed temperatures were below 200 and 60 °C, respectively. For bed and nozzle temperatures over 100 and 240°C, respectively, higher melt flows through the nozzles, and substrate distortion is observed. The results of the experimental studies to find optimal printing parameters for HDPE are shown in Fig. 4.8.

The temperature of the nozzle is maintained higher than the Vicat softening point of high density polyethylene (124 °C). For printing HDPE, the printing and bed temperature are changed between 200–230 °C and 60–100 °C, respectively. The trials are done using 3DP HDPE since it has the most warpage when compared to foams.

3D printed samples are left in the 3D printer's chamber until they reach ambient temperature. Printed samples show uniform layer bonding with the least amount of

Table 4.4 Remarks on different 3D printing parameters

Printing temperature (°C)	Print bed temperature (°C)	Observation	Figure 4.8
200	60	Improper layer deposition	a
220	60	Interlayer defects	b
220	100	Bottom layers diffusion with substrate	c
240	100	Maximum warpage, defective part	d
220	80	Smooth layered deposition, no defects between layers, smoother peeling off of the part, no distortions	e

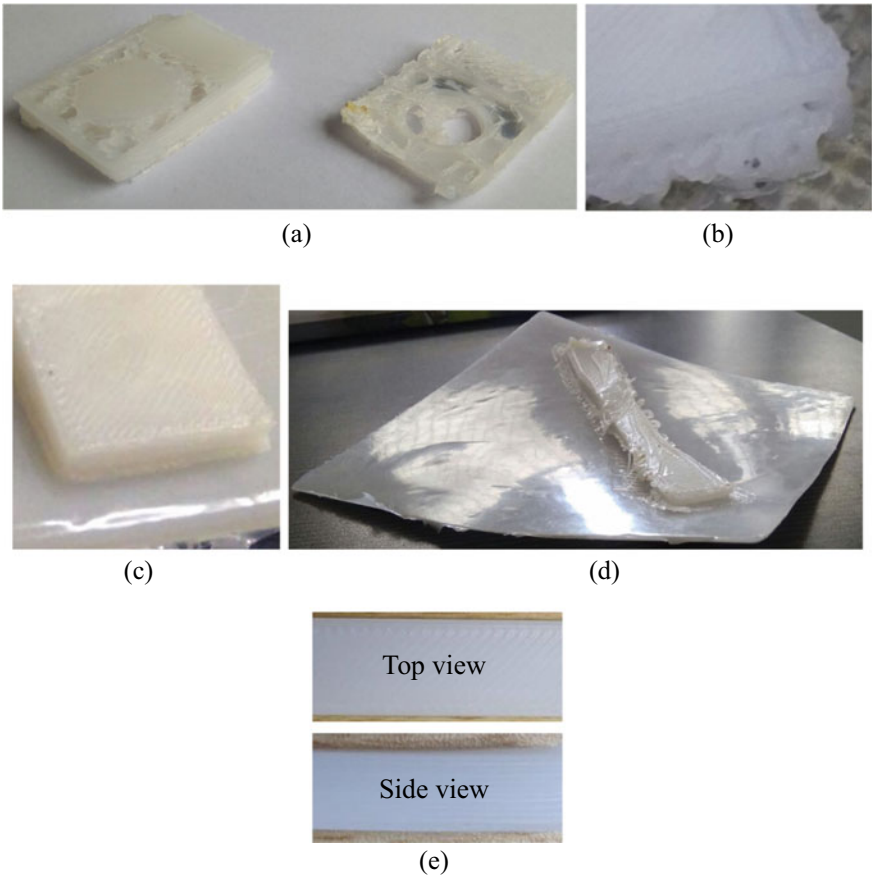

Fig. 4.8 Challenges in 3D printing of H (Table 4.4) **a** incorrectly deposited layers, **b** defects between layers, **c** higher diffusion, **d** maximum warpage, and **e** defect-free print [5]

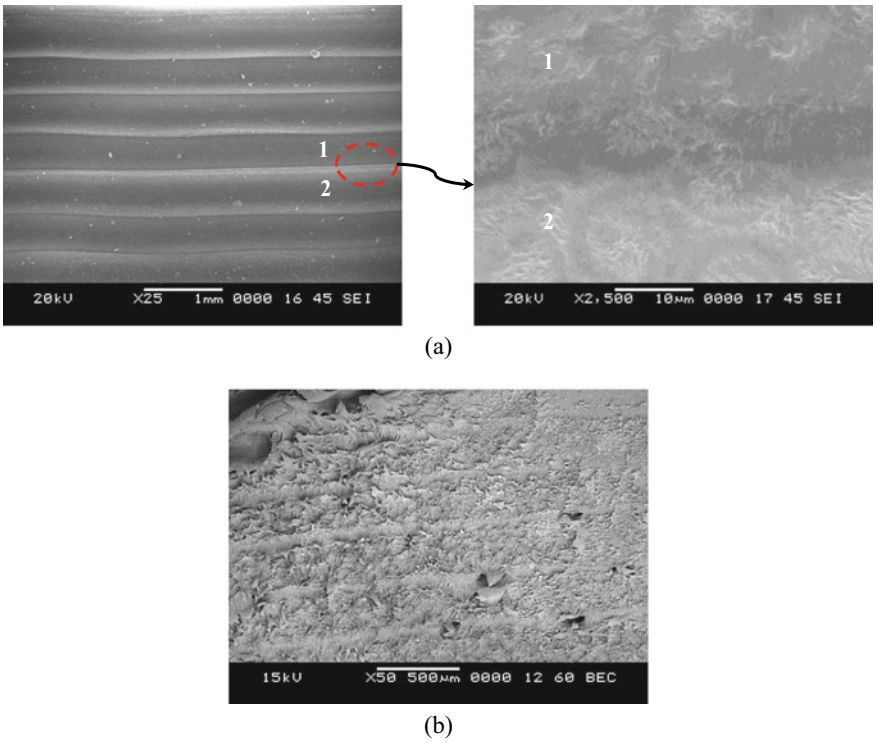

Fig. 4.9 SEM of printed **a** HDPE along and **b** across the thickness/deposition direction [5]

warpage (Fig. 4.9a). At increased magnification, the highlighted area in Fig. 4.9a indicates very smooth diffusion across the layer. This fact verifies the feasibility of the HDPE printing/processing parameters (Table 4.4). Figure 4.9b shows SEM of freeze-fractured high density polyethylene.

4.3.2 Three-Dimensional (3D) Printing of Sandwich Samples

By feeding HDPE and foamed filaments into nozzle "1" (N1) and nozzle "2" (N2), respectively, for developing SH20–SH60 SF-cored sandwich composites, the sandwich (S) printing can be done all at once (concurrently). The pilot tests (Table 4.5) are used to simultaneously determine the best printing parameters for printing SF-cored sandwiches. To obtain adequate values, SF-cored sandwiches of 180 × 18 × 8 mm^3 are printed with various nozzles, chambers, bed temperatures, and printing speeds. Table 4.5 summarizes the results of the experiments used to determine the best printing settings for the core and sandwiches by adjusting N1 (Fig. 4.10a) and N2 (Fig. 4.10b) temperature, bed, and chamber temperature (Fig. 4.11a) at various

printing speeds (Fig. 4.11b). Table 4.6 summarizes the most appropriate printing parameters based on Table 4.5's findings. To achieve better adhesion, eliminate shrinkage, and limit residual stresses, all samples are printed on HDPE substrate at chamber and bed temperatures of 60 and 80 °C, respectively. N1 deposits 1 mm of bottom HDPE skin at a temperature of 220 °C. Following that, N2 is used to deposit the foamed core for the subsequent 6 mm at temperatures of 220 °C for H20 and 240 °C for H40−H60. Further, on the topmost layer of the previously printed core, N1 prints high density polyethylene skin of 1 mm. Using a simplified 3D tool path, G-codes are generated to build sandwiches (SH20-SH60) with an 8 mm total thickness by following the N1-N2-N1 sequence. All the core and sandwich coupons have a rectilinear pattern with a y-axis orientation. To ensure appropriate clearances between the prints and nozzle, a layered thickness of 0.32 mm was chosen. To optimize the surface smoothness and reduce warpage, all samples are printed at a constant speed of 30 mm/s. MFI estimates have set a multiplier of 0.9 for H−H40 and 1.3 for H60. With a printing speed of 30 mm/s, layers can be deposited without difficulty for up to 60% MFI reduction. Because nozzle blocking occurs at higher MFIs, 1.3 multiplier is used for H60 with a specific temperature level.

Table 4.5 Experimental test observations during 3DP of SF-cored sandwiches

Parameter and range	Typical value	Observation	Figure No
Nozzle-1 temperature °C (200–230)	200	Non-uniform layer deposition	Figure 4.10a
	230	Bulk material flow at multiple locations	
	220	The material flow is continuous and smooth without any difficulty	
Nozzle-2 temperature °C (230–250)	230	Improper flow of material and rough surface finish	Figure 4.10b
	250	Lumped depositions	
	240	Good print with excellent surface finish	
Bed (60–100) °C and chamber temperature °C (40–80)	60 and 40	Shrinkage/warpage at the ends	Figure 4.11a
	100 and 80	Comparatively less warpage at ends	
	80 and 60	Samples without any warpage	
Printing speed mm/s (25–35)	25	Small islands formations on the surface	Figure 4.11b
	35	Formation of small voids on the surface	
	30	Sample with smooth surface finish	

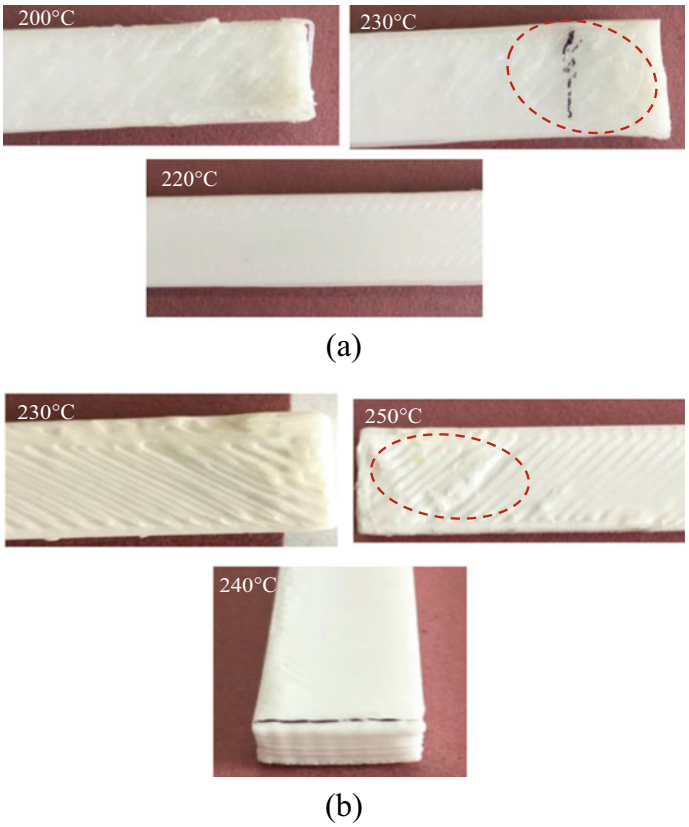

Fig. 4.10 Prints with different **a** N1 and **b** N2 temperatures

The micrograph of 3D printed H60 in Fig. 4.12a reveals consistent GMB distribution as well as elongated spaces. Lower MFI and reduced melt viscosity result in elongated gaps with greater filler volume percent. Because of air gaps/raster gaps/residual microporosities between neighboring rasters (Fig. 4.12b), prints have a higher void content than filaments (Table 4.2). Due to lower matrix content, high melt viscosities, and lower CTE, air gaps increase as GMB content increases. As previously stated, such microporosities may improve compressive and damping capacities.

SH20-SH60 sandwiches are printed using the selected printing parameters, and Fig. 4.13a shows a SH60 micrograph spanning three separate zones (top–bottom skin). The micrograph in the thickness direction is shown in Fig. 4.13b. Both micrographs show flawlessly diffused layers along and across the prints, showing that the printing conditions described in this paper are suitable.

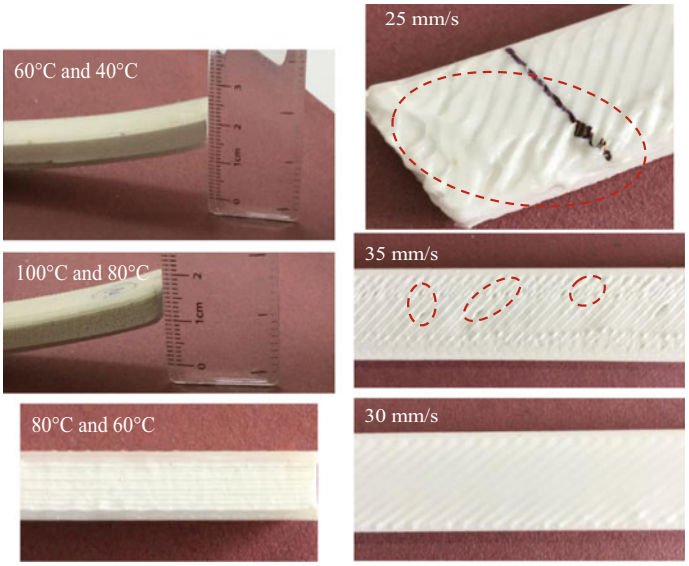

Fig. 4.11 Prints with **a** different combinations of chamber and bed temperatures and **b** different printing speeds

Table 4.6 Processing parameters

Parameters	H	H20	H40	H60	SH20	SH40	SH60
N1 (°C)—HDPE filament	220	–	–	–	220	220	220
N2 (°C)—Foam filaments	–	220	240	240	220	240	240
Extrusion multiplier	0.9	0.9	0.9	1.3	0.9	0.9	1.3
Temperature (°C)—bed	80						
Temperature (°C)—chamber	60						
Speed of printing (mm/s)	30						
Thickness of layer (mm)	0.32						
% Infill	100						
Raster pattern	Rectilinear						
Raster angle	± 45°						

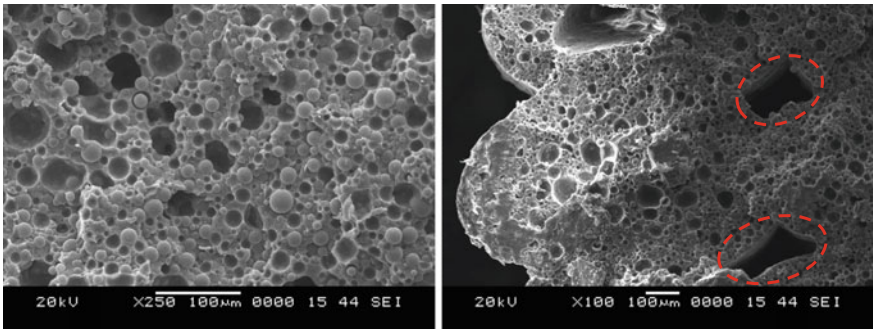

(a) (b)

Fig. 4.12 Micrograph of printed **a** H60 and **b** associated raster gaps (residual microporosity) in H60 [5]

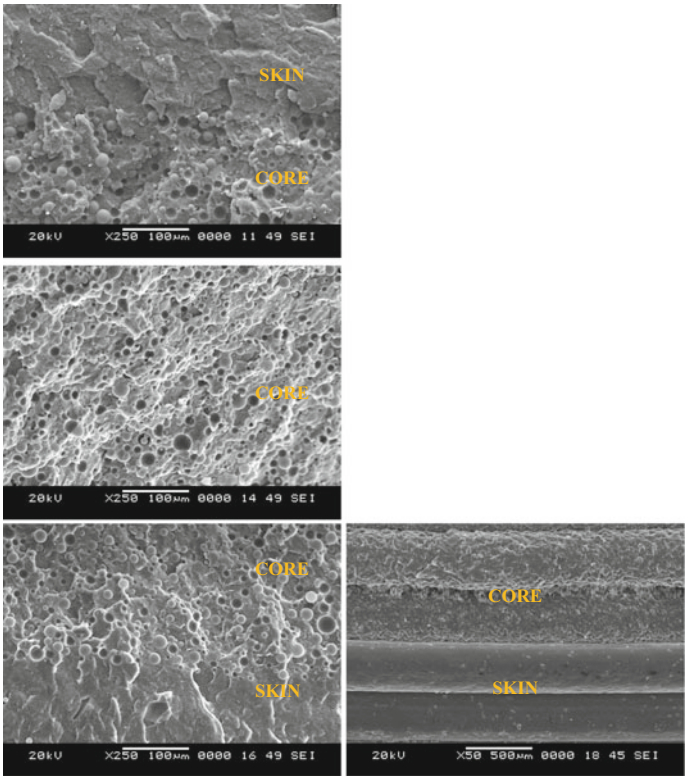

(a) (b)

Fig. 4.13 As-printed sandwich SEM of **a** across and **b** along the direction of thickness [6]

References

1. Escócio VA, Pacheco EBAV, Silva ALNd, Cavalcante AdP, Visconte LLY (2015) Rheological behavior of renewable polyethylene (HDPE) composites and sponge gourd (Luffa cylindrica) residue. Int J Polym Sci 714352
2. Mohanty S, Nayak SK (2010) Short bamboo fiber-reinforced HDPE composites: influence of fiber content and modification on strength of the composite. J Reinf Plast Compos 29(14):2199–2210
3. Shaikh H, Anis A, Poulose AM, Alam M, A-Otaibi MN, Alam MA, Al-Zahrani SM (2016) Studies on high density polyethylene reinforced with phosphate ore particles: thermal, rheological, mechanical and morphological properties. Polym-Plastics Technol Eng 55(17):1831–1841
4. El Achaby M, Ennajih H, Arrakhiz FZ, El Kadib A, Bouhfid R, Essassi E, Qaiss A (2013) Modification of montmorillonite by novel geminal benzimidazolium surfactant and its use for the preparation of polymer organoclay nanocomposites. Compos B Eng 51:310–317
5. Bharath HS, Bonthu D, Prabhakar P, Doddamani M (2020) Three-dimensional printed lightweight composite foams. ACS Omega 5(35): 22536–22550
6. Bharath H, Bonthu D, Gururaja S, Prabhakar P, Doddamani M (2021) Flexural response of 3D printed sandwich composite. Compos Struct 263:113732

Chapter 5
Mechanical Testing

5.1 Static Testing

5.1.1 Differential Scanning Calorimetry (DSC)

The melting and crystallization characteristics of filaments and prints with H–H60 mixtures are estimated using a PerkinElmer DSC-6000 from the USA. In a 30 L Al crucible, a 10 mg sample is heated to a temperature range of 0–200 °C and then isothermally cured for roughly 3 min at 200 °C. After removing the thermal history caused by previous processing phases, samples are cooled down to 0 at 10°/min. After three minutes of chilling at 0 °C, the cupons are heated from 0–200°C. Exothermic and endothermic peaks, which indicate enthalpy of melting at cold crystallization, can be seen on DSC graphs. It is determined that Crystallinity% (α_{Cryst}) is [1],

$$\alpha_{Cryst} = \frac{\Delta H_m}{\Delta H_m{}^*(1 - W_{GMB)}} \times 100, \tag{5.1}$$

where ΔH_m = fusion heat in J/g and $\Delta H_m{}^*$ = fusion heat/gram of HDPE, i.e., 293 J/g [2] and W_{GMB}= weight fraction of GMBs.

Table 5.1 shows the thermal response of HDPE-H60 (T_{Cryst}, T_{Melt}, and CTE). Figure 5.1 shows DSC graphs for H–H60. The endothermic peak for pure HDPE is detected around 108 °C, which is noted to be on the rise for foams. Figure 5.1 also shows a drop in endotherm and a rise in crystallization temperature as GMB concentration increases. This clearly shows that as HDPE cools, melt nucleation creeps in on the GMB surface at higher temperature, resulting in thick crystal lamellas and higher T_{Cryst} [3]. In comparison with H_2O, melts inertia is ignored because the foams temperature of crystallization changes in a narrowed range of 2.2% (Table 5.1). As shown in Table 5.1, increasing the filler volume percent has no effect on the T_{Melt} of both prints and filaments, indicating that the subsequent thermal history creeped in due to 3D printing after extrusion process has not resulted in additional thermal residual stresses, and printing/processing temperatures for the samples can

M. Doddamani et al., *3D Printing of Composites*, Materials Horizons: From Nature to Nanomaterials, https://doi.org/10.1007/978-981-99-1730-3_5

Table 5.1 Thermal behavior of samples [4]

Material	T_{Cryst} (°C)		α_{Cryst} (%)		T_{Melt} (°C)	
	F	P_{nt}	F	P_{nt}	F	P_{nt}
H	105.70	110.82	59.54	61.74	131.47	130.88
H20	112.67	113.12	49.12	50.72	132.51	131.24
H40	112.92	113.23	33.71	37.01	130.45	131.29
H60	112.59	113.27	25.79	28.59	130.86	130.90

be kept similar (elaborately discussed in the earlier section). With increased GMB content, there is a decrease in Crystal (56.68%) for foamed filaments.

Crystal fell from 61.74 (H) to 28.59% in printed samples, demonstrating a similar pattern (H60). As noted in the previous section, the related prints have a greater

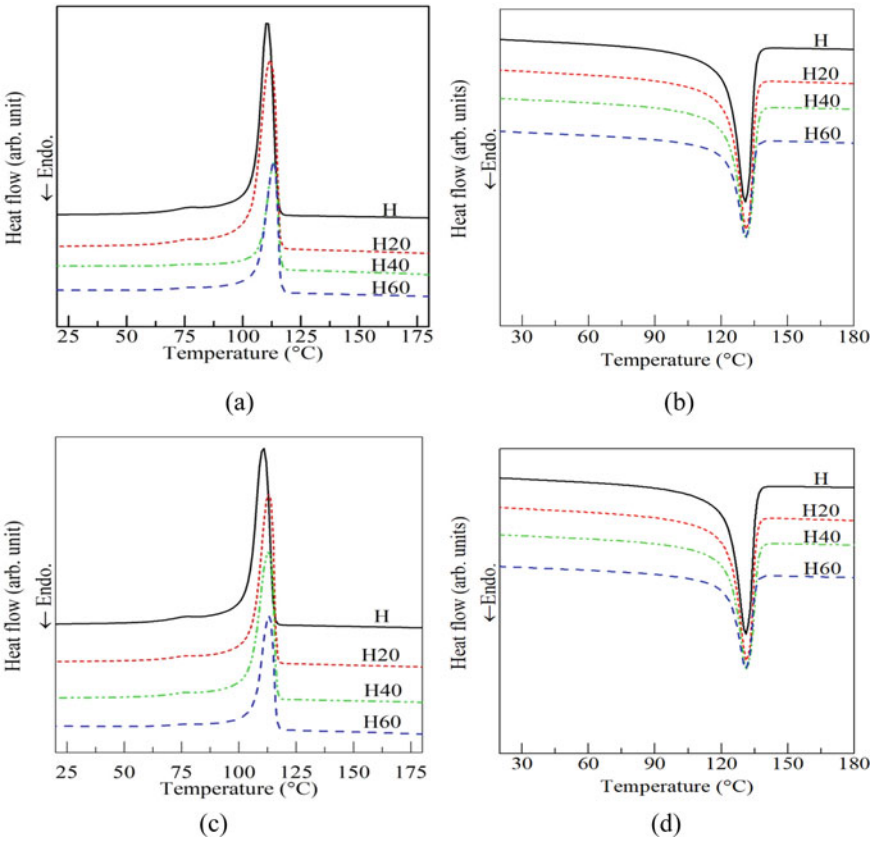

Fig. 5.1 Crystallization peaks: cooling cycles in **a** filament and **c** printed cupons. Melting peaks: heating cycles (2nd) in **b** filament and **d** printed cupons [4]

α_{Cryst} than filaments and are expected to exhibit higher dimensional stabilities and lower shrinkage. The filaments are quenched after extruding and pass through the water bath. As a result, relatively less energy and time are available for filament melt crystallization than in prints where materials cool gradually on the bed of the 3D printer [5]. α_{Cryst} declines in foams together with the crystal domain reduction of HDPE due to the resistance provided by glass microspheres to the polymer chain flow [6, 7]. As a result, the dimensional stability of the foamed prints increases with no distortions.

5.1.2 Coefficient of Thermal Expansion (CTE)

CIPET, Chennai's dilatometer, is utilized to calculate CTE for prints [8] with dimensions of 75 × 12.7 × 3 mm. Warpage is qualitatively displayed by CTE values, which also connect filler loading's impact on dimensional stability and microstructural studies [9]. CTE is performed in the temperature range of 20–90 °C. An average of five samples is reported for investigation.

As seen in Table 5.2, adding GMB to the HDPE matrix lowers CTE [10, 11]. Dimensional stabilities can be achieved by incorporating GMB into H at higher printing temperatures, as demonstrated in the previous section, where significant warpage reduction is observed in printed cupons with dimensional stabilities and decreased thermal residual stresses [10]. In addition to the larger discrepancy in CTE values between GMB and HDPE, the entrapped gas/air within GMB provides resistance to heat transfer, resulting in reduced thermal conductivity. Furthermore, CTE aids in the comprehension of the raster's diffusion and the generation of air gaps in 3DP. Because of the higher CTE values make warpage a critical and problematic issue when printing neat HDPE, as seen in Fig. 4.8d. Nonetheless, using the right printing and bed temperatures has solved the problem. Furthermore, owing to the lower thermally conductive gases/air within hollow GMB limiting heat flow, dimensionally stable printed cupons are observed in these foams [12]. The H60 print had the lowest CTE of all the foams, resulting in negligible raster diffusion and air gaps (Fig. 4.12b). As seen in Table 4.2, such air gaps/residual microporosities make SFs lighter (2–4%).

Table 5.2 CTE of printed samples [4]

Material	CTE × 10^{-6} (°C)	% decrease compared to HDPE
H	135 ± 3.29	–
H20	106 ± 3.85	21.48
H40	88 ± 2.65	34.81
H60	75 ± 1.15	44.44

5.1.3 Tensile Response

The Zwick Roell make Z020 is used to tensile test filament and 3D printed materials. The filament length is kept at 176 mm, with a 76 mm as the distance between the two grips. The test is conducted at a continuous loading rate of 5 mm/min. The strain is measured with an extensometer (gauge length 50 mm). The printed samples are tested using an extensometer with a gauge length of 25 mm, according to ASTM D638-14, at comparable crosshead displacement. An extensometer is used to measure the initial load elongation of 0.1 MPa. The load and displacement data are used to determine stress and strain. The five specimens' average modulus and strength values are examined for each arrangement. The matrix phase's reinforcing phase distribution, size, constituents interaction, and inherent qualities influence the tensile response.

5.1.3.1 Tensile Response of Filaments

To utilize feedstock filament material in a printer, filament must match certain specifications, such as form retention (shape and size) without excessive deformations/bending and the ability to sustain frictional force as it passes between drive rollers [13]. Bending can be prevented by maintaining the filaments firm enough to sustain the push of the driving roller without disturbing the corresponding printer elements. The tensile stress–strain graphs of filaments are shown in Fig. 5.2. When compared to H20, H40, and H60, stronger intact GMBs enhance filament moduli by 8.171, 14.402, and 46.812%, respectively (Table 5.3 and Fig. 5.2b). Due to its ductility, HDPE filament can be stretched more than 1000% without breaking. Figure 5.2a, however, only depicts strain up to 400%. Figure 5.2b shows that H40 and H60 failed at 25% strain. With a UTS of 12.63 MPa, H20 has the maximum strain of more than 40% among foams. According to Fig. 5.2c, a larger concentration of matrix in H20 efficiently resists the tensile forces by plastically deforming the entire cross-section. The highlighted region in Fig. 5.2c depicts the creation of a new surface, which increases strain at the bulk scale. Among the foams, H60 had the largest void of 7.7% (Table 4.2), resulting in substantially early filament fracture due to effective area reduction caused by elongated pores collapse/merging (locations 1–4 in Fig. 5.2d). Despite this, H60 has the maximum modulus due to the greater number of unbroken GMB microspheres (encircled area in Fig. 5.2d). Because of the weaker bonding between HDPE and GMB, strength falls as filler content increases, as shown in Fig. 4.6c. Furthermore, when the GMB content increases, the volume of HDPE drops, lowering the compliant ductile phase and leading in lower strength values. Surface treating GMB particles to improve interfacial bonding can increase filament strength; however, it is outside the purview of this study. Coupling agents induce brittleness and increase spooling stiffness, and hence, such a surface treatment strategy requires careful attention. The processing time and associated cost

are reduced to a minimum, boosting the industrial adaptability of components with similar moduli and strength.

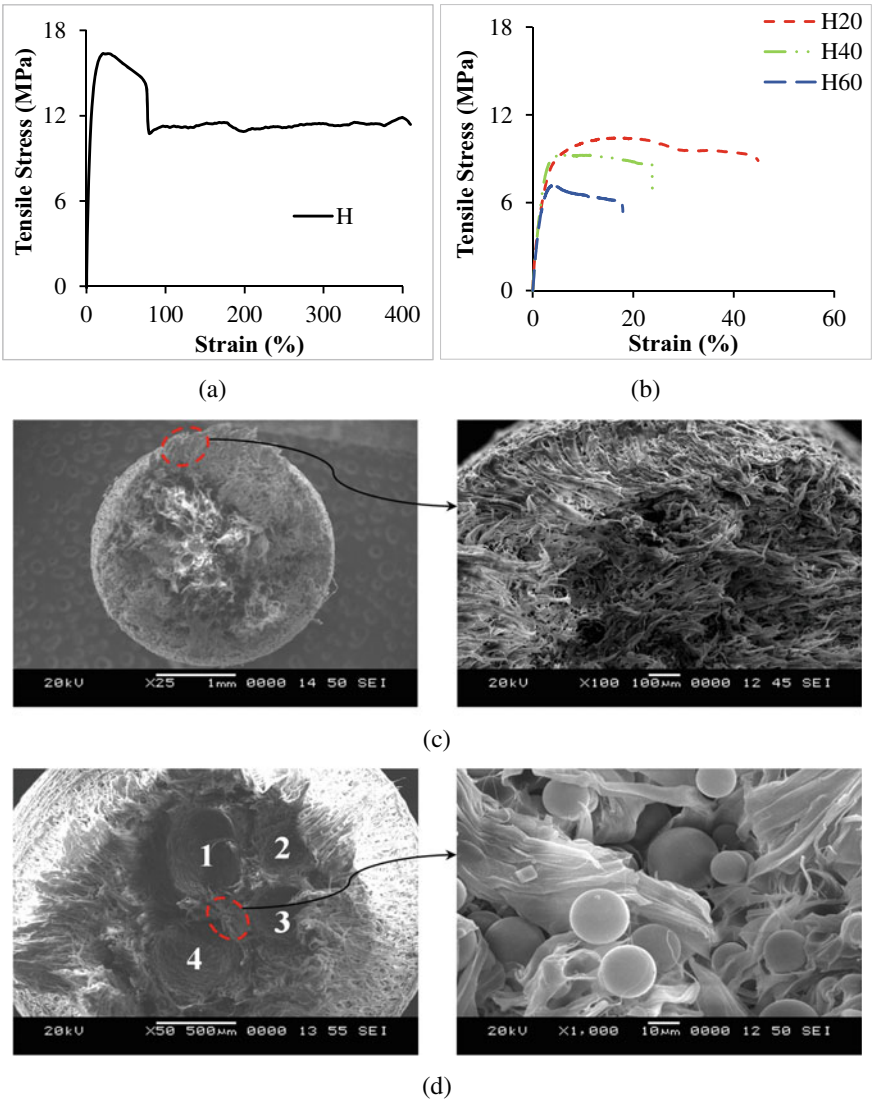

Fig. 5.2 Stress and strain plots of **a** HDPE and **b** H20–H60. Micrographs of **c** H20 and **d** H60 filaments after tensile test [4]

Table 5.3 Tensile response [4]

Material	Modulus in MPa		UTS in MPa		Elongation at UTS in %		Fracture strength in MPa		Fracture strain in %	
	F	P_{nt}	F	P_{nt}	F	P_{nt}	F	P_{nt}	F	P_{nt}
H	722 ± 16.73	810.25 ± 16.73	16.4 ± 0.22	17.68 ± 0.21	17.90 ± 0.26	15.04 ± 0.23	–	6.68 ± 0.11	–	93.00 ± 1.03
H20	781 ± 17.95	865.56 ± 17.79	10.45 ± 0.42	12.8 ± 0.35	12.63 ± 0.33	5.68 ± 0.29	8.93 ± 0.23	10.39 ± 0.29	44.27 ± 0.23	30.48 ± 0.10
H40	826 ± 14.27	1125.68 ± 12.41	9.25 ± 0.39	9.49 ± 0.49	5.27 ± 0.35	3.11 ± 0.31	7.01 ± 0.19	8.24 ± 0.25	23.81 ± 0.22	21.66 ± 0.06
H60	1060 ± 18.53	1199.26 ± 11.53	7.16 ± 0.17	8.45 ± 0.18	2.39 ± 0.21	4.69 ± 0.11	5.90 ± 0.14	7.78 ± 0.19	16.53 ± 0.31	14.49 ± 0.07

5.1.3.2 Tensile Response of 3D Printed Samples

The stress–strain response of 3D printed H–H60 follows a similar pattern, and the values are reported in Table 5.3. Pure H filament does not break even after a 1000% strain, whereas HDPE prints can only withstand a 45% strain, demonstrating a behavioral transition from ductile (compliant) to brittle phase during 3DP. Extrusion of HDPE occurs twice: first during filament creation and again in the printer extruder of the nozzle. Multiple extrusion cycles cause polymer chain realignment and crosslinking due to thermal processing, which leads to the hardening phenomena. The printed H40 and H60 foams have 21.67 and 14.48% failure strains, respectively, whereas H20 has up to 30.47% strain. Due to raster fibrillation, which results in broom-like fibrous ends, HDPE has a lengthy necking region (Fig. 5.3a). Because of substantial plastic deformation, new surface forms arise in fibrous endings (SEM of the encircled area in Fig. 5.3a). The H40 and H60 foamed prints have no necking regions and fracture normally, as seen in the fractographic area, where matrix plastic deformations are barely visible (Fig. 5.3b).

All the microspheres appear to be intact, indicating that substantial weight savings of 28% (Table 4.2) were realized after printing. At increasing filler percentages, intact GMB particles form a load-carrying matrix, which crumbles early due to post-printing-induced stiffness/brittleness. The modulus and strength of the filament and printed coupons improved by 12.22, 10.83, 36.28, 13.14%, and 7.8, 22.49, 2.59, and 18.02%, respectively, in a comparative examination. The results of HDPE/GMB prints are compared to injection-molded HDPE/cenosphere foams. When compared to injection-molded SFs, 3D printed HDPE has a greater elastic modulus of 53.17%, indicating that it has a higher UTS. At UTS, 3D printed foam elongates and has a fracture strength of 47.45%, which is three times that of injection-molded specimens [14].

Foam modulus rises as GMB percentage rises (Table 5.3). H60 has the highest foams modulus, at 48.02% more than HDPE print. With no tooling costs, 3D printed H–H60 has 1.6–1.7 times stronger moduli than molded counterparts. When compared to H., the fracture strength of foam prints is 1.16–1.56 times higher. Because printing offers flexibility in constructing integrated (jointless) components with complicated designs, particular qualities of foams are necessary for weight-critical regimes. H60 and H20 are the foams with the highest specific strength and modulus, respectively. Table 5.4 indicates the weight reducing potential of GMB/HDPE based on E/n estimates ($n = 1$, 2, and 3). Table 5.4 shows that printed foams can be utilized efficiently in integrated complicated designs such as buoyancy modules, automotive, and aerospace components.

5.1.3.3 Property Map

The tensile response versus composite density manufactured utilizing various processing techniques is shown in Fig. 5.4 [15–17]. In comparison with solid-filled material systems, closed-cell foamed composites have promising qualities that can be

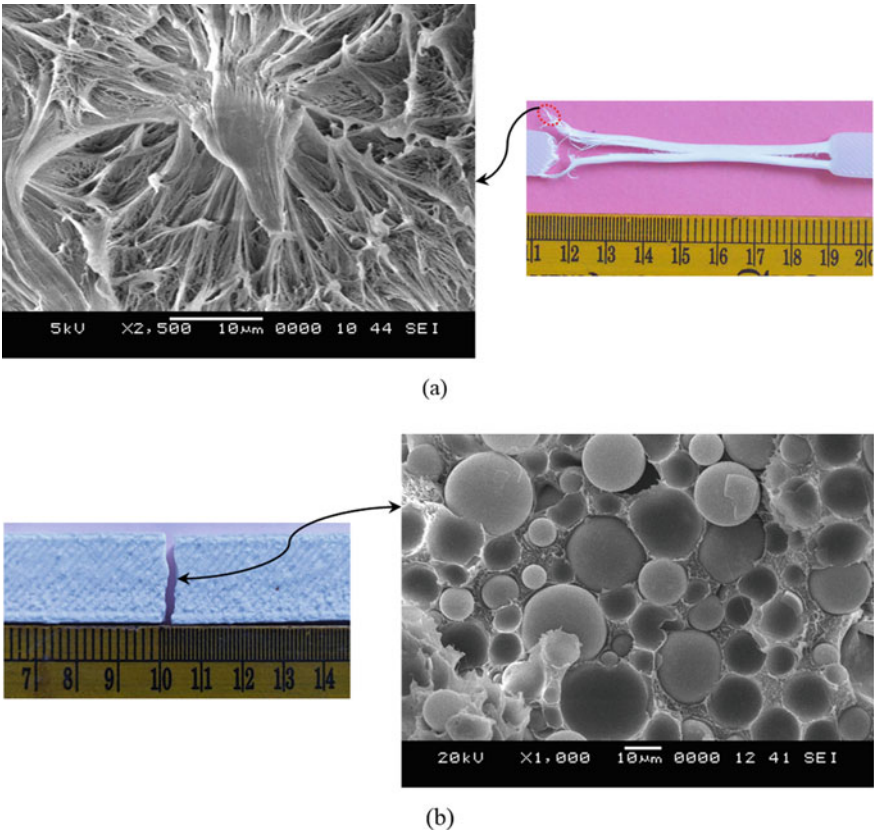

Fig. 5.3 3D printed **a** HDPE and **b** H60 after tensile tests [4]

Table 5.4 Weight reducing factor [4]

Material	$\frac{E}{\rho}$ [a]	$\frac{E}{\rho^2}$ [b]	$\frac{E}{\rho^3}$ [c]
H	0.87	0.94	1.02
H20	1.05	1.27	1.54
H40	1.51	2.02	2.71
H60	1.80	2.69	4.02

[a] MPa/kg/m^3, [b] MPa/(kg/m^3)^2 $\times$ 10^{-3}, [c] MPa/(kg/m^3)^3 $\times$ 10^{-6}

used in weight-sensitive regimes. GMB-based 3D printed foams have a density that falls in between compression and injection-molded foams. Except for wood-filled composites, the tensile moduli of printed composites overpower compression and injection-molded composites (Fig. 5.4a). GMB foams had comparable strength to compressive and injection-molded prototypes (Fig. 5.4b). The selection of optimal printing and extrusion factors with minimalized particle breakage resulted in a large

weight decrease of 28%. Weight reductions of this magnitude for complexly designed integrated printed components would improve performance while lowering carbon emissions.

5.1.4 Flexural Behavior of 3D Printed Core and Sandwich

Flexural testing of a 3D printed core with a sample dimension of 127 × 12.7 × 3.2 mm^3 (ASTM D790-17) and a sandwich with a sample dimension of 180 × 18 × 8 mm^3 (ASTM C393-16) is carried out in a three-point bend configuration using a computer-controlled Zwick (Zwick Roell Z020, ZHU) machine with a load cell capacity of 20 kN. It is assumed that the strain rate is 0.01 S-1 and that the preload is 0.1 MPa. With a 16 (span length):1 (depth ratio), the loading rates of 1.37 mm/min for core and 3.41 mm/min for sandwich samples are maintained. The averaged values with standard deviation are presented after testing a minimum of five samples. The test is terminated at a strain of 10% when cupons did not fracture completely. Flexural modulus is computed using,

$$E_{fM} = \frac{L^3 m}{4bd^3}, \tag{5.2}$$

where L is the support span (mm), b is the width of beam (mm), d is the thickness of beam (mm), and m is the slope of the tangent to the initial straight-line portion of the load–deflection curve. The flexural stress (σ_{fS}) is calculated by,

$$\sigma_{fs} = \frac{3PL}{2bd^2}. \tag{5.3}$$

5.1.4.1 Flexural Behavior of 3D Printed Core Samples

As shown in Fig. 5.5a, the flexural test is performed in a three-point bending arrangement with samples placed. As shown in Fig. 5.5b, the printed core begins to give as the load is gradually applied. The crack started from the tensile zone and spread throughout the loading directions until it reached the other compressive region (Fig. 5.5c), indicating flexural failure. Surprisingly, the crack failed to propagate within the deposited layers, indicating that the printing conditions were appropriate (Table 4.6). In comparison with H, which did not break until 10% strain, foams showed brittle fracture (Fig. 5.6a). The presence of GMB in HDPE causes brittleness. Figure 5.6b shows that increasing GMB content increases flexural modulus. Table 5.5 summarizes the results. Due to weaker interfacial bonding between constituent pieces and the presence of raster's gaps (Fig. 5.6d), the flexural strengths are reduced (Fig. 5.6c). When compared to foam samples, HDPE had the strongest strength, with

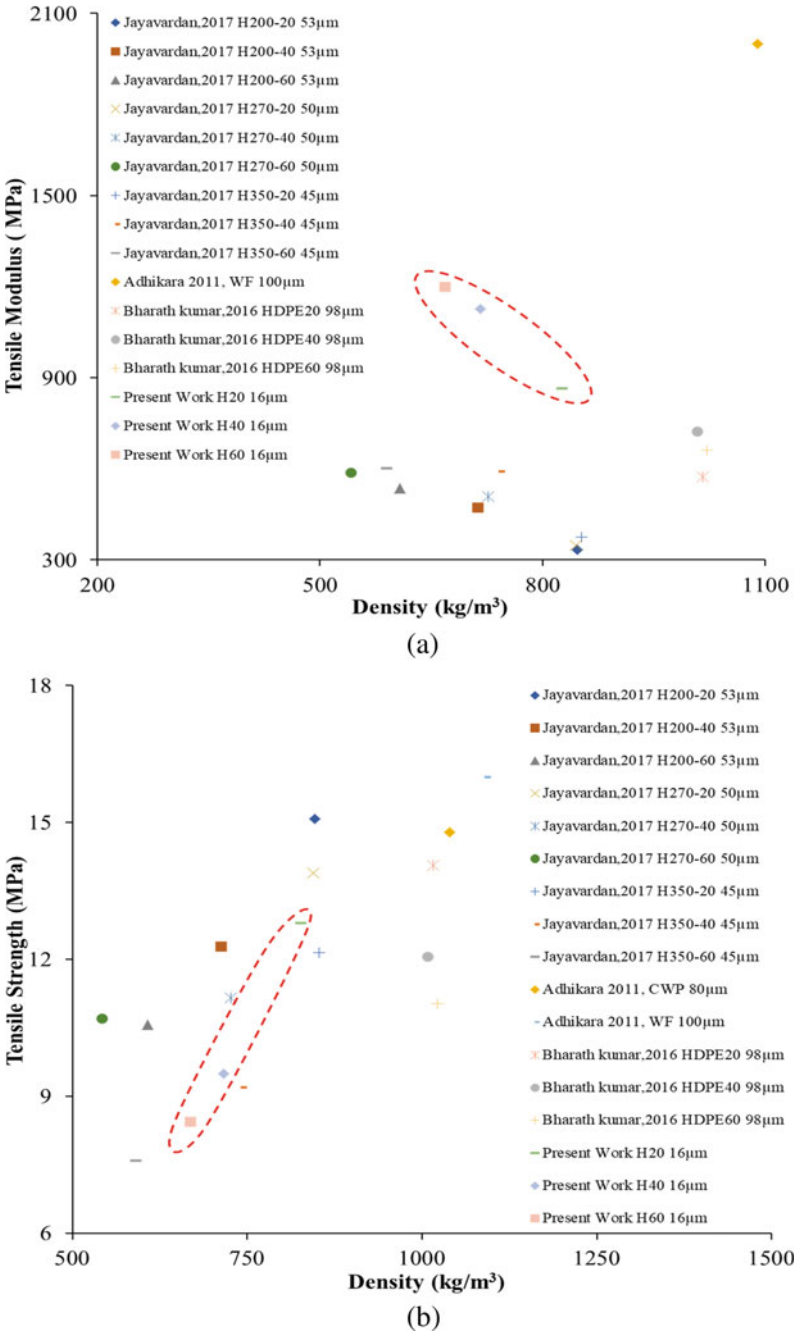

Fig. 5.4 Tensile, **a** moduli and **b** strength of high density polyethylene composite [14–16]

1.21, 1.47, and 1.67 times the strength of H20–H60 foams. The modulus of H60 is 1.37 times greater than that of H, which is owing to undamaged GMB microspheres even at the greatest filler embedment (Fig. 5.7c). Compared to H60 (Fig. 5.7c), fewer filler quantities result in more widespread plastic deformation (Fig. 5.7a, b).

When compared to HMBs, GMBs inserted in the HDPE matrix enhance the specific moduli twice (Table 5.5). In comparison with molded counterparts, the moduli of H–H60 printed foamed cupons are 1.39–1.08 times greater, although strength is higher and comparable in HDPE and H20. The printed H40 and H60 samples have a drop-in strength of 1.14 and 1.27 compared to fully dense molded samples due to greater matrix porosity caused by raster gaps [18]. Due to decreased CTE values, the volume of these raster gaps grows as filler loadings increase. Nonetheless, overlapping layers can eliminate these gaps, which will be investigated further in future studies. As previously stated, flexural strength is observed to decline as constituent elements are used in the received condition. Furthermore, adding filler increases the amorphous percentage, resulting in more constrained matrix flows and

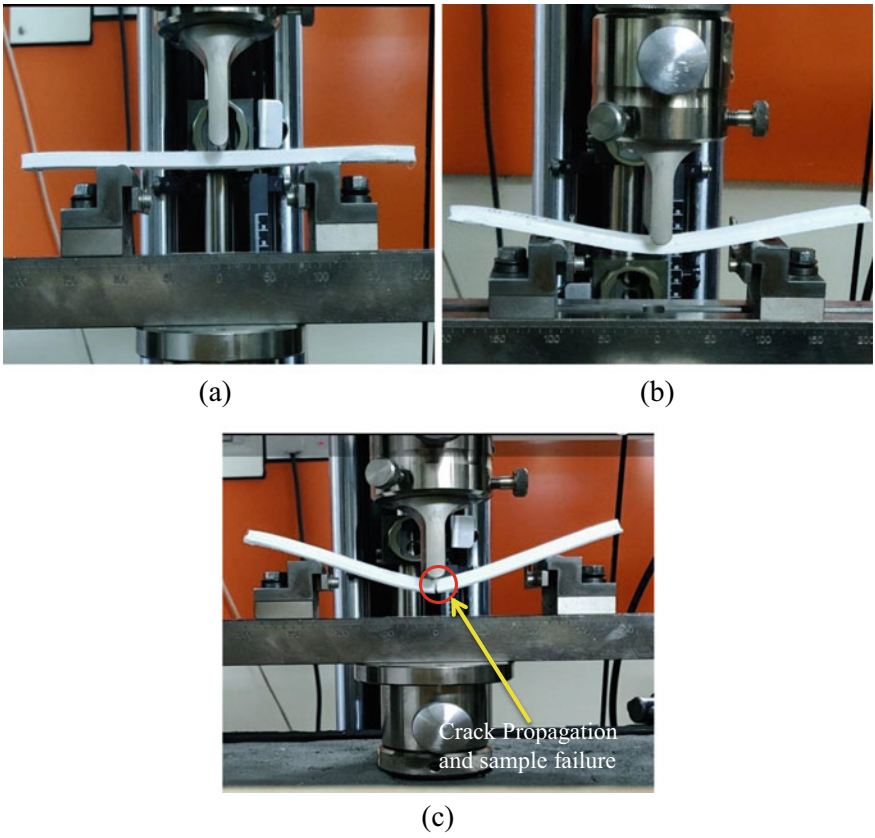

Fig. 5.5 **a** H60 in flexure mode, **b** deflection, and **c** discontinuity propagation [4]

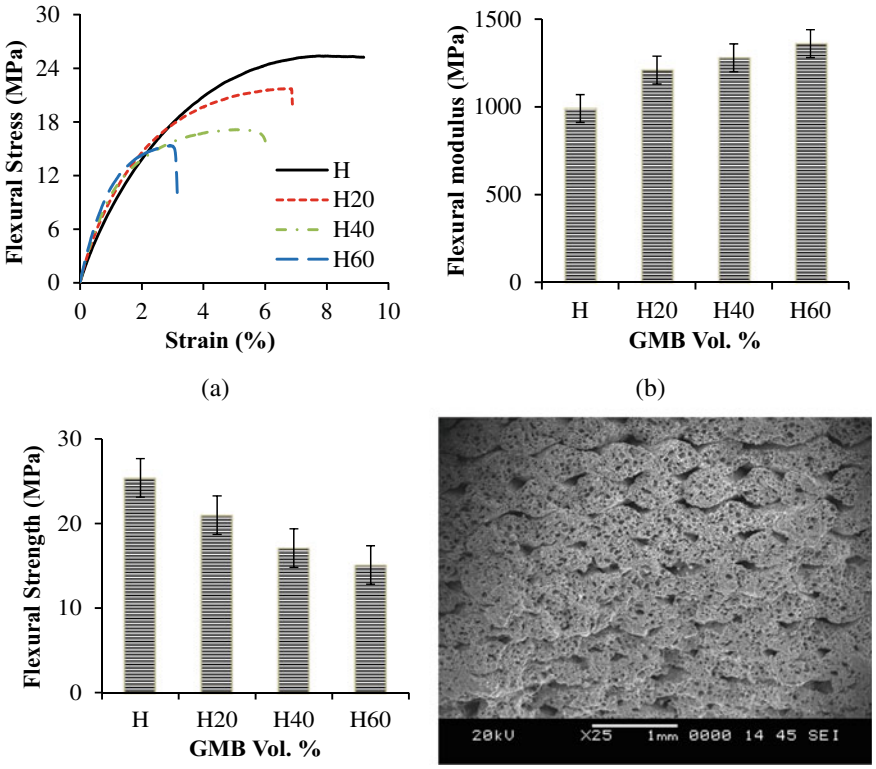

Fig. 5.6 Representative, **a** stress–strain plots for prints, **b** flexural moduli, **c** strength and **d** H60 micrograph showing raster gaps [4]

Table 5.5 Flexural responses [4]

Material	Moduli in MPa	Strength in MPa	Fracture strength in MPa	Fracture strain %	Specific modulus in MPa/kg/m^3	Specific strength in MPa/kg/m^3 $\times 10^{-3}$
H	990 ± 11.28	25.4 ± 0.12	–	–	1.068	27.40
H20	1210 ± 19.56	21.0 ± 0.58	20.34 ± 0.32	6.88 ± 0.09	1.465	25.42
H40	1280 ± 11.87	17.1 ± 0.47	16.89 ± 0.41	6.04 ± 0.11	1.716	22.92
H60	1360 ± 11.23	15.1 ± 0.72	15.00 ± 0.79	3.15 ± 0.07	2.036	22.60

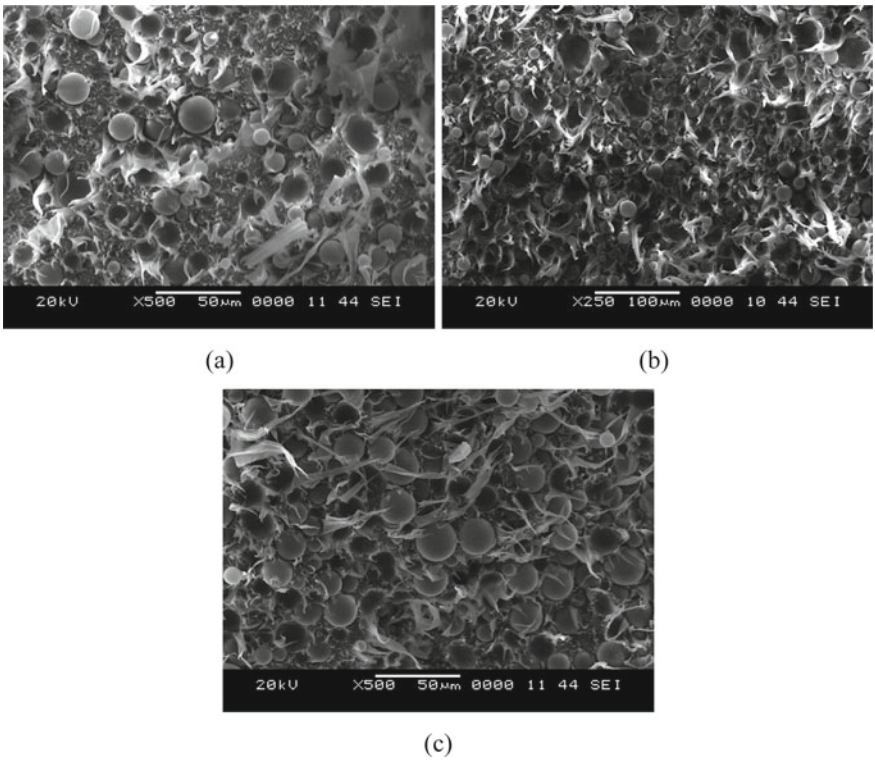

Fig. 5.7 Post-flexural tested printed, **a** H20, **b** H40, and **c** H60 cores [4]

restricted mobilities of polymer chains augmented by the weaker interfacial bondings. Enhancing constituents bonding with appropriately selected coupling agent may improve strength, compromising significant ductility reductions, which could impede filament extrusion and the 3DP process.

5.1.4.2 Property Map

The flexural behavior as a function of composites density manufactured utilizing different manufacturing techniques is shown in Fig. 5.8 [14–16]. GMB-based 3D printed foams have a density that falls between compression and injection-molded foams. The flexural modulus of GMB-based 3D printed composites is higher than that of conventionally manufactured syntactic foams (Fig. 5.8a). Composites made by compression and injection molding have similar flexural strength (Fig. 5.8b). Optimal extrusion and printing conditions with minimal filler breakage can be used to reduce density. Figure 5.8 shows how filler percent and printing settings can be used to manipulate flexural response over a wide range.

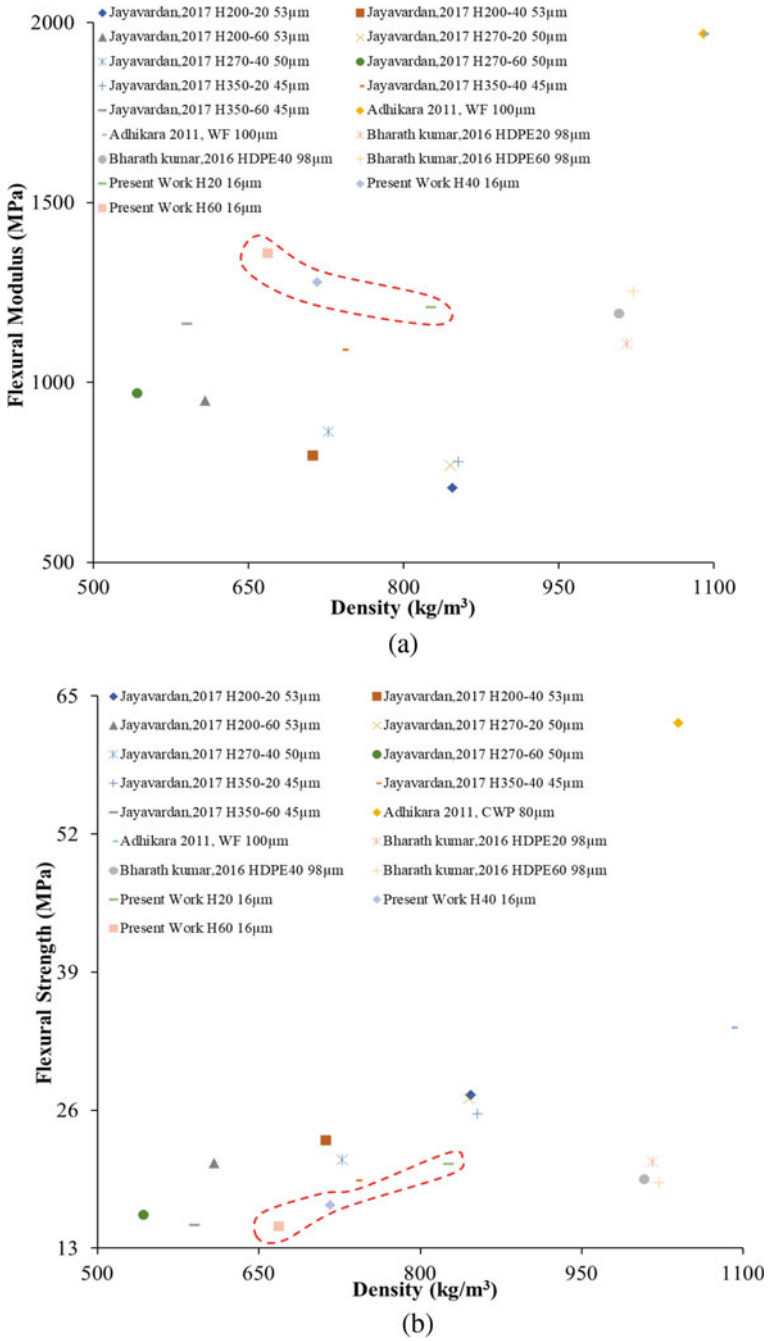

Fig. 5.8 Flexural, **a** moduli and **b** strengths of HDPE composite [14–16]

5.1.4.3 Flexural Behavior of 3D Printed Sandwich

Table 5.6 lists the physical properties of the 3D printed sandwiches. As the amount of GMB in the sandwich increases, the density of the sandwich lowers. Because of the additional HDPE layered skin on the foamed cores, the densities of SH20–SH60 are higher (6.45–8.36%) than the corresponding foam cores (H20–H60). In SH60, the highest weight reduction noted is 22%. With such higher weight reducing avenues, the synthesized SF-cored printed sandwich might potentially replace several components in buoyancy modules, providing increased specialized mechanical qualities and integrated geometrical features (without any joints).

Figure 5.9 shows the SEM of printed SF-cored sandwich flexural prints that have been freeze cracked. These micrographs show continuity in interfacial bonding at the core-skin interfaces in all the printed configurations, implying that the printing settings are suitable.

In the flexure of the sandwiches, the stress changes over the thickness, from compressive (topmost skin where the loading pointer hits) to tensile (bottom-most skin) region. Further, shearing force creeps in along the printed cupons length in traditionally produced sandwiches, leading to core-skins debonding and subsequent failure. As a result, the orientations of the origin and spread of cracks can be used to identify the different kinds of stresses that lead to failure Fig. 5.10 illustrates the yielding and midpoint deflections of an SH20. SH20 did not show failure until the test reached 10% strain and had the highest strength among the sandwiches. A brittle fracture was found in SH40 and SH60 (Fig. 5.11a). The discontinuity in sandwich composites starts in the bottom-most skin and travels along with the core below the loading point. Failure starts on the tensile side at the loading point and progresses to the compressive side. Due to the appropriate printing parameters used, similar failure features are seen for all printed SF core sandwich composites, avoiding shear failure/crack together with the deposited layers. The moduli rise as the GMB % rises (Table 5.7 and Fig. 5.11b). When compared to various sandwich compositions, SH60 has the highest modulus. The moduli of SH60 are enhanced by intact GMBs with greater filler loading, as seen in Fig. 5.12b. Flexural strength diminishes when GMB content in the core increases, as seen in Fig. 5.11c. SH20 and SH40 fully disintegrated into two pieces, displaying the typical brittle fracture. The strongest component is SH20, which may be attributed to efficient load transmission between the elements. The absence of plastic deformation in H, as seen in Fig. 5.12a, supports this conclusion. SH60 performs worse than SH20 due to excessive polymer deformation of

Table 5.6 Physical properties of the printed sandwiches [19]

Material	ϕ_f (vol.%)	ρ^{th} (kg/m^3)	ρ^{exp} (kg/m^3)	ϕ_V (%)	% Weight reduction compared to HDPE
SH20	20	879.35 ± 14	897.5	2.02	5.14
SH40	40	777.38 ± 16	845	8.00	16.14
SH60	60	723.87 ± 11	792.5	8.66	21.91

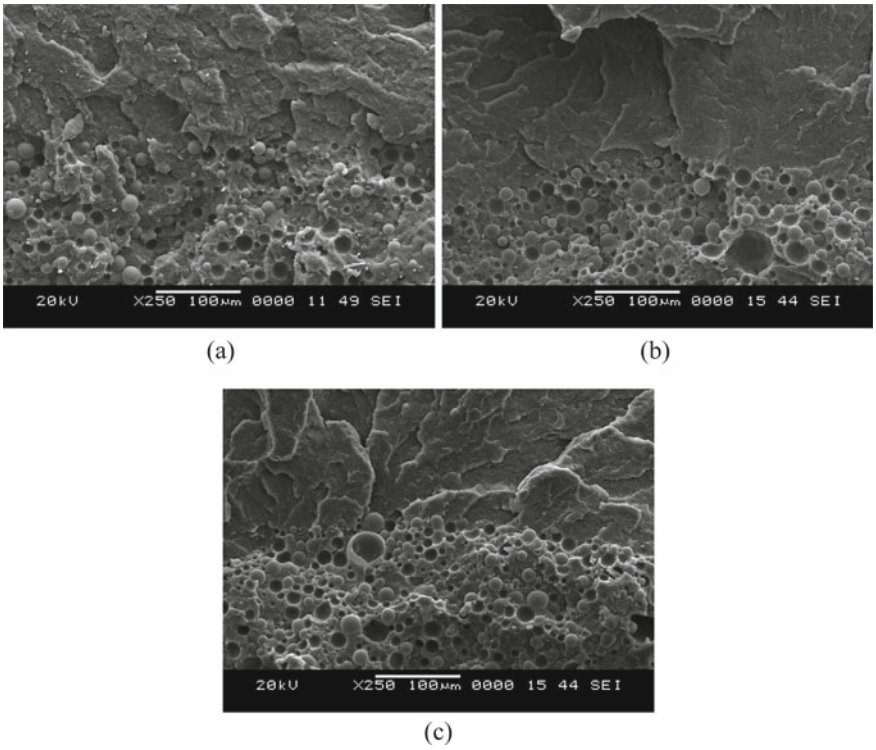

Fig. 5.9 SEM of sandwich, **a** H20, **b** H40 and **c** H60 at core-skin interfaces [19]

the matrices at higher filler %. Despite this, SH60's specific strength is 1.1 times greater than SH20's. The crack began in the mid-span in SH40 and SH60, spread vertically through the thickness of the core, and reached the upper HDPE skin. The increasing breakdown of the top skin reduces the rate of stress reduction and adds extra strain before failure. In shear stress, interfacial failure is a prevalent occurrence that has influenced sandwich composites. Nonetheless, due to excellent and seamless bonding, none of the concurrently printed SF core sandwiches described in this work showed interfacial separation/debonding between core and skin (Fig. 5.9).

5.1.4.4 Comparison of Core and Sandwich Flexural Properties

Comparing 3D printed sandwich composites' flexure properties to those of their corresponding cores. Figure 5.13 compares the flexural characteristics of the printed core and the corresponding sandwiches. Though the addition of GMBs reduces strength, it increases specific strength, which is a critical aspect in weight reducing scenarios. The strength of the sandwich cores is 1.05, 1.22, and 1.35 times more than that of the H20–H60 cores, respectively, indicating the potential benefit of

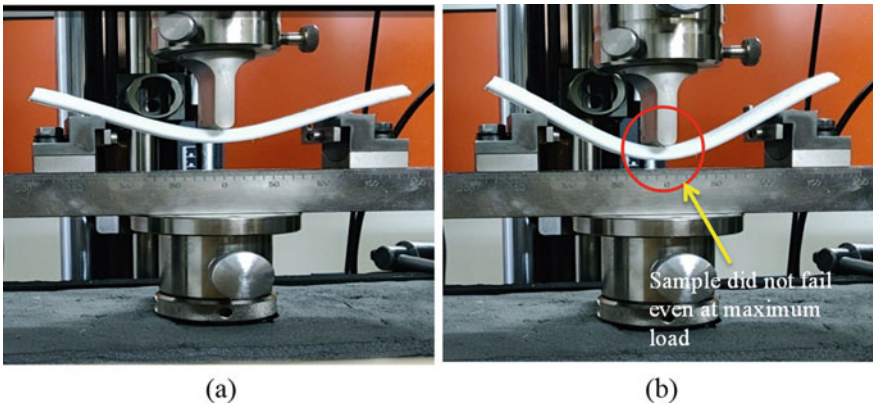

Fig. 5.10 SH20, **a** yielding and **b** midpoint deflection images [19]

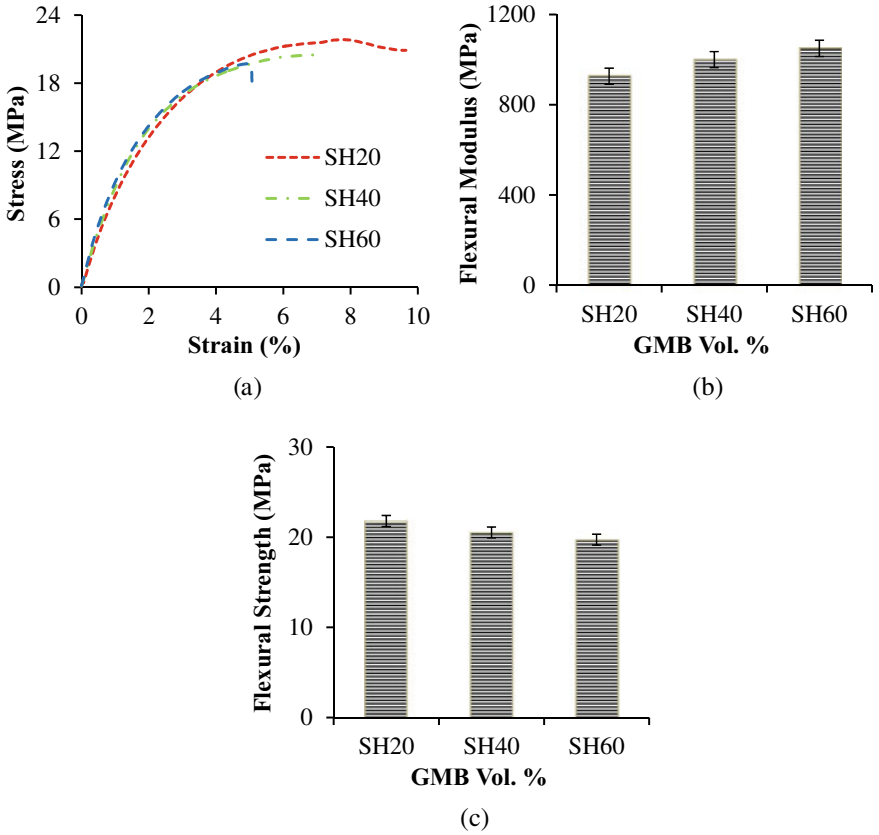

Fig. 5.11 **a** Stress–strain response, **b** moduli and **c** strengths in printed sandwich cupons [19]

Table 5.7 Flexural behavior of sandwich prints [19]

Materials	Experimental moduli in MPa	Theoretical moduli in MPa	Strength in MPa	Fracture strength in MPa	Fracture strain (%)
SH20	927 ± 18.46	1067.83	21.80 ± 0.45	–	–
SH40	1000 ± 13.58	1126.09	20.53 ± 0.52	20.25 ± 0.57	7.13 ± 0.15
SH60	1050 ± 12.86	1186.57	19.72 ± 0.80	19.72 ± 0.77	5.20 ± 0.10

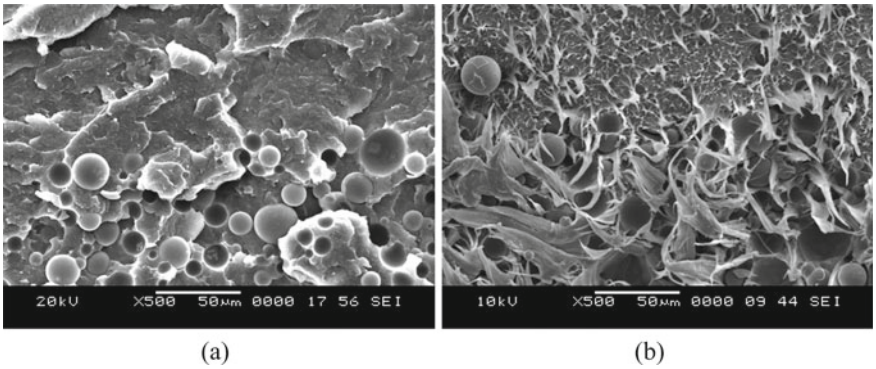

Fig. 5.12 Micrograph of post-flexural tested, **a** SH20 and **b** SH60 [19]

producing an SF-cored sandwich using 3D printing. Sandwich composites printed in 3D have 1.04, 1.17, and 1.18 times the flexural strength of cenosphere-based cores printed in 3D [20]. Based on the findings of this study's investigations, SH60 has the maximum specific moduli and strength magnitudes that can be employed for potential weight-saving scenarios without sacrificing mechanical behavior.

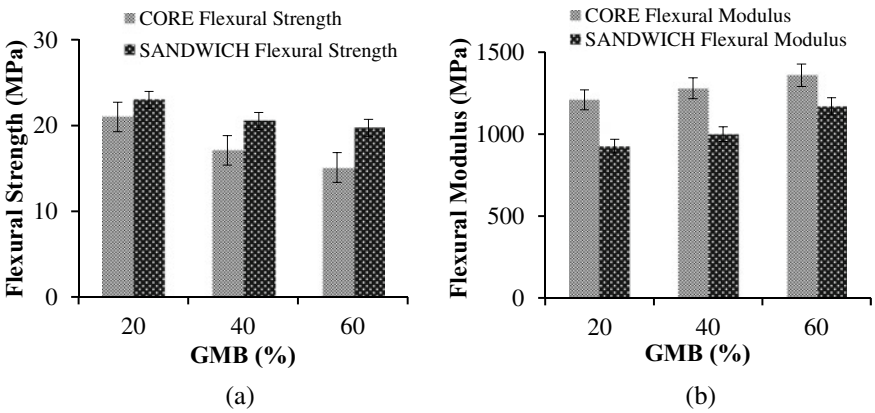

Fig. 5.13 Flexural, **a** strength and **b** modulus comparison for printed core and sandwich [19]

5.1.4.5 Theoretical Prediction of Sandwich Properties

Theoretical computations are based on the mechanics of composite beam theory [21]. The core and face sheets are assumed to be homogeneous in this hypothesis. A sandwich with a span length of L, a width of b, and a total thickness of h are shown in Fig. 5.14a. Two radius R rollers overhang the specimen kept far by a distance L, and load P is applied to the topmost layer via a radius R anvil. Theoretical moduli and failure loads values for printed SF-cored sandwiches are calculated using an experimental technique using the skin and core properties evaluated separately. Figure 5.14b shows the terms used for deducing theoretical values and comparative graphs for 3D printed sandwich composites.

The load is delivered progressively at the center in flexure loading circumstances, and the deflection includes skin and core deformation. When the wedge comes into direct contact with top skin in the presence of multiaxial stress, the mechanical characteristics of the top skin deteriorate. As a result, in theoretical deflection calculations, the thickness of the topmost skin where the load is applied is ignored [22, 23]. Equation 5.4 can be used to compute this deflection [24]. The sandwich's theoretical moduli, derived using the law of mixtures, can be used to measure the skin–core bonding efficiency of the properties of printed sandwich construction (Eq. 5.8). The total deflection at the midpoint equals sum of the deflections caused by face sheet

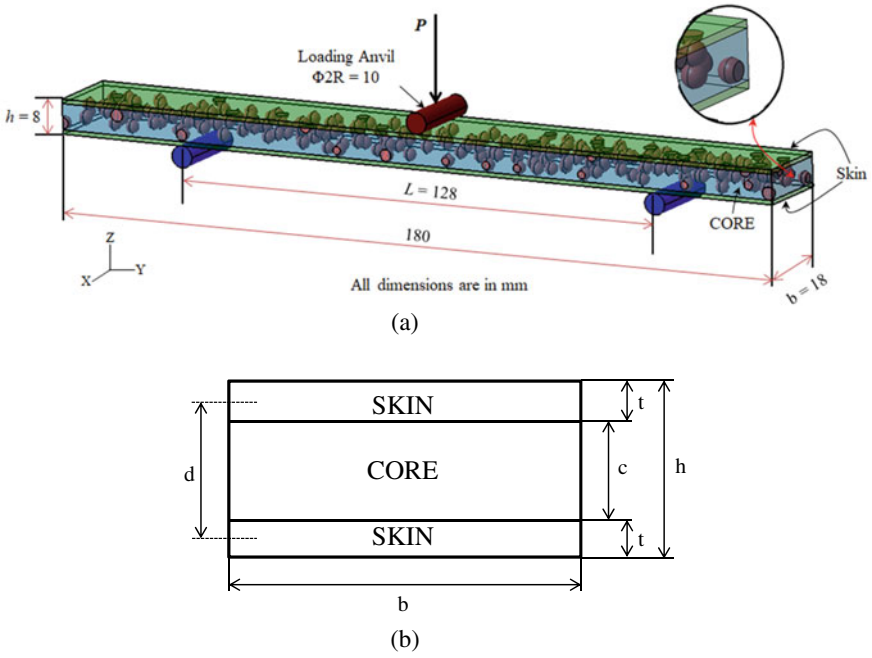

Fig. 5.14 **a** Dimensions and flexural test samples, **b** sandwich terminologies [19]

bending and core shear [25].

$$\delta = \frac{PL^3}{48(EI)_{\text{eq}}} + \frac{PL}{4(AG)_{\text{eq}}} \tag{5.4}$$

Here EI_{eq} is called flexural rigidity, which is estimated using Eq. 5.5 and $(AG)_{\text{eq}}$ is shear rigidity calculated using Eq. 5.6. The shear moduli of the core are (G_C) computed using Eq. 5.7.

$$EI_{\text{eq}} = \frac{bt^3E_s}{12} + \frac{btd^2E_s}{4} + \frac{bc^3E_c}{12} \tag{5.5}$$

$$AG_{\text{eq}} = \frac{bd^2G_c}{c} \tag{5.6}$$

$$G_c = \frac{E_c}{2(1+\mu)} \tag{5.7}$$

$$E = E_sV_s + E_cV_c \tag{5.8}$$

From Table 5.3, the skin and core moduli are taken. Table 5.7 provides values for the flexural modulus that are observed to be in good agreement between experimental and theoretical data (Fig. 5.15a). For SH20, SH40, and SH60, the theoretical and experimental modulus results differ by 13.18, 11.19, and 11.50%, respectively. The vacant contents in the printed sandwiches are to blame for these variances. Strength, in addition to sandwich rigidity, is quite important. Understanding the failure mechanisms covered in the subsequent section is necessary to calculate the critical loads reached for a sandwich post-elastic region. Equations 5.9, 5.10, and 5.9 depend on the neutral axis, the moment of inertias, the moment of resistance, and the failure load of the sandwich (Eq. 5.11).

$$Y = \frac{(A_sE_sY_s) + A_cE_cY_c}{(A_sE_s) + (A_cE_c)} \tag{5.9}$$

$$I_t = \frac{(E_cI_c + E_sI_s)}{E_c} \tag{5.10}$$

$$\sigma_{f\max} = \frac{nMY_{\max}}{I_t} \tag{5.11}$$

$$M = \frac{P}{2} \times \frac{L}{2} \tag{5.12}$$

The critical load estimates for printed sandwiches are shown in Table 5.8 and are shown to be lowering with increasing GMB volume percent. Larger void contents

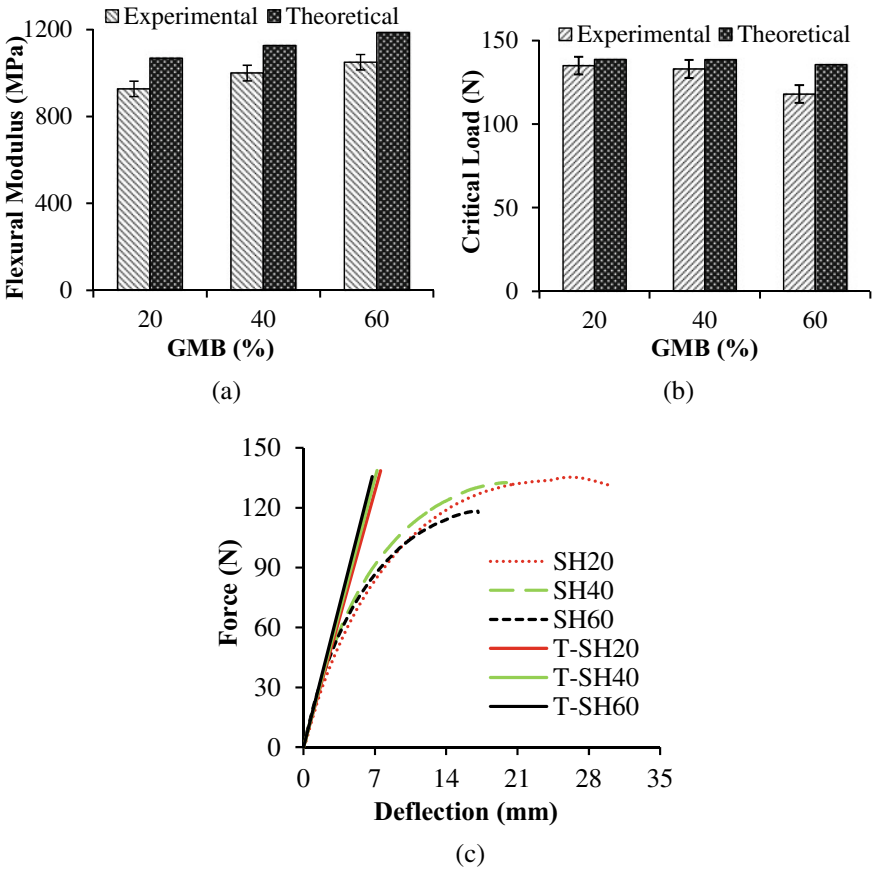

Fig. 5.15 Comparative analysis of **a** modulus, **b** critical loads, and **c** force–deflection response. *Note* T denotes "theoretical" [19]

with higher filler loadings are the cause of this. These gaps may create a three-phase SF shape and contribute to the damping property's improvement. Up to 50% of the maximum load, the difference between theoretical and experimental loads is reported to be in extremely good agreement (Fig. 5.15b). These theoretical methods aid in the prediction of the sandwich properties, which determine a wide range of potential applications. Figure 5.15c shows the load–deflection curves for both theoretical and experimental predictions.

5.1.4.6 Failure Mode of 3D Printed Sandwich

The skin shape, strength, and core material all play a role in the sort of sandwich failure [26]. Indentation, shear, and microbuckling/face wrinkling are the three probable failure modes in sandwiches under flexure. During core indentation and shear

Table 5.8 Critical loads [19]

Material	Experimental critical load (N)	Theoretical critical load (N) from Eq. 5.9	Deviation (%)
SH20	135	138.67	2.64
SH40	133	138.57	4.01
SH60	118	135.60	12.97

failures, the sandwich faceplates remain elastic [27]. As shown Fig. 5.16a, indentation occurs when compressive yield strengths match stresses developed across the core thickness. The overall indentation region is made up of the plastic indentation zones (λp—core reactive force = core compression strength) and the elastic indentation zones (λe—reactive force equals kw). The radial shear strain in the core surpasses the failure strain in the case of shear failure. Faceplate contribution has been overlooked in previous studies [25, 28], whereas circumferential hinges work has been taken into account [26]. The bottom skin fails first due to strain, whereas the top skin suffers from micro buckling and face wrinkles (compression side). Sandwiches with ductile skins collapsed in the bottom-most skin, while those with brittle skins failed in the top with microbuckling [29]. When a load is given to a sandwich construction, the skin usually experiences tensile/compressive failure, while the core usually experiences shear failure. For all the sandwiches examined, there is no shear. A linear indentation is detected where the wedge directly contacts the top skins, and as the load rises, compressive stresses are created on the top skin, causing wrinkling in the center for SH20 (Fig. 5.16c). As can be seen in the typical image Fig. 5.16d, indentation failure is detected in SH40 and SH60 samples in this study. In shear, none of the samples failed. Except for SH20, all the samples shattered in a nearly straight line slightly below the loading point (Fig. 5.16d). On the shattered surface of the top skin, the indentation is positioned in the designated area of Fig. 5.16d. Also, due to a higher proportion of stiffer GMBs inclusion resulting to brittle behavior, SH40 and SH60 show crack initiations at the bottom-most skin and shear failure of core. Except for shear, the printed sandwiches generated in this study show similar failure characteristics [24, 29, 30, 31].

5.1.5 Compression Response of Printed Cores and Sandwiches

The compression tests of 3D printed core and sandwich samples [32] are conducted using a Zwick (Zwick Roell Z020, ZHU) computer-controlled universal test system with a 20 kN load cell. The test is conducted at a constant crosshead displacement velocity of 0.5 mm/min. The criteria for the end of the test are set at 20 kN load. An in-house developed MATLAB code is used to analyze the data. The peak stress at the

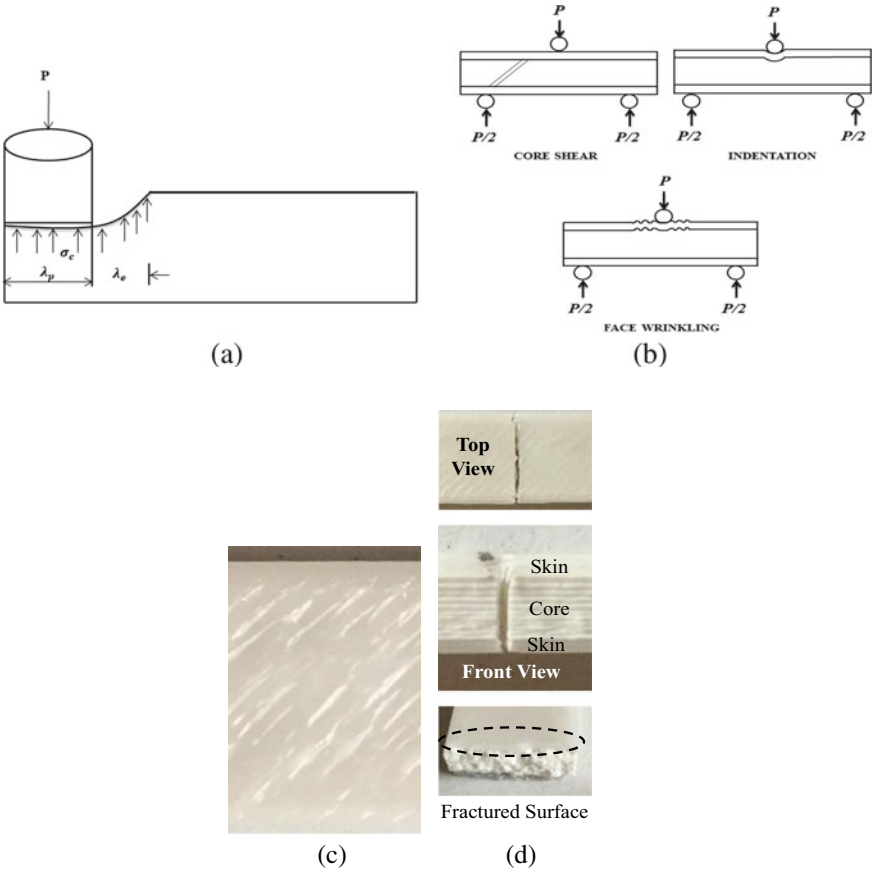

Fig. 5.16 **a** Core indentations and **b** failure mode observed sandwiches; **c** face wrinklings in SH20 and **d** SH40 and SH60 indentation failures [19]

end of the elastic region determines the compressive strength. At least five samples of each volume fraction are examined to ensure accuracy.

5.1.5.1 Compression Response of Printed Core Cupons

The compression test experimental setup is shown in Fig. 5.17a–c show the compressive stress–strain graphs of 3D printed neat HDPE and H20–H60. The compressive characteristics of the 3D printed core samples are estimated using MATLAB code written in-house, and the results are shown in Table 5.9. HDPE has a greater modulus and is 1.06 times higher than H60 because of its viscoelastic nature and lower glass transition temperature. Foam modulus rises as GMB content rises (Fig. 5.17e). H60 had the highest modulus among the foams, measuring 1.18 and 1.08 times that of H20

and H40, respectively. This is because intact GMBs are present at greater filler loadings. When compared to H60, HDPE yield strength was 1.23 times higher. Because of inadequate interface bonding between constituent pieces and raster gaps, SF's yield strength reduces (Fig. 5.17f) when filler loading increases. Due to decreased CTE, the volume of these raster gaps rises with filler loadings. H20 had the highest yield strength among the foams, possibly due to effective load transmission between constituents, and was 1.18 times stronger than H60. H60 performs worse than H20 due to severe plastic deformation of the matrix with increased filler loading. When subjected to compressive loads, the stress plateau is one of the most important characteristics of SFs and hollow particles. The stress plateau region becomes visible as the filler amount increases. The stress plateau region gets more evident as the GMB volume fraction increases. In the compressive stress–strain graph, the plateau region is noticeable in H40 and H60 when compared to H20 and is noted to be between 20 and 40% strain (Fig. 5.17c). Increased filler content boosts energy absorption at 50% strain in foams. H60 has a maximum energy absorption of 8.33 MJ/m^3 at 50%. Furthermore, as the load is increased, the plateau zone experiences a rise in stress with minimum deformation, leading to the strain hardening effect. This considerable rise in stress with smaller stresses is due to densification produced by the collapse of in-situ voids and hollow GMBs. When the load exceeds the plateau zone, the filler particles begin to collapse. The void area left following the collapse of GMB particles is filled by the HDPE matrix due to continuing compressive stresses, resulting in the densification phenomena. Foams have superior specific characteristics than clean HDPE (Table 5.10), indicating that they might be used in weight-sensitive applications. H60 had the highest specific modulus and strength among the foams, measuring 1.31 and 1.12 times that of HDPE.

The initial densification is triggered by the collapse of matrix porosities (Fig. 5.18a, c, e). GMB begins to break as the stress level grows, producing in additional densification. Deformed resin, intact GMB, and debris can be seen at higher magnification (Fig. 5.18b, d, f). There is no discernible difference in the look of the fracture surface for these materials in terms of strain rate because all compression samples are tested with constant crosshead displacement.

5.1.5.2 Compression Response of 3D Printed Sandwich Samples

The compression behavior of the 3D simultaneously produced sandwich samples is comparable to that of the core. The experimental setup for the sandwich SH60 sample under compression is shown in Fig. 5.19a. Figure 5.19b shows the stress–strain charts of 3D printed tidy sandwich samples. Sandwich compression properties are determined using in-house created MATLAB code, and the results are published in Table 5.11, just like foam core compression properties. Foam modulus rises as GMB content rises (Fig. 5.19d). SH60 has the largest modulus, 1.48 and 1.33 times that of SH20 and SH40, respectively. At greater filler loadings, intact GMBs improve SH60 moduli. Sandwich yield strength falls as filler loading increases (Fig. 5.19e) due to poor interface bonding between ingredients and raster gaps with increasing

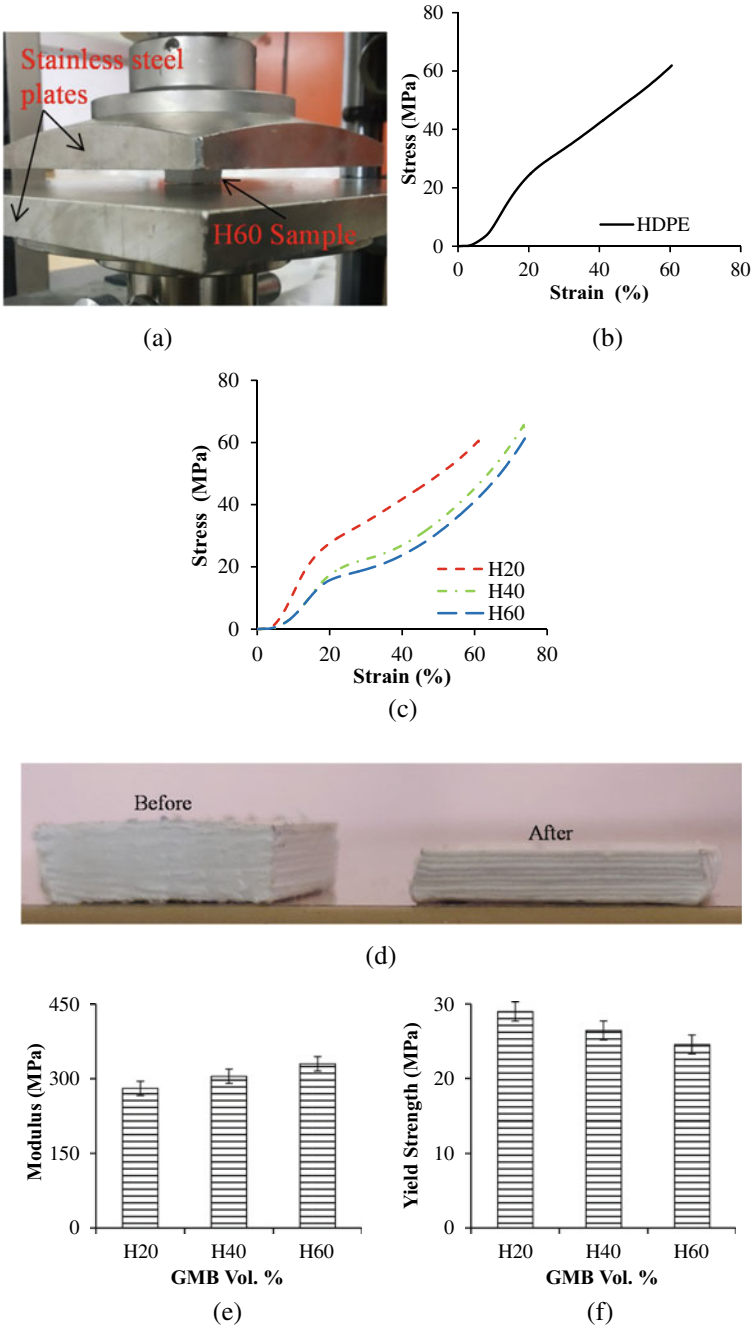

Fig. 5.17 **a** Experimental setup, **b** compressive stress–strain plots for HDPE, **c** foam, **d** H20—before and after compression, **e** compressive modulus and **f** yield strength as function of GMB vol.%

Table 5.9 Compressive response of printed H–H60

Material	Modulus in MPa	Yield strength in MPa	Yield strain (%)	Peak stress in MPa	Plateau stress in MPa	Energy observed at 50% strain (MJ/mm^3)
H	348.26 ± 10.35	30.25 ± 0.85	8.68 ± 0.19	68.54 ± 0.15	–	7.96 ± 0.55
H20	280.46 ± 12.25	28.98 ± 1.28	10.33 ± 0.24	59.85 ± 0.18	–	6.94 ± 0.26
H40	304.84 ± 11.58	26.45 ± 1.05	8.67 ± 0.15	66.42 ± 0.13	21.46 ± 0.02	7.49 ± 0.37
H60	329.95 ± 14.85	24.56 ± 0.98	7.44 ± 0.18	60.25 ± 0.09	19.73 ± 0.05	8.33 ± 0.48

Table 5.10 Specific compressive response of printed cupons

Material	Specific modulus ($MPa/kg/m^3$)	Specific yield strength ($MPa/kg/m^3$) × 10^{-3}
H	0.376	32.63
H20	0.339	35.08
H40	0.408	35.46
H60	0.494	36.77

filler loadings. The yield strength is reduced by excessive plastic deformation of the matrix at increased GMB concentration. The best strength is SH20, which could be related to efficient load transfer between the matrix and filler.

SH20 has a yield strength of 1.12 times that of SH60. With increasing filler material, the stress plateau region becomes more noticeable. Between 20 and 40% of strain, the plateau zone for sandwich SH20–SH60 can be found (Fig. 5.19b). The energy absorption at 50% strain in sandwiches increases as the filler amount increases. The energy absorption rate of 10.22 MJ/m^3 for SH60 is the maximum energy absorption among foams. SH60 has the highest specific moduli and strength (Table 5.12), allowing it to be used for weight-saving applications without sacrificing mechanical qualities.

The compressive properties of 3D printed sandwiches are compared to those of their respective cores. A comparison of yield strength between the printed core and the respective sandwiches is shown in Fig. 5.20a. Though the addition of GMBs reduces strength, it increases specific yield strength, which is important in weight-sensitive structural applications. SH20, SH40, and SH60 cores have yield strengths that are 1.22, 1.20, and 1.20 times greater than H20–H60 cores, respectively, demonstrating the potential benefit of 3D printing SF-cored sandwiches simultaneously. Sandwiches have a larger specific modulus than the core (Fig. 5.20b), which is an important design element when creating weight-sensitive structures.

The densification phenomena occur at higher stress with 1 mm HDPE skin at the top and bottom of the core in the sandwich because the HDPE skin resists the applied compressive load. The initial densification process begins when the maximum stress level is reached by collapsing the voids that have formed inside the core (Fig. 5.21a, c, and e). Additionally, when the stress level rises, GMB breaking occurs, causing

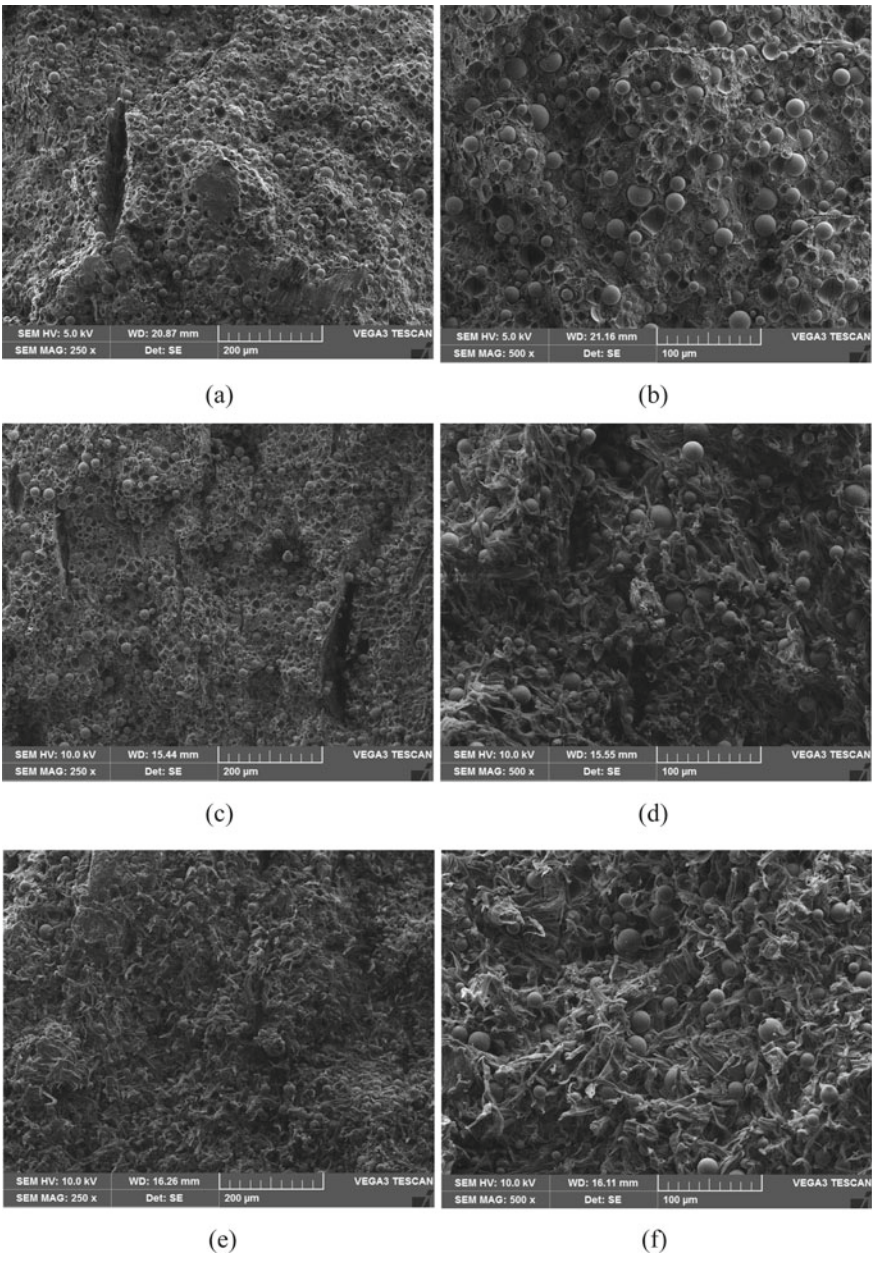

Fig. 5.18 Micrographs of compressive tested H20 (**a**, **b**), H40 (**c**–**d**), and H60 (**e**–**f**)

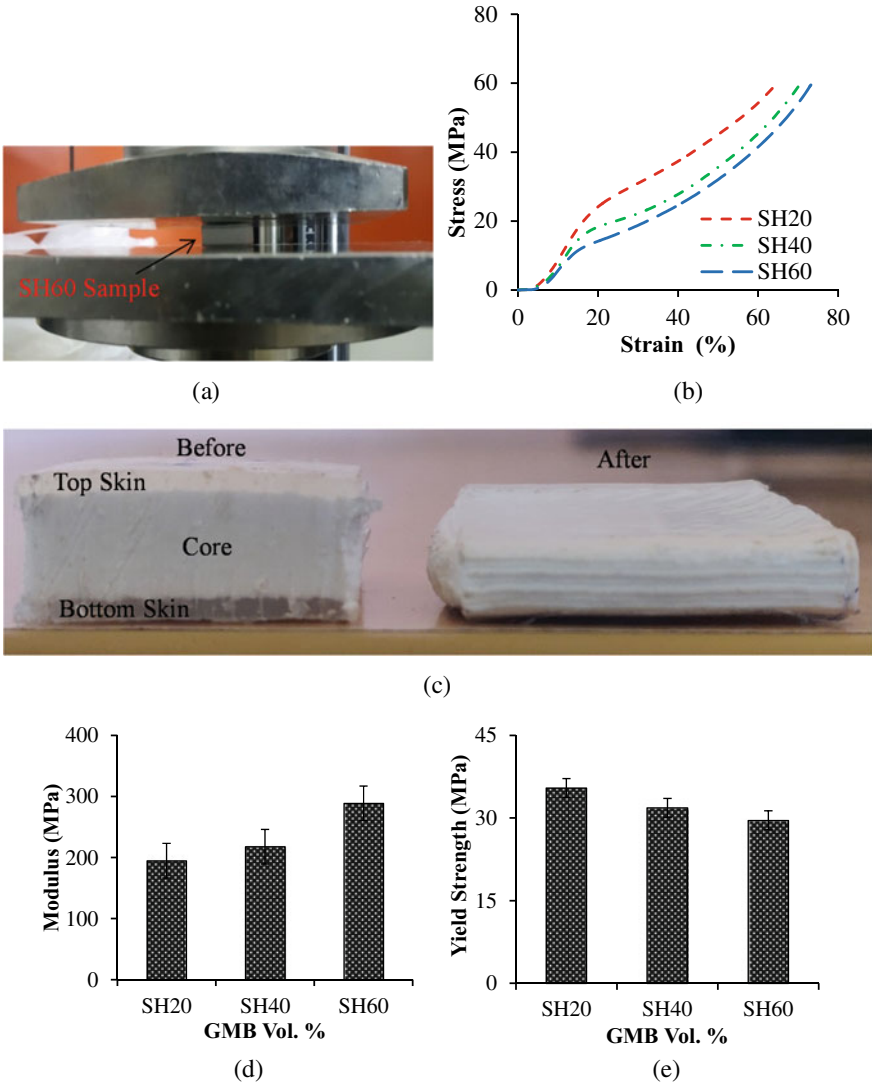

Fig. 5.19 **a** Experimental setup, **b** sandwich compressive stress–strain plots for 3D printed sandwich, **c** SH60 before and after compression, **d** compression modulus and **e** yield strength as function of GMB vol.%

additional densification. At higher magnification, Fig. 5.21b, d, f shows the deformed resin, intact GMB, and debris of sandwich samples. Despite this, due to the excellent and seamless bonding of skin and core, none of the printed SF-cored sandwiches showed interfacial separation between core and skin.

Table 5.11 Compressive behavior of printed sandwiches

Material	Modulus in MPa	Yield strength in MPa	Yield strain (%)	Peak stress in MPa	Plateau stress in MPa	Energy observed at 50% strain (MJ/mm^3)
SH20	194.67 ± 13.45	35.47 ± 1.05	20.71 ± 0.18	58.45 ± 0.12	23.56 ± 0.04	8.54 ± 0.36
SH40	217.62 ± 10.27	31.85 ± 0.98	16.21 ± 0.15	59.23 ± 0.11	19.45 ± 0.02	9.73 ± 0.27
SH60	288.83 ± 12.75	29.57 ± 1.20	10.23 ± 0.25	60.05 ± 0.17	17.68 ± 0.15	10.22 ± 0.58

Table 5.12 Specific properties of 3D printed sandwich samples

Material	Specific modulus ($MPa/kg/m^3$)	Specific yield strength ($MPa/kg/m^3$) × 10^{-3}
SH20	0.221	40.33
SH40	0.279	40.97
SH60	0.399	40.85

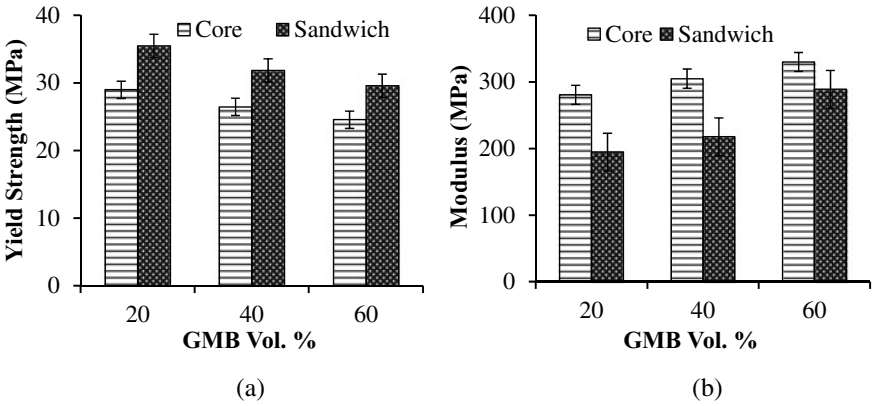

Fig. 5.20 Compression property comparison of 3D printed core and sandwich

5.2 Dynamic Tests

5.2.1 Buckling and Free Vibration Investigation

5.2.1.1 Buckling of 3D Printed Core

Buckling tests of printed H and SFs are carried out on a H75KS Tinius Olsen UTM at 0.2 mm/min crosshead displacements under axial compressive stresses. Samples with dimensions of 210 × 12.5 × 4 mm in length, breadth, and thickness were utilized in the buckling test [33, 34], with an average of five samples tested. Based on preliminary

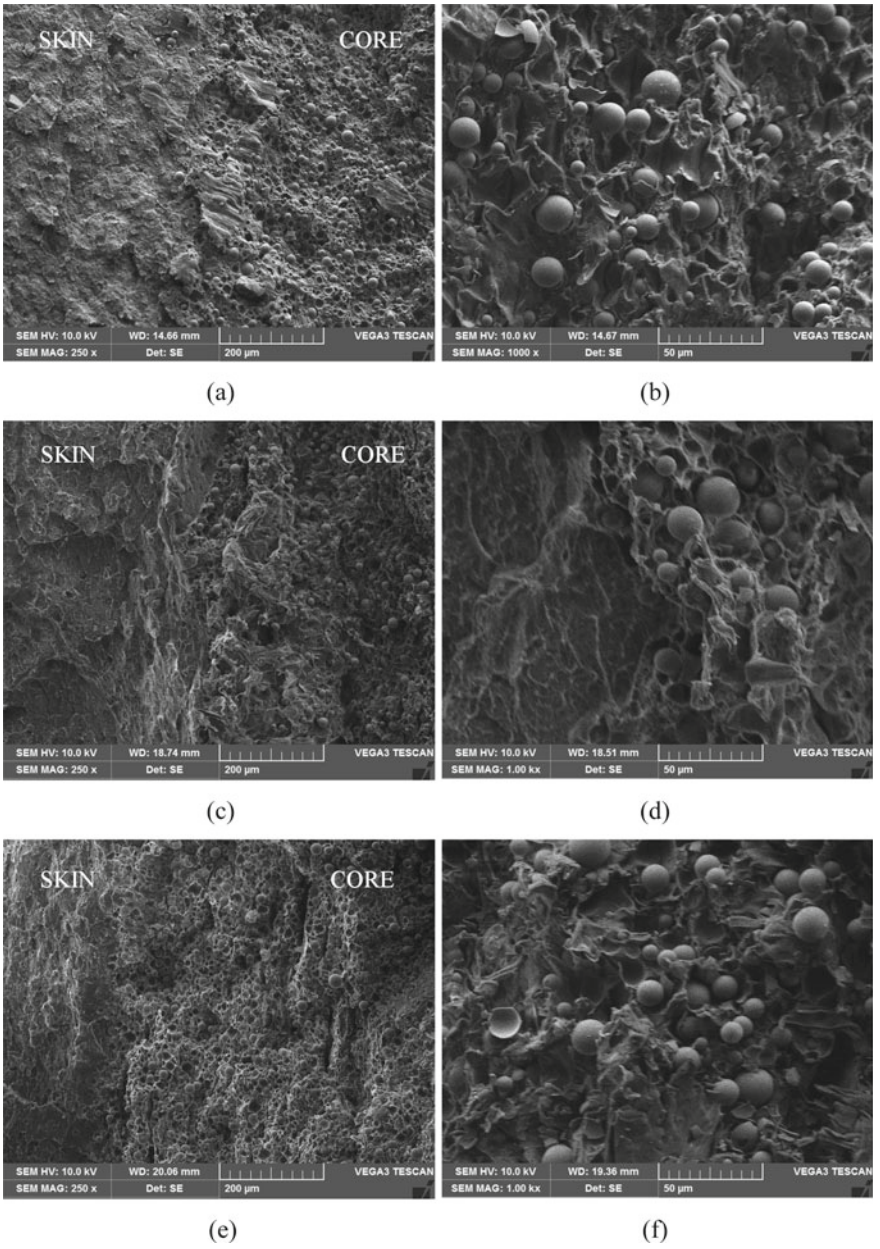

Fig. 5.21 Compressive tested SH20 (**a**, **b**), SH40 (**c**, **d**) and SH60 (**e**–**f**)

experiments, a 0.6 mm end shortening is taken into account to explore the behavioral changes in the post-buckling zone. The experimental layout for the mechanical buckling and free vibration under a compressive force is shown schematically in Fig. 5.22.

For the estimation of the critical buckling loads and to enable reliable structural designs, the DTM and MBC techniques are used. Figure 5.23 for a representative printed sample shows how to create tangents for load and deflection curves produced through experimental means for MBC and DTM methods [3, 37]. The DTM method involves drawing tangents in the post- and prebuckling regions. The critical load is determined by the intersection of two tangents, as shown in Fig. 5.23a. The critical buckling load value for the MBC approach corresponds to a position on the plot where the bisectors are drawn at the intersection points wherein both tangents meet (Fig. 5.23b). The vibration and buckling response of 3D printed H and associated SFs, both MBC and DTM methods, are presented for comparison.

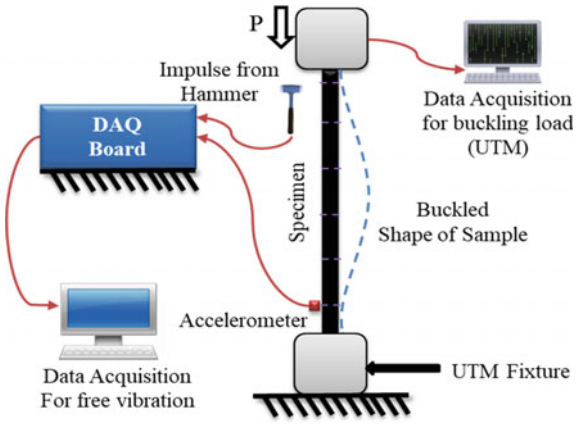

Fig. 5.22 Mechanical vibration and buckling setup [35, 36]

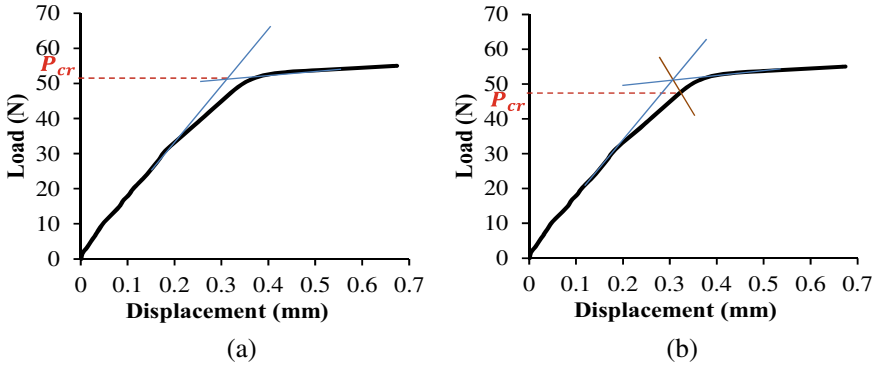

Fig. 5.23 Estimation of P_{cr} using, **a** DTM and **b** MBC for H20 prints [35, 36]

Figure 5.24 shows SEM of freeze-fractured printed H–H60 buckling and vibration samples. In the case of foams, all the cupons are printed using appropriate printing conditions (Table 5.13), resulting in a homogeneous dispersion of GMBs in the HDPE matrices. Figure 5.24 shows that the microballoons are intact after blending, extrusion, and printing, confirming the acceptability of the printing conditions utilized in this study.

The buckled mode forms of SF exhibit a typical global buckling behavior in the buckling investigations of 3D printed H and their associated foams. As shown

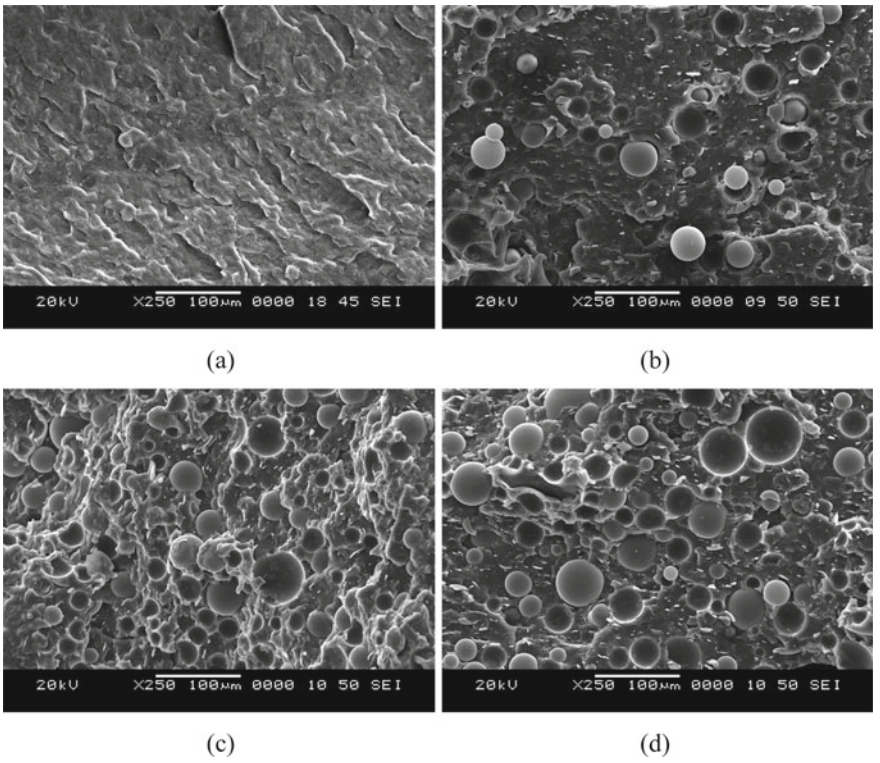

Fig. 5.24 SEM of fractured **a** H, **b** H20, **c** H40, and **d** H60 [35, 36]

Table 5.13 Experimental and theoretical P_{cr} [35, 36]

Material	Experimental P_{cr} in N		Theoretical P_{cr} (N)	Deviations in DTM (%)	Deviations in MBC (%)
	DTM	MBC			
H	50 ± 1.5	47 ± 1.3	57.88	13.61	18.79
H20	52.5 ± 2.4	48.41 ± 1.8	60.03	12.54	19.35
H40	68.3 ± 3.5	64.39 ± 2.6	81.19	15.87	20.69
H60	86.4 ± 3.4	83.45 ± 2.2	109.45	21.05	23.37

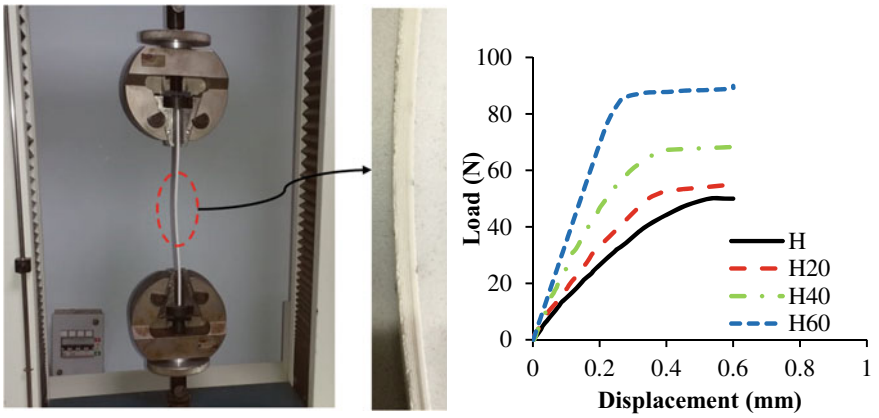

Fig. 5.25 **a** 3D printed foamed being tested and **b** plots showing buckling behavior of prints [35, 36]

in Fig. 5.25a, all buckling modes exhibit the greatest transverse defections in the center and no defection at the fixed end. Figure 5.25b depicts the observed buckling behavior of HDPE and foams, with the data summarized in Table 5.13. It's worth noting that the buckling load rises as GMB percent rises. This could be related to a rise in foam stiffness as the number of GMBs in the HDPE matrix rises. An increase in the load-bearing performance of composite with increasing GMB content can be related to a rise in critical buckling loads. Based on the Euler–Bernoulli assumptions [38], the theoretical P_{cr} for clamped–clamped H and foams therein is derived as,

$$P_{cr} = \frac{4\pi^2 E I}{L^2} \tag{5.13}$$

By the Bardella–Genna model, E is the modulus. The moduli of GMBs are many times higher than that of H, resulting in a larger critical load for SFs. For HDPE, the experimentally deduced critical load is 50 N. In DTM and MBC techniques, the P_{cr} of H20, H40, and H60 is increased by 5, 36.5, 72.9, and 3.01, 37.03, 77.6%, respectively, than H. DTM estimates a greater critical buckling load than MBC. The difference between them is approximately 3–8%. The buckling load computed theoretically of neat H is 57.89 N, which increases by 3.72, 40.26, and 89.08% in H20–H60, respectively. The theoretical and practical buckling loads are very similar at smaller filler amounts. The void volume fraction increases as the filler content increases, resulting in greater discrepancies in experimental and theoretical results. Both H and foams therein did not fracture due to layers delamination, according to the buckled mode shapes (Fig. 5.25a). This is due to the high quality of composites created using the proper printing conditions.

Table 5.14 Comparative values of moduli [35, 36]

Material	Young's modulus in MPa		% Deviation
	Equation 2.11	Equation 5.18	
H	970.05 ± 13	970.05	–
H20	1031.10 ± 26	1012.6	1.79
H40	1415.30 ± 24	1376.1	2.76
H60	1887.22 ± 30	1874.1	0.69

Table 5.14 lists the moduli obtained from Bardella–Genna (Eq. 5.18) and the frequency for high density polyethylene and their foams. The moduli of H20–H60 are enhanced by 6.28, 45.88, and 94.53%, respectively, when compared to H. As GMB content rises, modulus rises as well, providing greater resistance to buckling. The presence of GMBs in HDPE matrices boosts the inherent frequencies of SFs. According to Eq. 5.18, the variance in Young's moduli for H20–H60 computed from Eq. 5.18 and frequency data is 1.78, 2.68, and 2.23%, respectively. The natural frequency of SF is increasing when stiffer GMB particles are added, perhaps increasing the overall stiffness of the foams.

5.2.1.2 Free Vibration of 3D Printed Core

The first three natural frequency of the printed high density polyethylene and their foamed beams under axial compression loads with clamped–clamped circumstances are recorded (Fig. 5.26). By stimulating the samples with a 9722A2000 Kistler impulse device with a sensitivity of 10 mV/N, a uniaxial accelerometer (8778A500) with 10 mV/g sensitivity and a 500 g operational range is utilized to observe the vibration data. The accelerometer is attached to the specimen using beeswax. DEWESoft program records response signals and transforms time to frequency-domain signals to compute natural frequencies and mode using a rapid Fourier transform technique. The modal analysis is carried out in the experimental route with 20 N load increment until the cupon deflection reaches 0.60 mm.

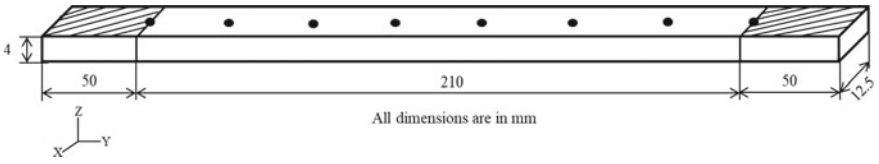

Fig. 5.26 Schematic diagram of specimen used in free vibration test [35, 36]

5.2.1.3 Baadella–Genna Approach for Estimating Moduli

Using the Bradella–Genna model [39] the modulus of high density polyethylene and foam cupons is calculated, and the findings are compared to experimental values. The following equations describe the homogeneous approach used by this model to predict the shear and bulk modulus.

$$K_{\text{bulk}} = K_m \frac{\delta(1+\Phi_\Upsilon)+k(1+\Phi_\Upsilon)}{\delta(1-\Phi)+k(\Upsilon+\Phi)}, \tag{5.14}$$

where

$$\gamma = \frac{4G_m}{3K_m} \tag{5.15}$$

$$\delta = \frac{4G_f}{3K_m}(1-\eta^3) \tag{5.16}$$

$$K = \frac{4G_f}{3K_f} + \eta^3. \tag{5.17}$$

The HDPE matrix's moduli and Poisson's ratio are taken as 810.25 MPa (Table 5.3) and 0.425 [14], respectively. Poisson's ratio and moduli of GMBs are respectively taken as 0.21 and 60,000 MPa [40]. The GMB particle radius ratio is computed using true particle density and GMB densitys, [38] and is 0.914. The shear moduli are obtained from Eq. 5.18, as mentioned in Reference [41]. The foam moduli are estimated using (Eq. 5.18) [42].

$$E = \left(\frac{\omega_j}{\beta_j^2}\right)^2 \left(\frac{\rho^{\exp} A L^4}{I}\right), \tag{5.18}$$

$$\text{where} \quad \omega_j = 2\pi f. \tag{5.19}$$

The density of the syntactic foams and Poisson's ratio are calculated using the rule of mixtures. The constant β_j Eq. 5.18 represents a specific mode, and under clamped–clamped boundary conditions, it is assumed to be 4.73 for the first mode [19]. The voids found in the samples are thought to be the volume that the matrix occupies in this scenario. Equation 5.20 is used to get the foam's Young's modulus.

$$E = \frac{9KG}{3K+G} \tag{5.20}$$

5.2.1.4 Theoretical Estimations

The spherical shape of the hollow GMB particles and the uniform dispersion of the GMBs in the HDPE matrices have been observed. Consequently, the composite of GMB and high density polyethylene SF can be modeled as isotropic materials. Additionally, it is anticipated that SF will behave as linearly elastic. The differential beam equations for the motion under axial compression while ignoring shear deformations and rotating inertial effect are given by [43]

$$EI\left(\frac{\partial^4 y(X)}{\partial X^4}\right) + P\left(\frac{\partial^2 y(X)}{\partial X^2}\right) - \rho A\left(\frac{\partial^2 y}{\partial t^2}\right) = 0, \tag{5.21}$$

where $y = y(x, t)$ and for the beam's natural mode of oscillation. Equation 5.21 presents the governing differential equations of beam motion which is subjected to an axial compression force developed based on Euler–Bernoulli hypothesis. The first term in this equation denotes the beam's bending stiffness, the second term reflects the work done by the applied axial forces, and the final term denotes the beam's inertia force.

$y(x, t) = Y(x)\cos\omega t$, then Eq. 5.21 becomes,

$$EI\left(\frac{\partial^4 Y(X)}{\partial X^4}\right) + P\left(\frac{\partial^2 Y(X)}{\partial X^2}\right) - \rho A\omega^2 Y(X) = 0. \tag{5.22}$$

The solution for Eq. 5.22 can be mentioned by taking into considerations dimensionless beam coordinates $\zeta = \frac{x}{l}(0 \le \zeta \le L)$.

$$Y(X) = Y(I\zeta) = D_1 \sin\mathrm{h}M\zeta + D_2 \cos\mathrm{h}M\zeta + D_3 \sin N\zeta + D_4 \cos N\zeta, \tag{5.23}$$

where D_1, D_2, D_3, and D_4 are constant coefficient, M and N can be put forth as,

$$M = L\sqrt{\left\{-\left(\frac{P}{2EI}\right) + \left[\left(\frac{P}{2EI}\right)^2 + \left(\frac{\rho A}{EI}\right)\omega^2\right]\right\}} \tag{5.24}$$

$$N = L\sqrt{\left\{\left(\frac{P}{2EI}\right) + \sqrt{\left[\left(\frac{P}{2EI}\right)^2 + \left(\frac{\rho A}{EI}\right)\omega^2\right]}\right\}} \tag{5.25}$$

$$M = \sqrt{\left(-V + \sqrt{V^2 + \Omega^2}\right)} \tag{5.26}$$

$$N = \sqrt{\left(V + \sqrt{V^2 + \Omega^2}\right)} \tag{5.27}$$

where $V = \frac{PL^2}{2EI}$; $\alpha = \sqrt{\frac{EI}{\rho A}}$ and $\Omega = \frac{\omega L^2}{\alpha}$.

By differentiating Eq. 5.23, we get,

$$\frac{dY}{dX} = MD_1 \cos h M\zeta + MD_2 \sin h M\zeta + ND_3 \cos N\zeta - ND_4 \sin N\zeta \tag{5.28}$$

$Y(x) = 0$, $\frac{dY(0)}{dx} = 0$, $(L) = 0$ and $\frac{dY(L)}{dx} = 0$ are the boundary condition for the clamped–clamped regime. The substitution of the boundary condition in Eqs. 5.23 and 5.28 leads to a non-trivial solution. By taking zero determinant of the coefficients for the non-trivial solution,

$$\begin{vmatrix} 0 & 1 & 0 & 1 \\ M & 0 & N & 0 \\ \sin h M & \cos h M & \sin N & N \\ M \cos h M & M \sin h M & N \cos N & -N \sin N \end{vmatrix} = 0 \tag{5.29}$$

$$\left(M^2 - N^2\right) \sin N \sin h M + 2MN(1 - \cos N \cos h M) = 0 \tag{5.30}$$

Substituting the M and N values in terms of Ω and V in Eqs. 5.30,

$$\Omega - V \sin \sqrt{\left(V + \sqrt{V^2 + \Omega^2}\right)} \sinh \sqrt{\left(-V + \sqrt{V^2 + \Omega^2}\right)} - \Omega \cos \sqrt{\left(V + \sqrt{V^2 + \Omega^2}\right)} \cosh \sqrt{\left(-V + \sqrt{V^2 + \Omega^2}\right)} = 0 \tag{5.31}$$

The characteristic equation for the compressive load, represented in Eq. 5.31, provides variation in natural frequencies. Equation 5.30 is numerically solved using MATLAB code, and the results are obtained frequency-compressive load graphs that are compared to experimental values.

The free vibration behavior of neat HDPE and SFs, which have been tested for their buckling strengths under axial compressive forces, has been researched. As illustrated in Fig. 5.26, the printed cupons are divided into eight equal portions along their length. The frequency response function (FRF) is determined by utilizing a roving impact hammer to excite the prints at the various indicated points and then measuring the related reaction with an accelerometer. The analytical solution produced by solving Eq. 5.31 is compared to the natural frequencies associated with the first three forms of bending modes. FRFs obtained with DEWESoft software are used to determine the natural frequencies for the first three modes. Figure 5.27 shows a typical FRF curve for H60. As the compressive force increases, the inherent frequency of all prints tends to decrease. Maintaining a constant compressive load throughout time is required to measure free vibration response effectively and accurately under the imposed compression, which is accomplished by incrementing the load program in the UTM by 20 N.

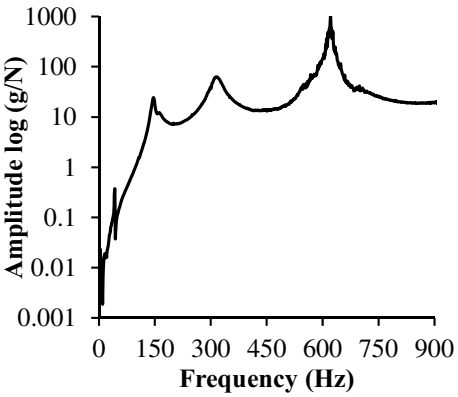

Fig. 5.27 FRF of H60 at no-load condition [35, 36]

The load is kept constant for 2 min after each increment, during which the free vibrations test is conducted. The load is increased until the print is strong enough to bear the imposed compressive load. The critical buckling loads are usually slightly higher than this load. The first natural frequency at the buckling region increases in the post-buckling zone because of the attainment of geometric stiffnesses and the beam deflections. Previous research has found a similar pattern in isotropic/composite beams and columns [44]. Under axial compressive loads is same as P_{cr}, the 1st natural frequency of H–H60 results in almost zero theoretically (Fig. 5.28). Due to the structural stiffness loss of printed cupons as the compressive force approaches the P_{cr}, the first natural frequency rapidly decreases.

5.2.1.5 Vibration Correlation Technique (VCT)

A vibration correlation technique, the non-destructive method, is used to estimate critical buckling loads from the prebuckling stage for composite beams (VCT). There are two sorts of VCT techniques: direct and indirect approaches [45]. The indirect method extrapolates an experimental functional relationship between the applied compressive load and the natural frequency to estimate the buckling load [45], whereas the direct method depends on the utilization of experimental functional relationships between the applied compression and the natural frequencies. The buckling load of the 3D prints is extrapolated using a straightforward approach in this study. Using the vibration correlation technique (VCT), the critical load of high density polyethylene and SFs is estimated from vibration data [46–49]. It's a non-destructive test that uses vibration data to compute critical load. The natural frequency is determined empirically using a compressive load that is less than the critical load in this method. The process is repeated for multiple load trials, and the technique's accuracy is based on the estimation of critical load using data corresponding to lower compressive loading levels. Figure 5.29a plots the squared values of fundamental frequencies against compressive load to indicate the critical load

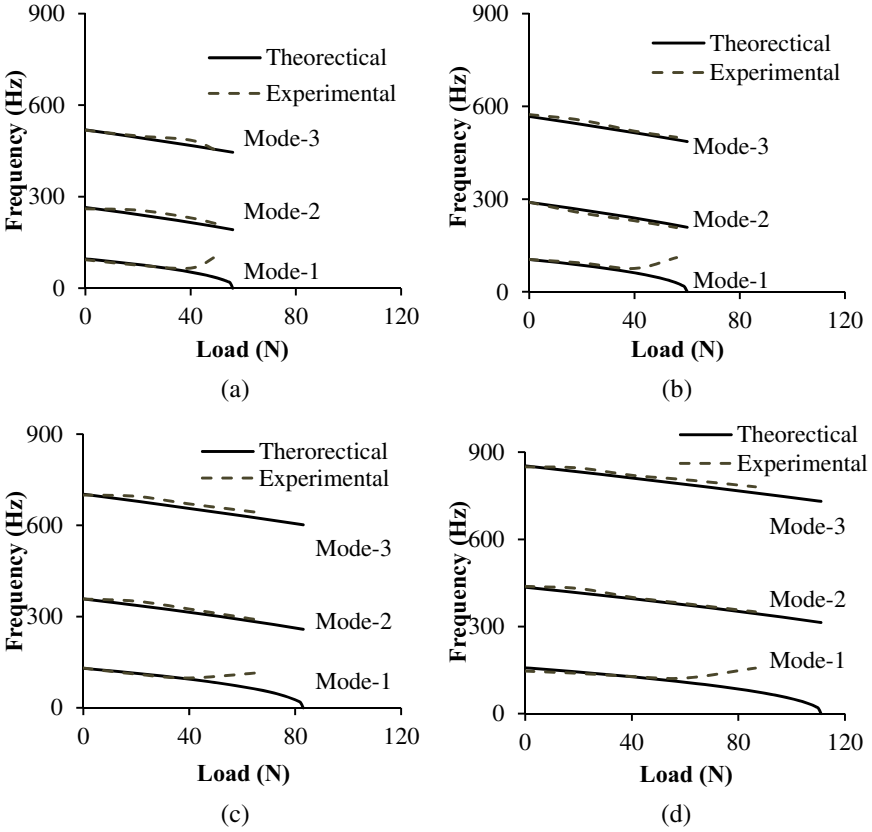

Fig. 5.28 Natural frequencies of **a** H, **b** H20, **c** H40 and **d** H60 [35, 36]

for H–H60. The plot is extrapolated to obtain critical loads using a second-order polynomial expression (Eq. 5.32).

$$\left(\frac{f}{f_n}\right)^2 = 1 - \left(\frac{P}{P_{\text{cr}}}\right), \tag{5.32}$$

where f_n and f are fundamental frequencies at no stress and compressive load, respectively, and P.

For variation in GMB content, Fig. 5.29b shows a comparison of critical buckling loads computed using DTM, VCT, and MBC techniques. The buckling load projected for each design from VCT rises with an increase in GMB %, as observed in buckling trials. The buckling load assessed using VCT is found to be closer to that computed using DTM and MBC techniques for H and H40. VCT, on the other hand, overestimated the buckling loads in the H20 and H60 cases. The comparison

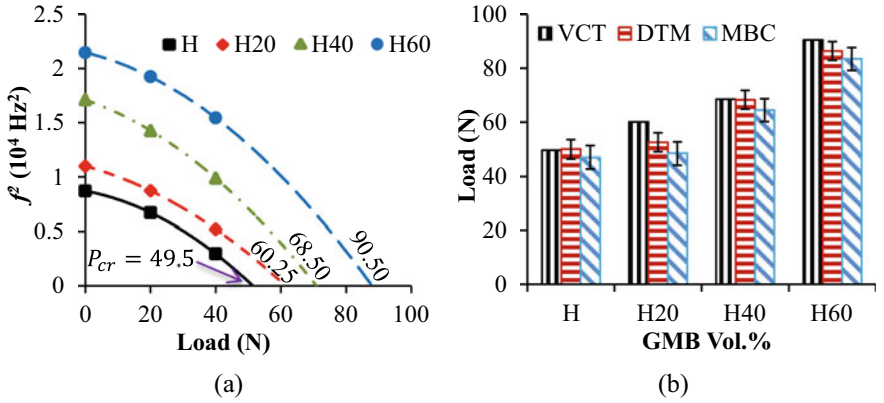

Fig. 5.29 **a** P_{cr} for H–H60 using VCT and **b** comparison through DTM, VCT, and MBC [35, 36]

of these methodologies aids in determining the values range with lower and upper bounds within which deviations are likely to occur.

5.2.1.6 Property Map

Composite density is a critical component in lightweight applications, and the lower density of SFs allows them to be utilized in weight reducing regimes. The buckling load as a function of composite densities is shown in Fig. 5.30 from the literature [33, 44]. The data on thermoplastic-based SFs produced using traditional manufacturing processes cannot be compared to data on 3D printed foams. As a result, 3D printed thermoplastic SFs are compared to thermosetting SFs in this section. Figure 5.30 shows data on density and buckling load gathered from the literature for fly ash cenosphere reinforced epoxy foams (untreated and treated) and natural fiber embedded thermosetting composites.

To produce structural components exposed to axial compressive load where the mechanism of failure is largely buckling, it is critical to choose the right matrices, fillers, and volume %. Natural fiber and GMB-based SFs are shown to be more prone to buckling failure than cenosphere foams. As previously stated, 3D printed thermoplastics are being compared against epoxy (thermosetting) SFs in this study. Nonetheless, a comparison like this can help industrial practitioners and designers understand the wide variety of values that exist between thermoplastic and thermosetting foam regimes. The higher performance of printed H60 than woven natural fabrics thermosetting composite is a very intriguing aspect to notice from this comparison, demonstrating the potential of the printed H60. 3D printed GMB/HDPE SF integrated lightweight functional components with complex geometrical designs can replace a few printed components subjected to axial compressive loadings in the automotive, aerospace, and marine industries.

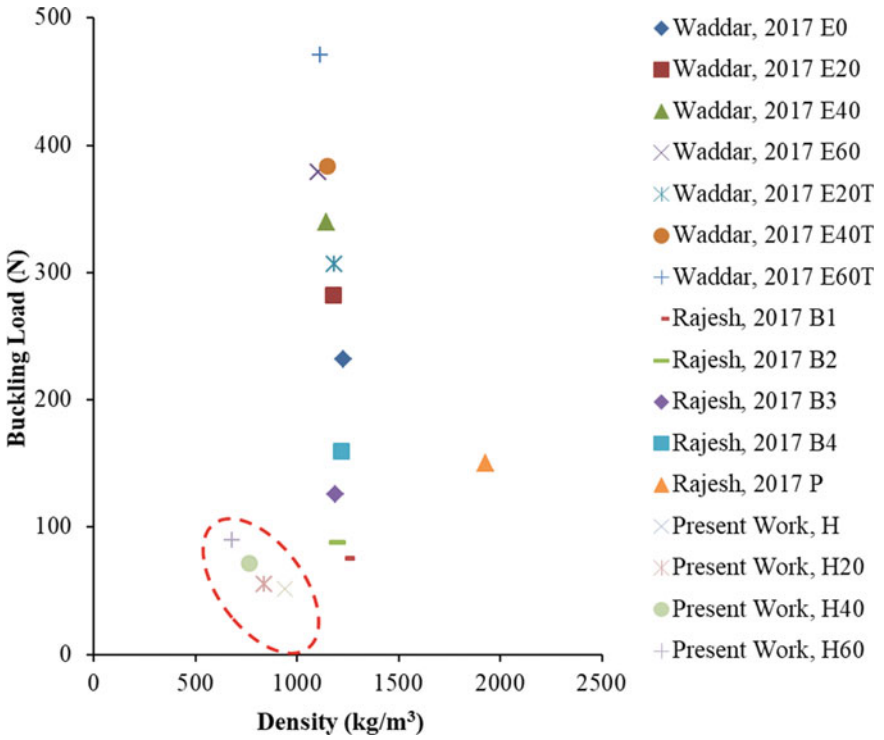

Fig. 5.30 Buckling loads versus density [33, 44, 50]

5.2.1.7 Buckling and Free Vibration of Printed Sandwiches Under Axial Compression

As the actual stress at the site of failure is significantly less than the material's capacity to withstand the applied loads, buckling analysis has become more and more crucial, especially in engineering design safety [51]. The H75KS UTM from Tinius Olsen, UK, with a 50 kN loading capacity, is used to conduct buckling investigations with a 0.2 mm/min crosshead displacements. The sandwich sample buckling test setup is shown in Fig. 5.31a. To observe the behavioral deflections, change in both the post- and prebuckling situations, the end shortening is restricted to 0.70 mm. Using load and deflection information obtained from a universal testing machine [52, 53], the experimental P_{cr} is visually approximated using the Modified Budiansky Criteria (MBC) and double tangent method (DTM) techniques. The point of intersection of the two tangents, P_{cr}, is taken into consideration when applying DTM to load–deflection curves, which are typically generated from the post-buckling and prebuckling regimes. A point that cuts through the two tangents drawn to the load-deflections plot is the focus of the P_{cr} MBC [50]. Due to their ability to forecast lower and upper bounds, the MBC and DTM are both frequently employed for P_{cr} predictions. Thus,

similar techniques are also used in the current work. The experimental setup utilized to determine the fundamental frequencies using modal analysis for the first three bending modes of concurrently manufactured sandwich composites with clamped–clamped boundary constraint is depicted in Fig. 5.31a. The response is acquired using a lightweight Kistler accelerometer (sensitivity: 10 mV/gm, operational range: 500 gm), which is excited using Kistler's impulse hammer (10 mV/N sensitivity). As previously noted, beeswax is utilized to improve the adherence of the accelerometer with the samples. With the aid of DEWE Soft, FFT is used to transform time-domain signals into frequency-domain signals. FRF is calculated at various points in the length breadth region, as shown in Fig. 5.31b. The frequency and vibration mode forms are directly provided by the DEWE Soft. To extract the mode shapes, the test is advanced from zero (the no-load condition) to P_{cr} with 20 N load increments and a pause for 2 min after each load increment (Fig. 5.31b). The procedure on similar lines is followed for all the printed cupons.

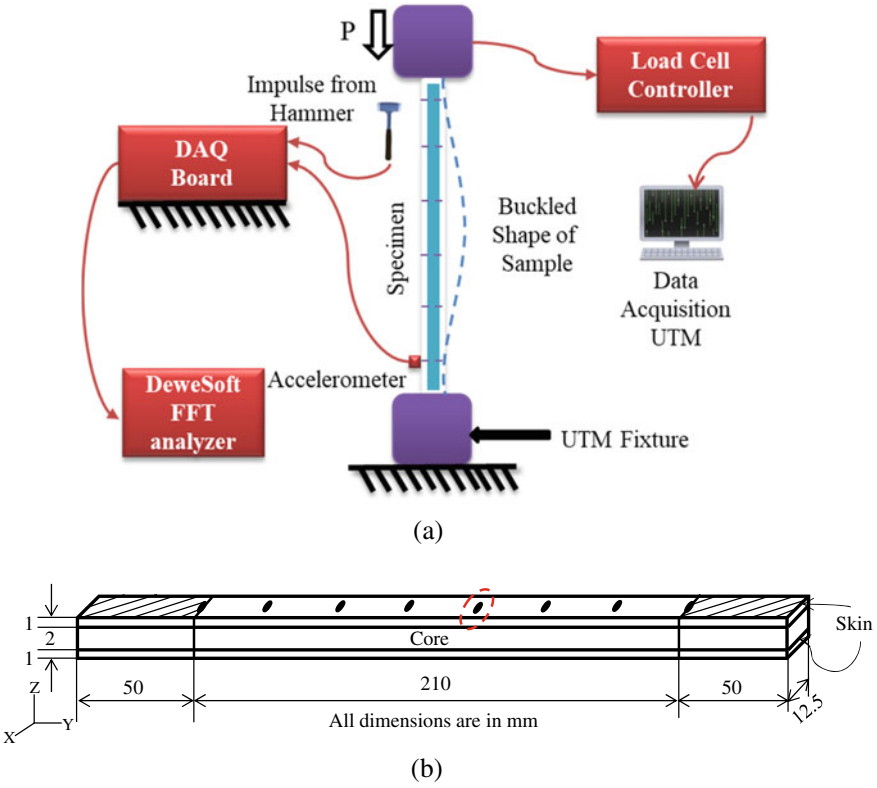

Fig. 5.31 **a** Setup schematics and **b** cupon dimensions [36]

5.2.1.8 Buckling Behavior

As shown in Fig. 5.32, the printing parameters employed to create a continuously printed sandwich produce distinct parallel layers with no flaws.

It has been discovered that high-quality samples can be printed with the right printing conditions (Table 4.6). Intact GMBs are uniformly disseminated in HDPE, as shown in Fig. 5.33a. Figure 5.33b shows micrographs of SH60 taken across the sample's thickness, exhibiting a smooth interface and complete diffusion between the skin–core interface with no delamination or layer movement. The foam core is a three-phase structure due to the creation of voids (HDPE, GMB, and voids). The vacuum content rises as GMB concentration rises, possibly because of residual microporosities between the two adjacent layers. Because the MFI is smaller, raster gaps will be larger at greater filler values, resulting in more vacant content. These gaps could operate as extra cushioning zones, improving damping and reducing weight in different ways with foam alone might not be possible.

As illustrated in Fig. 5.31a, the concurrently 3D produced tidy high density polyethylene and sandwiches are subjected to axial compressive loads through UTM with a boundary condition (clamped–clamped). The deflections along the sandwich axis are measured using the DAQ. For P_{cr} estimations, MBC and DTM are applied to load–deflection plots (Fig. 5.34a and Table 5.15). With increased GMB content, the sandwich buckling load increases. This is owing to the undamaged GMB particles increasing the sandwich's overall stiffness and providing smooth bonding between the skin and the core. During the buckling test, the concurrently produced sandwiches showed global buckling mode, with the maximum deflection reported at the midsections without skin wrinkling, delamination, or skin microbuckling (Fig. 5.34c). This is due to HDPE skin's low magnitude of compressive stresses compared to HDPE's microbuckling and wrinkling strength [54]. The most prevalent mechanism of sandwich structure failure under compression is skin delamination, which is absent for printed sandwiches all at once, indicating a very good seamless connection between the skin and core, as illustrated in Fig. 5.33b. The bottom and upper bounds P_{cr} are shown in Table 5.15, which vary between 8.4 and 2.41% for SH20–SH60. In DTM and MBC, SH20–SH60 showed a considerable load enhancement of 39.95–96.55% and 37.37–104.18%, respectively, when compared to H. The P_{cr} of SH60 is raised by 40.43% by the DTM approach and 48.66% by the MBC method when compared to SH20 in sandwiches. Figure 5.34b shows and compares the P_{cr} of printed representative H20 and SH20.

Fig. 5.32 Concurrently 3D printed representative SH60 [36]

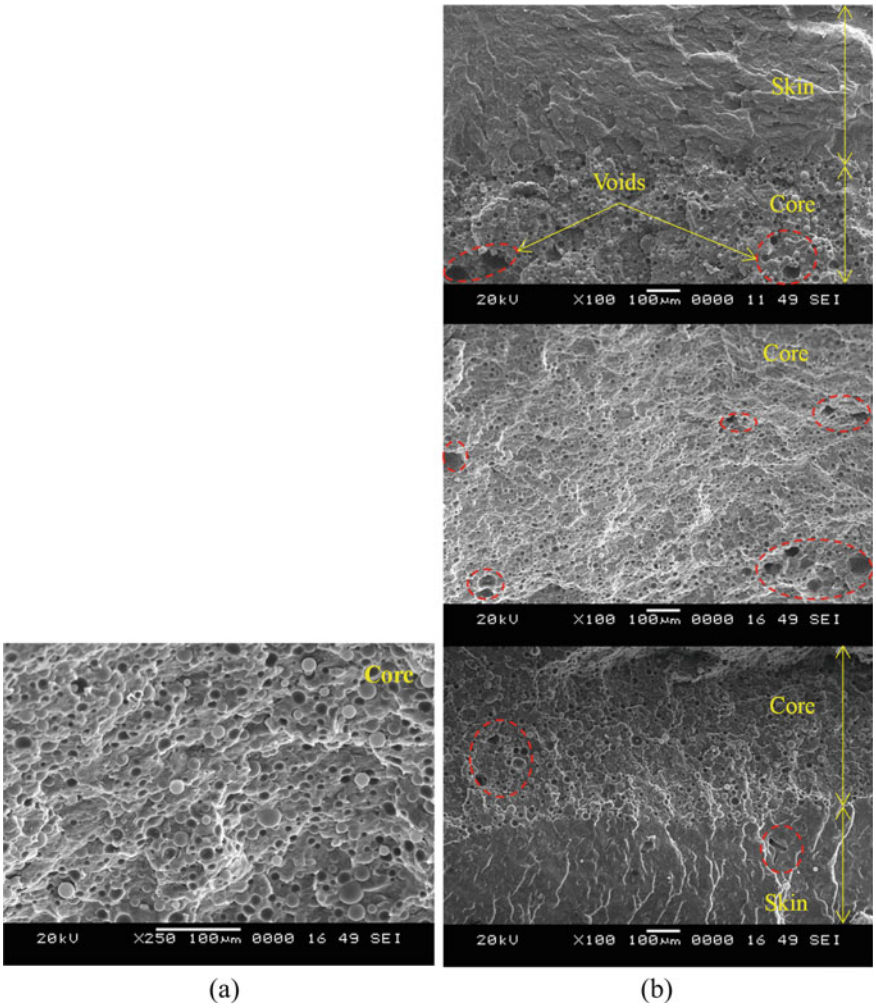

Fig. 5.33 SEM of **a** SH20 core and **b** all in one go printed SH60 [36]

Table 5.16 shows that P_{cr} H20–H60 rose in DTM and MBC by 5.73 and 3–78%, respectively when compared to H. This means that stronger GMB additions increase the SF core's buckling load dramatically. Furthermore, in DTM and MBC approaches, the P_{cr} of SH20–SH60 is increased by 33.31, 12.53, 13.74%, and 33.35, 14.59, 15%, respectively, when compared to the comparable H20–H60. P_{cr} is significantly improved in SH20 compared to SH60 among printed sandwiches, which could be attributed to the smaller void contents in SH20 compared to SH60 (Table 5.6). Furthermore, voids in the buckled zone may elongate more under the applied load, reducing the percent improvements. Despite this, SH60 had the highest P_{cr}.

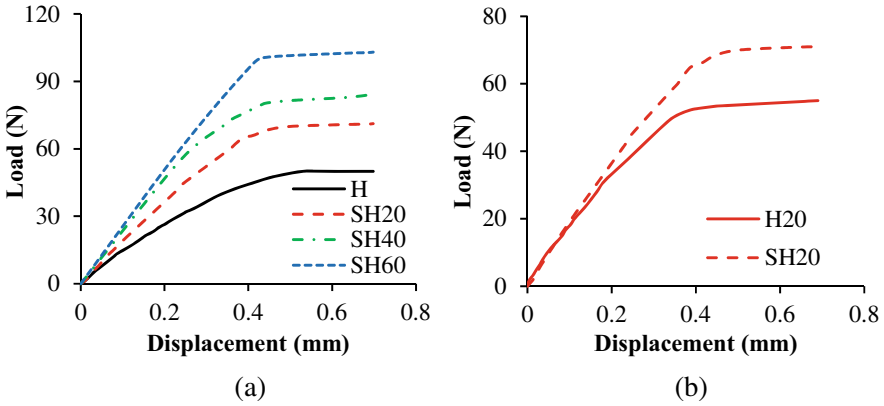

(c)

Fig. 5.34 **a** Printed HDPE and sandwich composites, **b** H20, SH20 comparison, and **c** buckled SH60 cupon [36]

Table 5.15 P_{cr} of sandwiches [36]

Material	$P_{cr}(N)$	
	MBC	DTM
SH20	64.56 ± 1.75	69.98 ± 2.80
SH40	73.78 ± 2.49	76.85 ± 3.52
SH60	95.97 ± 2.86	98.28 ± 3.74

The overall increase in P_{cr} can be attributed to unbroken GMBs, a defect-free skin–core interface, the absence of delamination between layers, and the absence of shear failure, all of which are related to the simultaneous printing of SF-cored sandwiches.

5.2.1.9 Free Vibration Response

The FEA is used to do the numerical Eigen buckling, and modal analysis of 3D printed foam cored sandwiches [34, 44]. For frequency and load calculations, the elastic moduli and Poisson's ratio of the core and skin are also estimated. The Bardella–Genna model is used to determine the core modulus of HDPE and GMB/HDPE [55]. Poisson's ratio for HDPE is taken to be 0.425 [14], whereas Poisson's ratio for GMB is taken to be 0.25 [40]. Using the rule of the mixing, Poisson's ratio of GMB/HDPE core is calculated as follows:

$$\vartheta_{12} = \vartheta_m V_m + \vartheta_f V_f. \tag{5.33}$$

The stages shown in Fig. 5.35a are used to compare the numerical forecasts with experimental results. The homogenization method from the Bardella–Genna models, based on the volume percentage and radius ratio, is used to compute the elastic characteristics of SFs [55]. Using four-noded SHELL181 elements, the sandwich is depicted as a layered entity (Fig. 5.35b). Sandwich's skin and core are modeled as isotropic layers with distinct material properties.

Compressive load and displacement boundary condition are used. The first three natural frequencies of the sandwiches obtained from numerical modal analysis predictions are compared with the experiment in the absence of axial compressive stress. The natural frequency is calculated by resolving the eigenvalue problem, and its experimental values are compared. Utilizing finite element analysis software, the non-linear buckling analysis is performed (ANSYS). The basic buckling modes of sandwiches are initially derived from an investigation of linear eigenvalue buckling. Additionally, the basic buckled mode shape and a chosen geometrical imperfection factor are fed into the non-linear analysis to produce the load–deflection curves. The geometrical imperfection factors control the load–deflection curve that was derived statistically (SH20: 0.001, SH40: 0.00015, and SH60: 0.0001). S stands for sandwich.

DEWETRON is used to accomplish the experimental modal analysis. Figure 5.36 shows the FRF curve, for example, SH20 samples. In addition, the experimental frequencies are compared to those derived using FEA numerical modeling. The first three experimental sandwich natural frequencies are listed in Table 5.17 as a function of applied axial compression. GMBs increase sandwich frequencies because their homogeneous distribution in HDPE boosts structural stiffness. Figure 5.37 shows a decreasing frequency trend as compression increases. It is also noted that near the closest point of P_{cr}, the frequency rapidly declines, resulting in lesser structural stiffness. When the applied load approaches P_{cr}, the fundamental frequencies of the sandwich approach a minimum and then abruptly increase beyond it due to improved

Table 5.16 P_{cr} computations through MBC and DTM [36]

Syntactic foam	$P_{cr}(N)$		Sandwich	$P_{cr}(N)$		% Increase in sandwich wrt core (DTM)	% Increase in sandwich wrt core (MBC)
	DTM	MBC		DTM	MBC		
H	50 ± 1.5	47 ± 1.3	–	–	–	–	–
H20	52.5 ± 2.4	48.41 ± 1.8	SH20	69.98 ± 2.80	64.56 ± 1.75	33.30	33.36
H40	68.3 ± 3.5	64.39 ± 2.6	SH40	76.85 ± 3.52	73.78 ± 2.49	12.52	14.58
H60	86.4 ± 3.4	83.45 ± 2.2	SH60	98.28 ± 3.74	95.97 ± 2.86	13.75	15.00

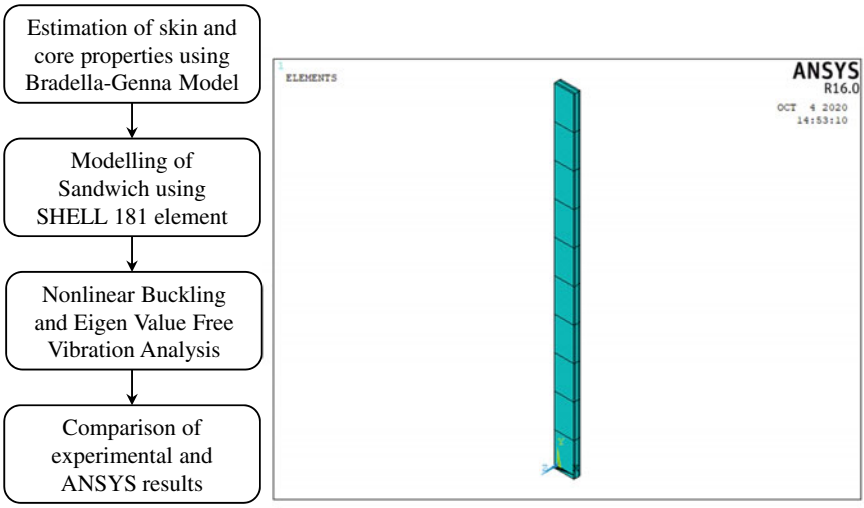

Fig. 5.35 **a** Analysis procedure and **b** Sandwich FEA model [36]

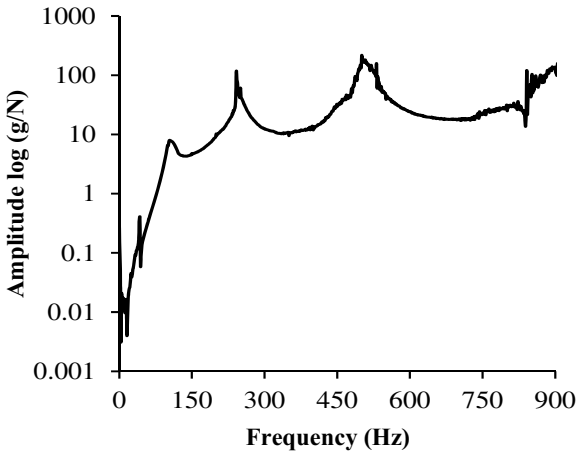

Fig. 5.36 FRF response of SH20 under compression [36]

structural stiffness due to post-buckling geometric deformation (Fig. 5.37). Similar observations have been published in [44, 56, 57].

5.2.1.10 Comparative Analysis

The Bardella–Genna method is used to get the elastic characteristics of HDPE and GMB-based SF (Table 5.18), which are then used as FEA inputs. Table 5.18 shows the

Table 5.17 Natural frequency of prints [36]

Material	Mode	Load (N)						
		0	20	40	60	80	100	120
H	1st	93.3	75.5	65.8	105.5	P_{cr}= 52 N		
	2nd	260.2	255.6	230.5	210.8			
	3rd	517.8	498.8	485.2	450.8			
SH20	1st	119.5	106.8	100.5	90.5	135.7	P_{cr}= 73 N	
	2nd	296.7	265.8	230.7	208.5	200.6		
	3rd	583.5	550.8	528.7	480.5	430.8		
SH40	1st	126.6	110.3	103.2	98.8	127.8	P_{cr}= 80 N	
	2nd	308.2	279.5	245.8	215.9	195.8		
	3rd	632.6	590.8	560.5	498.5	384.5		
SH60[a]	1st	138.2	120.8	112.4	104.2	100.8	98.3	155.8
	2nd	326.4	290.8	265.7	248.8	230.5	217.8	211.7
	3rd	698.2	660.5	615.8	585.6	540.2	464.7	452.8

[a] P_{cr} = 102 N

computed elastic properties of HDPE and sandwiches. Initially, the geometrical flaws are accounted for by the basic buckling mode obtained from the linear eigenvalue buckling estimations. The load–deflection curve is then used to derive the numerical buckling load using non-linear structural analysis. Figure 5.38 shows the numerical load–deflection and experimental curves for sandwiches. The experimental and numerical buckling loads of sandwiches are shown in Table 5.19. SH20's first buckling phase is seen in Fig. 5.39. According to the study, the largest difference between experimental and numerical buckling results is 10.29%. Due to well-diffused layers resulting in improved stiffness in concurrent printing, the experimentally evaluated results in Table 5.19 are higher than the computational predictions. In ANSYS, the natural frequencies of the first three sandwich modes are extracted under no-load conditions using modal analysis. Table 5.20 summarizes the findings. Both the numerical and experimental results are found to be in good agreement. The sandwich cores that were 3D printed at the same time had higher buckling and natural frequencies than the SF cores. Concurrent printing of lightweight sandwiches is effectively shown in this study, opening new paths for 3D printing complex-shaped integrated sandwich structures.

5.3 Acoustic Tests

The five models were created using AUTOCAD, which provides more flexibility for 3D and 2D drawings compared to other solid modeling packages like CREO, SOLIDWORKS, and SOLIDEDGE. The five models were each 96 mm in diameter,

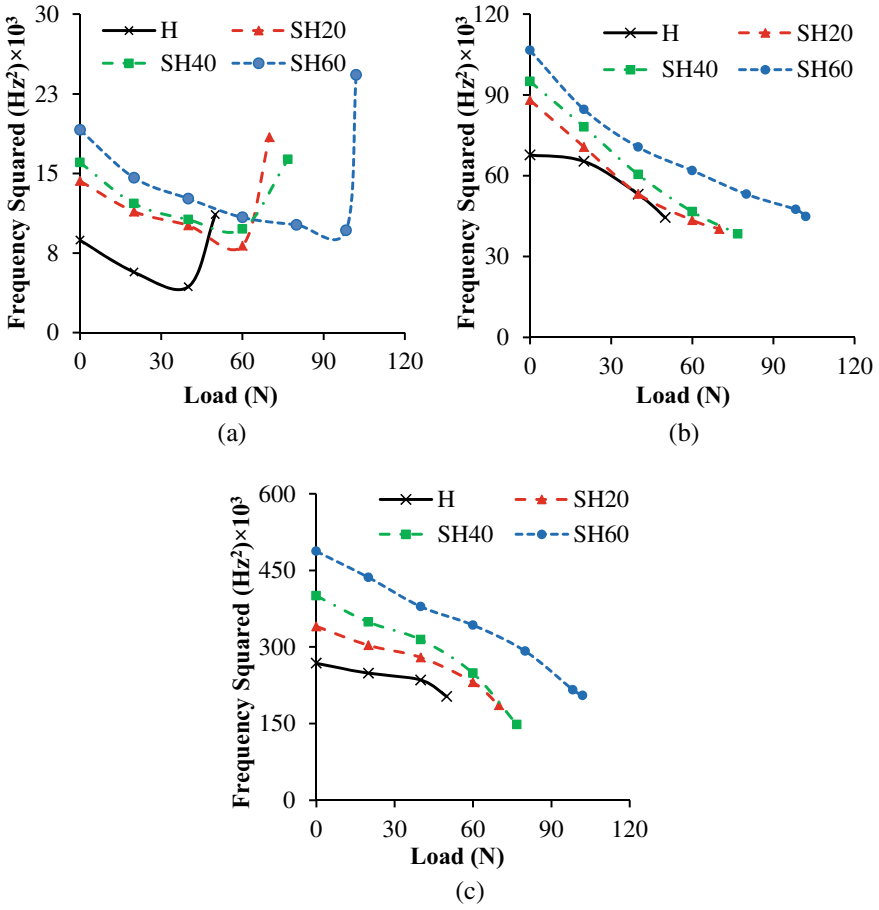

Fig. 5.37 Axial compressive influence on the natural frequency of **a** 1, **b** 2 and **c** 3rd modes [36]

Table 5.18 Modulus computations by Bardella–Genna model [36]

Material	Moduli (MPa)	Poisson's ratio
H	970.05	0.425
H20	1012.6	0.382
H40	1376.1	0.339
H60	1874.1	0.296

10 mm thick, and had holes that were 1 and 8 mm in diameter, respectively. The file was changed to the common .stl format and placed into SIMPLIFY 3D, a slicer program, to create the g-code needed to 3D print the model. The slicer software divides the solid into many uniformly thick layers and provides a simulation of

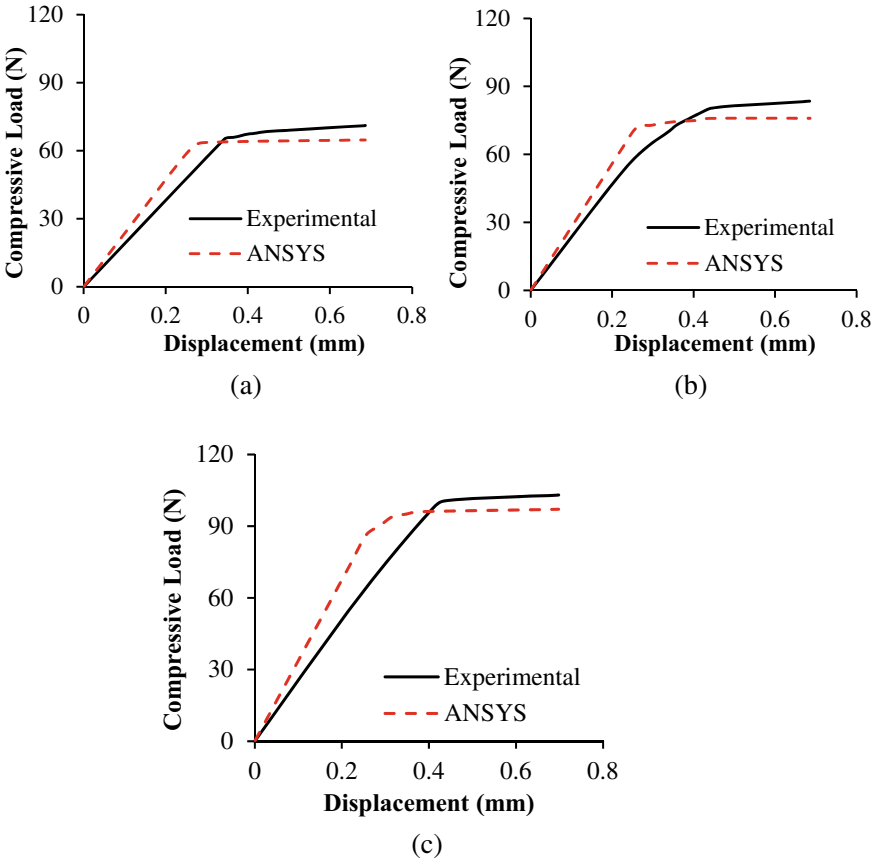

Fig. 5.38 Experimental and ANSYS comparative plots for **a** SH20, **b** SH40 and **c** SH60 [36]

Table 5.19 P_{cr} using numerical and experimental routes [36]

Material	Experimental (N)		Numerical (N)		Numerical and experimental predictions deviations (%)	
	DTM	MBC	DTM	MBC	DTM	MBC
SH20	69.98 ± 2.80	64.56 ± 1.75	63.45	61.70	10.29	4.64
SH40	76.85 ± 3.52	73.78 ± 2.49	74.15	71.85	3.64	2.69
SH60	98.28 ± 3.74	95.97 ± 2.86	94.08	89.85	4.46	6.81

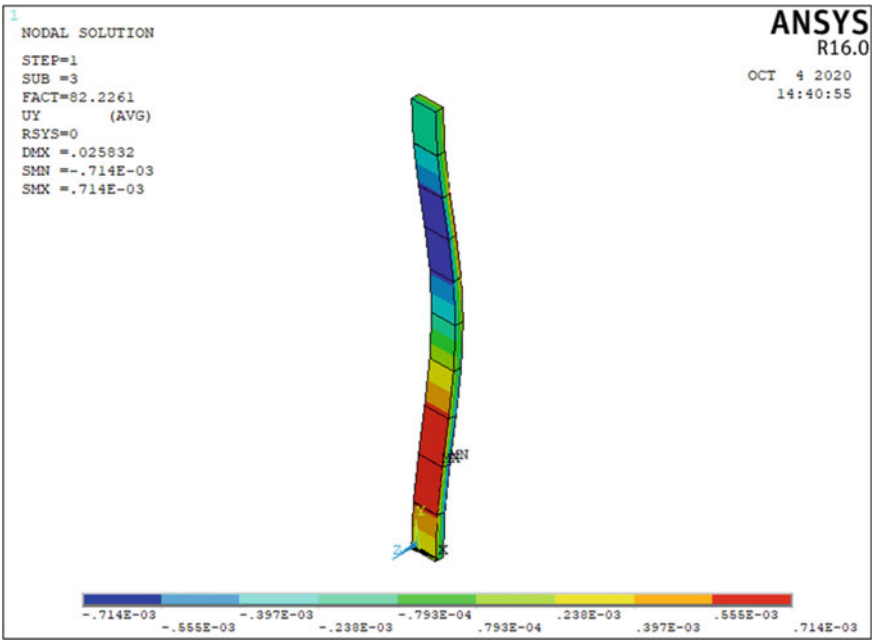

Fig. 5.39 1st buckling mode shape of SH20 [36]

Table 5.20 Natural frequency at zero load condition [36]

Material	Mode	Natural frequency (Hz)	
		Experimental	Numerical
SH20	1st	119.5	110.43
	2nd	296.7	287.45
	3rd	583.5	583.18
SH40	1st	126.6	117.16
	2nd	308.2	319.03
	3rd	632.6	678.70
SH60	1st	138.2	137.45
	2nd	326.4	358.74
	3rd	698.2	793.81

printing so that we may validate the process' correctness and improve the printing process.

Table 5.21 Typical parameters and their values considered for numerical analysis

Criterion	Typical value
Max. frequency in the model	3500 Hz
Incident wave angle	0°
Domain width (W)	0.2 m
Air domain height (H)	0.4 m
Air dynamic viscosity	1.8×10^{-5} Pa-s
Velocity of sound in air	343 m/s

5.3.1 Impedance Tube Method

Five models were put to the test for sound absorption in an impedance tube at Vellore Institute of Technology in Chennai. Based on the transfer function theory, the sound absorption of MPP is investigated in an impedance tube. The experiment is conducted in accordance with ASTM Standard E-1050, and a nominal diameter of 100 mm tube is selected to conduct the test for the targeted frequency range of 200–2000 Hz. Random incidence of two and a half inches Through an 8 channel M + P Vibpilot data gathering system, Microtech Gefell microphones are used to collect white noise signals produced by 16-Ω speakers.

5.3.2 Numerical Analysis

The numerical analysis was conducted using the COMSOL Multiphysics acoustic module, which uses the finite element approach. The software received the CAD model in .iges format after it had already been prepped for 3D printing. The temperature, pressure, and perforation ratio values are 293.15 K, 1 atm, and 0.01, respectively (Table 5.21).

According to the impedance tube output, all specimens except for 8 (which had 8 mm perforations throughout) performed very well in terms of absorption. Except for 8, peak values are at their highest between 0.9 and 0.99 in the following order: 181 > 1 > 18 > 818 >> 8. At the relevant resonance frequency of the specimen, the viscous thermal effects and dissipation are higher in the same order. To increase dissipation, the path's average diameter should be smaller. This assertion is false when peak values of 181 and 1 are contrasted. Therefore, we must conclude that the air column, steep slope, and particularly convergence all contribute to increasing dissipation. The dissipation of sound is affected by the geometrical variations of the perforations in terms of the peak value of the absorption coefficient and frequency bandwidth. The divergent-convergent hole outperformed the constant 1-mm-diameter hole in terms of peak absorption coefficient and bandwidth, according to data shown on the sound absorption coefficient. All the others had lower peak absorption coefficients, but their values were equivalent to those of a 1 mm hole with a constant diameter. To

Table 5.22 Frequency bandwidth for absorption coefficient, $\alpha = 0.75$

Sample	Frequency bandwidth (Hz)
1	210
181	310
18	320
818	350

demonstrate their superiority in absorbing a wider range of frequencies at a higher side, the bandwidths covered by all other holes for a given range of absorption coefficient were higher than the constant 1 mm hole. As a result, convergent-divergent, divergent-convergent, and tapered holes can be utilized in MPPs with performance that is largely comparable, saving both time and material during manufacturing. Maa's design approach may be accurately applied to thick MPPs as well. Additionally, the dissipative effect is improved by placing two 1 mm diameter holes in sequence with a broader air column between them. For all specimens with tapered holes, the peak resonance value has a phase shift to the higher side. As shown in Table 5.22, for them as well, the absorption bandwidth is higher for an absorption coefficient, say over a respectably high absorption coefficient, say 0.75, than for a constant 1-mm-diameter hole. It is practically trending in the opposite direction as the peak absorption coefficient. The ranking is as follows: 818 > 18 > 181 > 1. The pattern demonstrates that the curve flattens and covers a wider range of frequency bandwidth as peak value lowers (Fig. 5.40).

According to the graph, the sample with the 8-mm-diameter hole was a poorer absorber and was not considered for the numerical analysis. For all other sample specimens, there is good agreement between the results of the FEM simulations and the experiments. In every instance, the resonance frequencies are exact matches. Above an absorption value of 0.4, the bandwidths are also closer together. The experimental values are greater at extremely low and high frequencies. This can be the result of assumptions about perfect rigidity and surface smoothness being broken. Practically non-rigid, rough surfaces increase visco-thermal losses, which raises absorptivity. Due to the PLA specimen's comparatively superior surface polish and dimensional precision during 3D printing, however, there was little deviation in either of these areas.

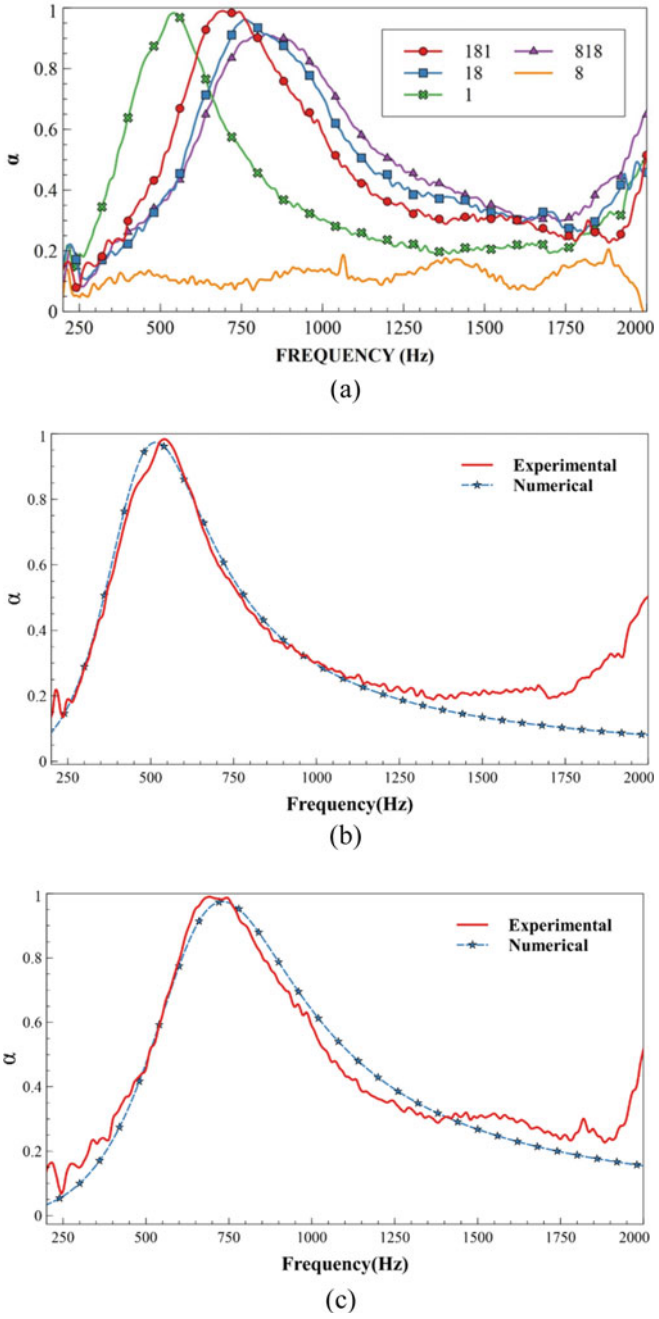

Fig. 5.40 Representative images of **a** sound absorption versus frequency for all the specimens, Numerical and experimental values plotted for **b** 1 mm constant diameter, **c** 1–8–1 mm divergent-convergent and **d** 8–1–8 mm convergent-divergent perforation specimen

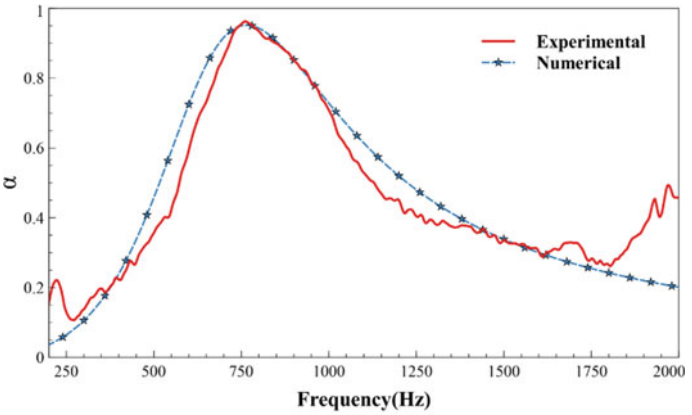

(d)

Fig. 5.40 (continued)

References

1. Lee T, Boey F, Khor K (1995) On the determination of polymer crystallinity for a thermoplastic PPS composite by thermal analysis. Compos Sci Technol 53(3):259–274
2. Divya V, Pattanshetti V, Suresh R, Sailaja R (2013) Development and characterisation of HDPE/EPDM-g-TMEVS blends for mechanical and morphological properties for engineering applications. J Polym Res 20(2):1–11
3. Shaikh H, Anis A, Poulose AM, Alam M, A-Otaibi MN, Alam MA, Al-Zahrani SM (2016) Studies on high density polyethylene reinforced with phosphate ore particles: thermal, rheological, mechanical and morphological properties. Polym-Plast Technol Eng 55(17):1831–1841
4. Bharath HS, Bonthu D, Prabhakar P, Doddamani M (2020) Three-dimensional printed lightweight composite foams. ACS Omega 5(35):22536–22550
5. Wasiak A, Sajkiewicz P, Woźniak A (1999) Effects of cooling rate on crystallinity of i-polypropylene and polyethylene terephthalate crystallized in nonisothermal conditions. J Polym Sci Part B: Polym Phys 37(20):2821–2827
6. Panupakorn P, Chaichana E, Praserthdam P, Jongsomjit B (2013) Polyethylene/clay nanocomposites produced by polymerization with zirconocene/MAO catalyst. J Nanomater 2013:154874
7. Sewda K, Maiti SN (2010) Crystallization and melting behavior of HDPE in HDPE/teak wood flour composites and their correlation with mechanical properties. J Appl Polym Sci 118(4):2264–2275
8. ASTM, Standard test method for coefficient of linear thermal expansion of plastics between – 300 C and 300 C with a vitreous silica dilatometer. D696-13, ASTM International, PA, USA
9. Fitzharris ER, Watanabe N, Rosen DW, Shofner ML (2018) Effects of material properties on warpage in fused deposition modeling parts. Int J Adv Manuf Technol 95(5):2059–2070
10. Baglari S, Kole M, Dey TK (2011) Effective thermal conductivity and coefficient of linear thermal expansion of high-density polyethylene—fly ash composites. Indian J Phys 85(4):559–573
11. Shunmugasamy VC, Pinisetty D, Gupta N (2012) Thermal expansion behavior of hollow glass particle/vinyl ester composites. J Mater Sci 47(14):5596–5604
12. Atagür M, Sarikanat M, Uysalman T, Polat O, Elbeyli İY, Seki Y, Sever K (2018) Mechanical, thermal, and viscoelastic investigations on expanded perlite–filled high-density polyethylene composite. J Elastomers Plast 50(8):747–761

13. Lombardi JL, Hoffinan RA, Waters JA, Popovich D (1997) Issues associated with EFF & FDM ceramic filled feedstock formulation. In: International solid freeform fabrication symposium
14. Kumar BB, Doddamani M, Zeltmann SE, Gupta N, Ramesh M, Ramakrishna S (2016) Processing of cenosphere/HDPE syntactic foams using an industrial scale polymer injection molding machine. Mater Des 92:414–423
15. Jayavardhan M, Kumar BB, Doddamani M, Singh AK, Zeltmann SE, Gupta N (2017) Development of glass microballoon/HDPE syntactic foams by compression molding. Compos B Eng 130:119–131
16. Jayavardhan M, Doddamani M (2018) Quasi-static compressive response of compression molded glass microballoon/HDPE syntactic foam. Compos B Eng 149:165–177
17. Bharath Kumar BR, Doddamani M, Zeltmann SE, Gupta N, Gurupadu US, Sailaja RRN (2016) Effect of particle surface treatment and blending method on flexural properties of injection-molded cenosphere/HDPE syntactic foams. J Mater Sci 51(8):3793–3805
18. Bharath Kumar B, Zeltmann SE, Doddamani M, Gupta N, Gurupadu S, Sailaja R (2016) Effect of cenosphere surface treatment and blending method on the tensile properties of thermoplastic matrix syntactic foams. J Appl Polym Sci 133(35):4381
19. Bharath H, Bonthu D, Gururaja S, Prabhakar P, Doddamani M (2021) Flexural response of 3D printed sandwich composite. Compos Struct 263:113732
20. Patil B, Bharath Kumar BR, Doddamani M (2019) Compressive behavior of fly ash based 3D printed syntactic foam composite. Mater Lett 254:246–249
21. Ugural AC, Fenster SK (2003) Advanced strength and applied elasticity, 4th edn. Pearson education, New Jersey
22. Budiansky B, Fleck NA (1993) Compressive failure of fibre composites. J Mech Phys Solids 41(1):183–211
23. Manalo A, Aravinthan T, Karunasena W, Islam M (2010) Flexural behaviour of structural fibre composite sandwich beams in flatwise and edgewise positions. Compos Struct 92(4):984–995
24. Omar MY, Xiang C, Gupta N, Strbik OM, Cho K (2015) Syntactic foam core metal matrix sandwich composite under bending conditions. Mater Des 86:536–544
25. Allen H (1969) Analysis and design of structural sandwich panels. Pergamon Press, London
26. Ashby MF, Evans A, Fleck NA, Gibson LJ, Hutchinson JW, Wadley HN (2002) Metal foams: a design guide-Butterworth-Heinemann, Oxford, UK, ISBN 0-7506-7219-6, Published 2000, Hardback, 251 pp. Mater Des 1(23):119
27. Steeves CA, Fleck NA (2004) Collapse mechanisms of sandwich beams with composite faces and a foam core, loaded in three-point bending. Part I: analytical models and minimum weight design. Int J Mechan Sci 46(4):561–583
28. Plantema FJ (1966) Sandwich construction: the bending and buckling of sandwich beams, plates, and shells. John Wiley and Sons, New York
29. Triantafillou TC, Gibson LJ (1987) Failure mode maps for foam core sandwich beams. Mater Sci Eng 95:37–53
30. Lingaiah K, Suryanarayana BG (1991) Strength and stiffness of sandwich beams in bending. Exp Mech 31(1):1–7
31. Theotokoglou EE (1996) Analytical determination of the ultimate strength of sandwich beams. Appl Compos Mater 3(5):345–353
32. ASTM, Standard test method for flatwise compressive properties of sandwich cores. C365M-16, ASTM International, PA, USA
33. Waddar S, Pitchaimani J, Doddamani M, Gupta N (2018) Buckling and free vibration behavior of cenosphere/epoxy syntactic foams under axial compressive loading. Mater Perform Charact 7(1):532–546
34. Waddar S, Pitchaimani J, Doddamani M, Barbero E (2019) Buckling and vibration behaviour of syntactic foam core sandwich beam with natural fiber composite facings under axial compressive loads. Compos B Eng 175:107133
35. Bharath H, Sawardekar A, Waddar S, Jeyaraj P, Doddamani M (2020) Mechanical behavior of 3D printed syntactic foam composites. Compos Struct 254:112832

36. Bharath H, Waddar S, Bekinal SI, Jeyaraj P, Doddamani M (2021) Effect of axial compression on dynamic response of concurrently printed sandwich. Compos Struct 259:113223
37. Chen H, Zhao YF (2016) Process parameters optimization for improving surface quality and manufacturing accuracy of binder jetting additive manufacturing process. Rapid Prototyping J 22(3):527–538
38. Timoshenko JMG (2004) Mechanics of materials, 2nd edn. CBS Publishers & Distributors Pvt. Ltd., New Delhi
39. Ahmed TJ, Stavrov D, Bersee HEN, Beukers A (2006) Induction welding of thermoplastic composites—an overview. Comp Part A: Appl Sci Manuf 37(10):1638–1651
40. Tagliavia G, Porfiri M, Gupta N (2010) Analysis of flexural properties of hollow-particle filled composites. Compos B Eng 41(1):86–93
41. Shariyat M (2007) Thermal buckling analysis of rectangular composite plates with temperature-dependent properties based on a layerwise theory. Thin-Walled Struct 45(4):439–452
42. Thomson WT (2008) Theory of vibrations with applications, 5th edn. Pearson Education, India
43. Bokaian A (1988) Natural frequencies of beams under compressive axial loads. J Sound Vib 126(1):49–65
44. Rajesh M, Pitchaimani J (2017) Experimental investigation on buckling and free vibration behavior of woven natural fiber fabric composite under axial compression. Compos Struct 163:302–311
45. Singer JA, Arbocz JA, Weller TA, Cheney JAR (2003) Buckling experiments: experimental methods in buckling of thin-walled structures. shells, built-up structures, composites and additional topics, volume 2. Appl Mechan Rev 56(1):B5
46. Abramovich H, Govich D, Grunwald A (2015) Buckling prediction of panels using the vibration correlation technique. Prog Aerosp Sci 78:62–73
47. Arbelo MA, de Almeida SFM, Donadon MV, Rett SR, Degenhardt R, Castro SGP, Kalnins K, Ozoliņš O (2014) Vibration correlation technique for the estimation of real boundary conditions and buckling load of unstiffened plates and cylindrical shells. Thin-Walled Struct 79:119–128
48. Arbelo MA, Kalnins K, Ozolins O, Skukis E, Castro SG, Degenhardt R (2015) Experimental and numerical estimation of buckling load on unstiffened cylindrical shells using a vibration correlation technique. Thin-Walled Struct 94:273–279
49. Souza M, Assaid L (1991) A new technique for the prediction of buckling loads from nondestructive vibration tests. Exp Mech 31(2):93–97
50. Waddar S, Jeyaraj P, Doddamani M (2018) Influence of axial compressive loads on buckling and free vibration response of surface-modified fly ash cenosphere/epoxy syntactic foams. J Compos Mater 52(19):2621–2630
51. Goel MD, Bedon C, Singh A, Khatri AP, Gupta LM (2021) An abridged review of buckling analysis of compression members in construction. Buildings 11(5):211
52. Tuttle M, Singhatanadgid P, Hinds G (1999) Buckling of composite panels subjected to biaxial loading. Exp Mech 39(3):191–201
53. Matsunaga H (1996) Free vibration and stability of thin elastic beams subjected to axial forces. J Sound Vib 191(5):917–933
54. Corigliano A, Rizzi E, Papa E (2000) Experimental characterization and numerical simulations of a syntactic-foam/glass-fibre composite sandwich. Compos Sci Technol 60(11):2169–2180
55. Bardella L, Genna F (2001) On the elastic behavior of syntactic foams. Int J Solids Struct 38(40):7235–7260
56. Mirzabeigy A, Madoliat R (2016) Large amplitude free vibration of axially loaded beams resting on variable elastic foundation. Alex Eng J 55(2):1107–1114
57. Wu H, Kitipornchai S, Yang J (2015) Free vibration and buckling analysis of sandwich beams with functionally graded carbon nanotube-reinforced composite face sheets. Int J Struct Stab Dyn 15(07):1540011

Chapter 6
Additive Manufacturing of Meta-materials

Metamaterials are three-dimensionally architected materials whose properties are influenced by their intrinsic topological structure and their bulk properties [1]. Mechanical metamaterials are man-made structures with customized mechanical properties governed by rationally planned architectures rather than chemical compositions. As a result, metamaterials are a unique class of designed materials with known constituent materials. These materials are commonly categorized into different types based on the properties that can be controlled by their design. The properties like mechanical [2–5], thermal [6–8], optical [9–11], electronics [12], acoustic [13, 14], and transport [15, 16] can be controlled using meta-structures. Incorporating the geometrical structures inside materials is a new level of expanding the materials design potential significantly. Meta-structures are well-known for their adaptability and toughness in many structural engineering applications [17]. The components for commercial manufacturing, such as meta-structures, can be created and incorporated using three-dimensional (3D) printing [18]. 3D printing technology [19, 20] has recently drawn a lot of focus for fabricating metamaterials. It has facilitated the rapid and low-cost fabrication of metamaterials with complicated geometries and shapes. Some of the most difficult aspects of any metallic or non-metallic material are its flexibility, durability, and mechanical efficiency. As a result, a meta-structure-based manufacturing strategy is required in a variety of engineering applications. Most of the reported metamaterials are manufactured from thermoplastic polymers, which can withstand higher deformations [21–25]. It is essential to understand that these polymers can have viscoelastic properties that impact mechanical properties, particularly under loading conditions [26]. Porosity, anisotropy, in-plane and out-of-plane thickness variation, voids, and weakly adhered or misaligned joints are some types of defects, flaws, and discontinuities that occur during manufacturing thermoplastic-based meta-structures. Hence, a new class of thermosetting-based material systems using 3D printing must be designed to overcome the problems associated with thermoplastics. Syntactic foam-based thermosetting polymers are one of the best options for replacing metallic structures that have been used in many structural engineering applications because of their lower cost, high mechanical strength, great flexibility,

M. Doddamani et al., *3D Printing of Composites*, Materials Horizons: From Nature to Nanomaterials, https://doi.org/10.1007/978-981-99-1730-3_6

and lightweight properties. Syntactic foams have a low density and a high specific strength due to the closed-cell nature due to the lighter weight of the hollow spherical particles. Hence, such materials are employed in a variety of applications that need low water absorption, long-term hydrostatic pressure resistance, buoyancy, and high impact resistance [27, 28]. The most prominent materials in syntactic foams are glass microspheres/microballoons/glass bubbles. The high compressive strength relative to other microspheres means that glass microspheres with diameters ranging from 10 to 300 μm are the preferred syntactic foam materials. 3D printing technologies have considerable potential for fabricating thermosetting-based syntactic foam components with complex geometries without tooling. Further from the incredible design flexibility, 3DP also has minimal capital costs and quick design to application process benefits. The fused filament fabrication (FFF) technology is most widely used to develop polymer matrix syntactic foams [29]. But developing syntactic foams through FFF also has some problems like large porosity, poor strength, weak layer adhesion, temperature sensitivity, and the multistep production process. Thermosetting polymers with superior structural stability can be manufactured without using filaments since material melting is not required for printing [5, 30, 31]. Creating new meta-structures through 3D printing might bring valuable changes in many structural engineering applications. Further, the meta-structure also aids in the creation of self-adaptive structures to enhance 4D printing applications [32]. The most common polymer system in syntactic foams is epoxy–hardener resin [33–37]. Tensile properties [38, 39], impact resistance [40], flexure strength [41, 42], flame retardant properties [43], compressive strength [44–46], heat insulation performance [47–49], electromagnetic shielding properties [50], friction properties [51, 52], dielectric properties [53, 54], and sound absorption properties [55] are among the many superior properties of epoxy-based syntactic foams. In marine applications, epoxy-based syntactic foam density and compressive strength are more valuable properties. Lower density can help improve buoyancy, whereas high strength can help adapt to the deeper sea. The syntactic foam must survive the immense pressure of the water by providing proper buoyancy for the construction equipment. An epoxy–hardener system, hollow glass microballoons, and additional fillers make up the multiphase epoxy-based syntactic foams. Only a certain approach can properly combine different components with meeting the epoxy-based syntactic foam composites' high strength and lightweight goals. The preparation method has a big impact on the characteristics of epoxy-based syntactic foam composites. Furthermore, large shear forces and high pressures during the formation process should be avoided because of the thin microsphere shells.

Metamaterials may have various qualities depending on the use for which they are being developed. Metamaterials are no longer restricted by the requirement of having negative permittivity and/or permeability. Instead, they are referred to as "left-handed materials" or "negative-index metamaterials". Now, it is recognized that metamaterials are made to have unusual features that are not present in natural materials. Building effective metamaterials and applying them to feasibly ground-breaking applications in antenna and radar design, subwavelength imaging, and invisibility cloak design occupied a significant portion of the work in the societies of electrical

engineering, material science, physics, and optics. Metamaterial structures and met surfaces may offer high controllability of the electromagnetic properties; however, the former approach has not yet been applied to address this issue. We suggest approaches to reroute electromagnetic fields and present a design approach using the design flexibility offered by metamaterials.

The commercialization phase is currently replacing the early development phase of metamaterials. By using additive manufacturing processes, it has proven possible to combine specific material properties with intricate internal architectural elements, speeding up the manufacture of metamaterials. The example study found that the internal structure with various infill patterns considerably impacted flexural strength. In practically every field of engineering and general-purpose product development, thermoplastic materials have been crucial to creating metamaterials. The widespread usage of thermoplastics as the primary building block of metamaterials is primarily due to its ease of recycling, handling, low toxicity, and molding flexibility. The scope of future development includes efforts to improve the resolution of 3D printers to boost the precision of metamaterials and post-processing of 3D printed components. The production of composite materials has also been made easier by additive manufacturing. The screw extrusion method allows for the blending of additives with thermoplastics to create materials with distinctive features. Typical manufacturing techniques use injection molding technology for plastic and polymer materials and casting and machining equipment for metals. Due to their low cost, high material flexibility, and ease of machining, researchers initially used polymer-based materials to create innovative structures. Some of the prototypes produced by architects and modular and reconfigurable buildings are examples of traditional methods for fabricating metamaterials, which are often made on a large scale. Mother Nature is a singular conventional pioneer in developing highly ordered, multiscale architectures; yet, conventional approaches are constrained and cannot be tailored to create customized metamaterials. The creation of multiscale natural constructions could facilitate the development of technologies toward synthetic and adjustable metamaterials.

The multi- and meta-structural designs concept has traditionally derived from the construction field, where it gives greater mechanical performance and macroscopic qualities independent of their composition [17]. Over the last two decades, various investigations have been conducted on meta- and multistructures in construction engineering. Earlier research has employed 3D printing to create functional and non-functional ABS architectures. Both consumer goods and industrial components use thermoplastic polymers. Many of those components have a high level of desire to reduce their weight. Despite extensive research on hollow particle-filled lightweight syntactic foams with thermoplastic matrix, the studies on the morphological, mechanical, thermal, and associated properties of 3D printed thermosetting matrix-based lightweight syntactic foam meta-structures have not yet been explored. As a result, 3D printing investigations for the meta-structure of thermosetting syntactic foam composite metamaterials for various novel structural applications are desirable. The percentage of filler in a matrix can be directly or inversely related to the properties of developed composite materials [56]. Additionally, the interaction

of polymeric chains on the surface of fillers can considerably affect the properties of the composite material [57]. The composition, particle size, wall thickness, and processing fabrication technique should be critically examined to achieve the proper thermosetting polymer composite for a given application. The mechanical, thermal, and electrical properties of foams with vinyl ester and epoxy matrices have been investigated that are synthesized using conventional manufacturing routes [44, 58–60]. Such traditional manufacturing routes for thermosetting-based syntactic foams have serious scalability limitations, multipiece assemblies, and difficulty in realizing geometrically complex integrated and leakproof joints. Modeling and simulation-based research on these materials are available in many literatures that focus on the effect of variables like constituent material interfacial effects, debonding, and particle failure under complex loading scenarios that affect syntactic foam properties. The effect of particle volume fraction on the mechanical characteristics of thermosetting syntactic foams is the focus of the initial investigation [61–63]. Nevertheless, using a combination of GMB volume fraction and wall thickness to regulate the properties of syntactic foams has yielded better results [64] in earlier investigations when processed through conventional processing technologies. 3D printing of such thermosetting foams with meta-structured topology will open many applications across marine, aerospace, and automobile sectors. Most importantly, 3D printing of such thermosetting-based foams leads to design flexibility and single-piece manufacturing resulting in components having enhanced mechanical properties.

A sort of artificial cycle structure called a metamaterial has a unit structural scale substantially smaller than the functional wavelength. Controlling electromagnetic properties and the direction of electromagnetic wave propagation through the design and placement of each unit structure is a popular study area in the field of stealth. Metamaterials are synthetic electromagnetic media with subwavelength-scale structures. They offer optical characteristics that can be precisely controlled on length scales smaller than the wavelength of light. The features of metamaterials that are not seen in nature may be completely surprising. For instance, they make it possible to build super lenses that surpass the diffraction limit. The concept of metamaterials may have the most possibility at far higher frequencies, at optical frequencies, or in the Tera-Hz zone, despite the majority of research to date focusing on microwave frequencies. As they offer novel ways to alter electromagnetic radiation like microwaves, metamaterials are of tremendous interest. Because of their distinct acoustical, electromagnetic, optical, and mechanical properties, metamaterials have tremendous potential for a wide range of applications. The difficulty of conventional architecture to provide the innovative functions provided by metamaterials is another factor fueling the growing interest in the development of metamaterials. Moreover, it has been demonstrated that the metamaterial phenomenon can be used to build energy harvesting technology, particularly in low-intensity energy scavenging. In order to obtain the correct order of response against incident energy, methods include algorithmically ordered building blocks at the submicron level. Additionally, there are many opportunities for energy harvesting due to the simplicity of customizing metamaterials in harmony with energy sources like acoustic, mechanical, optical, and microwave.

References

1. Bertoldi K, Vitelli V, Christensen J, van Hecke M (2017) Flexible mechanical metamaterials. Nat Rev Mater 2(11):17066
2. Berwind MF, Kamas A, Eberl C (2018) A hierarchical programmable mechanical metamaterial unit cell showing metastable shape memory. Adv Eng Mater 20(11):1800771
3. Bückmann T, Stenger N, Kadic M, Kaschke J, Frölich A, Kennerknecht T, Eberl C, Thiel M, Wegener M (2012) Tailored 3D mechanical metamaterials made by dip-in direct-laser-writing optical lithography. Adv Mater 24(20):2710–2714
4. Hedayati R, Leeflang AM, Zadpoor AA (2017) Additively manufactured metallic pentamode meta-materials. Appl Phys Lett 110(9):091905
5. Pierson H, Celik E, Abbott A, De Jarnette H, Gutierrez LS, Johnson K, Koerner H, Baur J (2019) Mechanical properties of printed epoxy-carbon fiber composites. Exp Mech 59(6):843–857
6. Kang S, Cha J, Seo K, Kim S, Cha Y, Lee H, Park J, Choi W (2019) Temperature-responsive thermal metamaterials enabled by modular design of thermally tunable unit cells. Int J Heat Mass Transf 130:469–482
7. Peralta I, Fachinotti VD, Álvarez Hostos JC (2020) A brief review on thermal metamaterials for cloaking and heat flux manipulation. Adv Eng Mater 22(2):1901034
8. Lim T-C (2019) 2D metamaterial with in-plane positive and negative thermal expansion and thermal shearing based on interconnected alternating bimaterials. Mater Res Exp 6(11):115804
9. Zhao Y, Belkin MA, Alù A (2012) Twisted optical metamaterials for planarized ultrathin broadband circular polarizers. Nat Commun 3(1):870
10. Soukoulis Costas M, Wegener M (2010) Optical metamaterials—more bulky and less lossy. Science 330(6011):1633–1634
11. Cai W, Chettiar UK, Kildishev AV, Shalaev VM (2007) Optical cloaking with metamaterials. Nat Photon 1(4):224–227
12. Walia S, Shah CM, Gutruf P, Nili H, Chowdhury DR, Withayachumnankul W, Bhaskaran M, Sriram S (2015) Flexible metasurfaces and metamaterials: A review of materials and fabrication processes at micro- and nano-scales. Appl Phys Rev 2(1):011303
13. Zangeneh-Nejad F, Fleury R (2019) Active times for acoustic metamaterials. Rev Phys 4:100031
14. Cummer SA, Christensen J, Alù A (2016) Controlling sound with acoustic metamaterials. Nat Rev Mater 1(3):16001
15. Wu X, Su Y, Shi J (2019) Perspective of additive manufacturing for metamaterials development. Smart Mater Struct 28(9):093001
16. Surjadi JU, Gao L, Du H, Li X, Xiong X, Fang NX, Lu Y (2019) Mechanical metamaterials and their engineering applications. Adv Eng Mater 21(3):1800864
17. Brun M, Movchan AB, Jones IS (2013) Phononic band gap systems in structural mechanics: finite slender elastic structures and infinite periodic waveguides. J Vibr Acoust 135(4)
18. Matlack KH, Bauhofer A, Krödel S, Palermo A, Daraio C (2016) Composite 3D-printed metastructures for low-frequency and broadband vibration absorption. Proc Natl Acad Sci 113(30):8386–8390
19. Kwok T-H, Wang CC, Deng D, Zhang Y, Chen Y (2015) Four-dimensional printing for freeform surfaces: design optimization of origami and kirigami structures. J Mechan Des 137(11)
20. Momeni F, Liu X, Ni J (2017) A review of 4D printing. Mater Des 122:42–79
21. Restrepo D, Mankame ND, Zavattieri PD (2016) Programmable materials based on periodic cellular solids. Part I: experiments. Int J Solids Struct 100–101:485–504
22. Ren X, Das R, Tran P, Ngo TD, Xie YM (2018) Auxetic metamaterials and structures: a review. Smart Mater Struct 27(2):023001
23. El-Helou C, Harne RL (2019) Exploiting functionally graded elastomeric materials to program collapse and mechanical properties. Adv Eng Mater 21(12):1900807
24. Zhang D, Xiao J, Yu W, Guo Q, Yang J (2018) Hierarchical metal/polymer metamaterials of tunable negative Poisson's ratio fabricated by initiator-integrated 3D printing (i3DP). Nanotechnology 29(50):505704

25. Frenzel T, Kadic M, Wegener M (2017) Three-dimensional mechanical metamaterials with a twist. Science 358(6366):1072–1074
26. Dykstra DMJ, Busink J, Ennis B, Coulais C (2019) Viscoelastic snapping metamaterials. J Appl Mechan 86(11)
27. Avalle M, Lehmhus D, Peroni L, Pleteit H, Schmiechen P, Belingardi G, Busse M (2009) AlSi7 metallic foams–aspects of material modelling for crash analysis. Int J Crashworthiness 14(3):269–285
28. Dou ZY, Jiang LT, Wu GH, Zhang Q, Xiu ZY, Chen GQ (2007) High strain rate compression of cenosphere-pure aluminum syntactic foams. Scripta Mater 57(10):945–948
29. Kumar BB, Doddamani M, Zeltmann SE, Gupta N, Ramesh M, Ramakrishna S (2016) Processing of cenosphere/HDPE syntactic foams using an industrial scale polymer injection molding machine. Mater Des 92:414–423
30. Compton BG, Lewis JA (2014) 3D-printing of lightweight cellular composites. Adv Mater 26(34):5930–5935
31. Hmeidat NS, Kemp JW, Compton BG (2018) High-strength epoxy nanocomposites for 3D printing. Compos Sci Technol 160:9–20
32. Noroozi R, Bodaghi M, Jafari H, Zolfagharian A, Fotouhi M (2020) Shape-adaptive metastructures with variable bandgap regions by 4D printing. Polymers 12(3):519
33. Dando KR, Cross WM, Robinson MJ, Salem DR (2018) Production and characterization of epoxy syntactic foams highly loaded with thermoplastic microballoons. J Cell Plast 54(3):499–514
34. Zeltmann SE, Chen B, Gupta N (2018) Thermal expansion and dynamic mechanical analysis of epoxy matrix–borosilicate glass hollow particle syntactic foams. J Cell Plast 54(3):463–481
35. Yu W, Xue H (2017) Effect of soaking corrosion on flexural properties of carbon fiber reinforced epoxy syntactic foams. Fibers Polym 18(5):971–978
36. Yu W, Xue H, Qian M (2017) Tensile and compressive properties of epoxy syntactic foams reinforced by short glass fiber
37. Zhang X, Ya B, Huang B, Zhou B, Pei L, Jia F (2017) Study on preparation and properties of carbon nanotubes/hollow glass microspheres/epoxy syntactic foam. J Polym Eng 37(1):93–98
38. Gupta N, Nagorny R (2006) Tensile properties of glass microballoon-epoxy resin syntactic foams. J Appl Polym Sci 102(2):1254–1261
39. Bharath Kumar B, Zeltmann SE, Doddamani M, Gupta N, Gurupadu S, Sailaja R (2016) Effect of cenosphere surface treatment and blending method on the tensile properties of thermoplastic matrix syntactic foams. J Appl Polym Sci 133(35)
40. Chen P, Li J, Zhang L (2018) Analysis of mechanical characteristics of fly ash cenospheres reinforced epoxy composites. J Wuhan Univ Technol Mater Sci Edn 33(1):139–145
41. Cavasin M, Giannis S, Salvo M, Casalegno V, Sangermano M (2018) Mechanical and thermal characterization of an epoxy foam as thermal layer insulation for a glass fiber reinforced polymer. J Appl Polym Sci 135(47):46864
42. Saha MC, Nilufar S (2010) Nanoclay-reinforced syntactic foams: Flexure and thermal behavior. Polym Compos 31(8):1332–1342
43. Xiang Y, Wang L, Yang Z, Gao P, Qin S, Yu J (2019) Effect of aluminum phosphinate on the flame-retardant properties of epoxy syntactic foams. J Therm Anal Calorim 137(5):1645–1656
44. Gupta N, Pinisetty D, Shunmugasamy VC (2013) Reinforced polymer matrix syntactic foams: effect of nano and micro-scale reinforcement. Springer Science & Business Media
45. Panteghini A, Bardella L (2015) On the compressive strength of glass microballoons-based syntactic foams. Mech Mater 82:63–77
46. Sankaran S, Ravishankar B, Sekhar KR, Dasgupta S, Kumar MJ (2017) Syntactic foams for multifunctional applications. Composite materials. Springer, pp 281–314
47. Waddar S, Pitchaimani J, Doddamani M (2018) Snap-through buckling of fly ash cenosphere/epoxy syntactic foams under thermal environment. Thin-Walled Struct 131:417–427
48. Gupta N, Pinisetty D (2013) A review of thermal conductivity of polymer matrix syntactic foams—effect of hollow particle wall thickness and volume fraction. Jom 65(2):234–245

49. Robert TM, Nair S, Mathew D, Reghunadhan Nair C (2018) Room temperature processable heat-resistant epoxy-oxazolidone-based syntactic foams. Polym Adv Technol 29(1):121–129
50. Zhang L, Wang LB, See KY, Ma J (2013) Effect of carbon nanofiber reinforcement on electromagnetic interference shielding effectiveness of syntactic foam. J Mater Sci 48(21):7757–7763
51. Manakari V, Parande G, Doddamani M, Gaitonde V, Siddhalingeshwar I, Shunmugasamy VC, Gupta N (2015) Dry sliding wear of epoxy/cenosphere syntactic foams. Tribol Int 92:425–438
52. Shahapurkar K, Chavan VB, Doddamani M, Kumar GM (2018) Influence of surface modification on wear behavior of fly ash cenosphere/epoxy syntactic foam. Wear 414:327–340
53. Singh AK, Shishkin A, Koppel T, Gupta N (2018) A review of porous lightweight composite materials for electromagnetic interference shielding. Compos B Eng 149:188–197
54. Shunmugasamy VC, Pinisetty D, Gupta N (2014) Electrical properties of hollow glass particle filled vinyl ester matrix syntactic foams. J Mater Sci 49(1):180–190
55. Park J, Yang SH, Minn KS, Yu CB, Pak SY, Song YS, Youn JR (2018) Design and numerical analysis of syntactic hybrid foam for superior sound absorption. Mater Des 142:212–220
56. Singh AK, Patil B, Hoffmann N, Saltonstall B, Doddamani M, Gupta N (2018) Additive manufacturing of syntactic foams: part 1: development, properties, and recycling potential of filaments. JOM 70(3):303–309
57. Singh AK, Saltonstall B, Patil B, Hoffmann N, Doddamani M, Gupta N (2018) Additive manufacturing of syntactic foams: part 2: specimen printing and mechanical property characterization. JOM 70(3):310–314
58. Gupta N, Woldesenbet E, Mensah P (2004) Compression properties of syntactic foams: effect of cenosphere radius ratio and specimen aspect ratio. Compos A Appl Sci Manuf 35(1):103–111
59. Gupta N, Ye R, Porfiri M (2010) Comparison of tensile and compressive characteristics of vinyl ester/glass microballoon syntactic foams. Compos B Eng 41(3):236–245
60. Porfiri M, Gupta N (2009) Effect of volume fraction and wall thickness on the elastic properties of hollow particle filled composites. Compos B Eng 40(2):166–173
61. Bardella L, Genna F (2001) On the elastic behavior of syntactic foams. Int J Solids Struct 38(40):7235–7260
62. Rizzi E, Papa E, Corigliano A (2000) Mechanical behavior of a syntactic foam: experiments and modeling. Int J Solids Struct 37(40):5773–5794
63. Huang J, Gibson L (1993) Elastic moduli of a composite of hollow spheres in a matrix. J Mech Phys Solids 41(1):55–75
64. Gupta N, Zeltmann SE, Shunmugasamy VC, Pinisetty D (2014) Applications of polymer matrix syntactic foams. Jom 66(2):245–254

Chapter 7
3D Printing of Industrial Components

Compared to traditional processing methods, 3D printing enables the creation of components without compromising the strength-to-weight ratio. 3D printed SF-based prints and sandwiches open the possibility of more direct industrial applications for geometrically difficult items. Components manufactured with traditional fabrication processes, such as 3D printing syntactic foams, may be able to replace parts made with traditional fabrication techniques, which have limitations in terms of intricate geometries, longer production times, and higher costs. The adoption of 3DP over traditional processing has resulted in a variety of advantages, including the ability to create extremely specialized, complicated structures, cost savings, design freedom, and personalization. The printing method's precision, printing size, and the effect of external elements all influence the accuracy of the 3D printed composite. 3DP helps in printing intricate shapes and precise components with microscale details despite print resolution, surface polish, quality, and layer adhesion challenges. As a result, certain industrial scale components are 3D printed in this study to demonstrate the practicality of produced filaments in 3D printers by focusing on the component's weight. HDPE is the most widely utilized polymer in consumer goods manufacturing. Many present parts can benefit from GMB filled HDPE SFs, which provide a lightweight alternative while also reducing HDPE usage, resulting in a cost-effective proposal.

A reduction in failure strain can be a limiting factor in some applications. Mismatches in particle and matrix CTE, which might result in interfacial separation or material failure, are other essential considerations to address. As a result, new material uses must be carefully explored. Many readily accessible HDPE pieces have been found, and the process parameters employed in this study have been used to print these parts in syntactic foams. Composite density is a critical component in lightweight applications, and the lower density of SFs allows them to be employed in weight-sensitive constructions. According to the findings of this study, H60 has a greater weight-saving potential of 28% when compared to pure HDPE, and the presence of GMB provides resistance to polymer chain flow. Thereby, dimensionally stable foam prints can be produced without any warpage. H60 filament is used to print some of the industrial components as shown in Fig. 7.1.

M. Doddamani et al., *3D Printing of Composites*, Materials Horizons: From Nature to Nanomaterials, https://doi.org/10.1007/978-981-99-1730-3_7

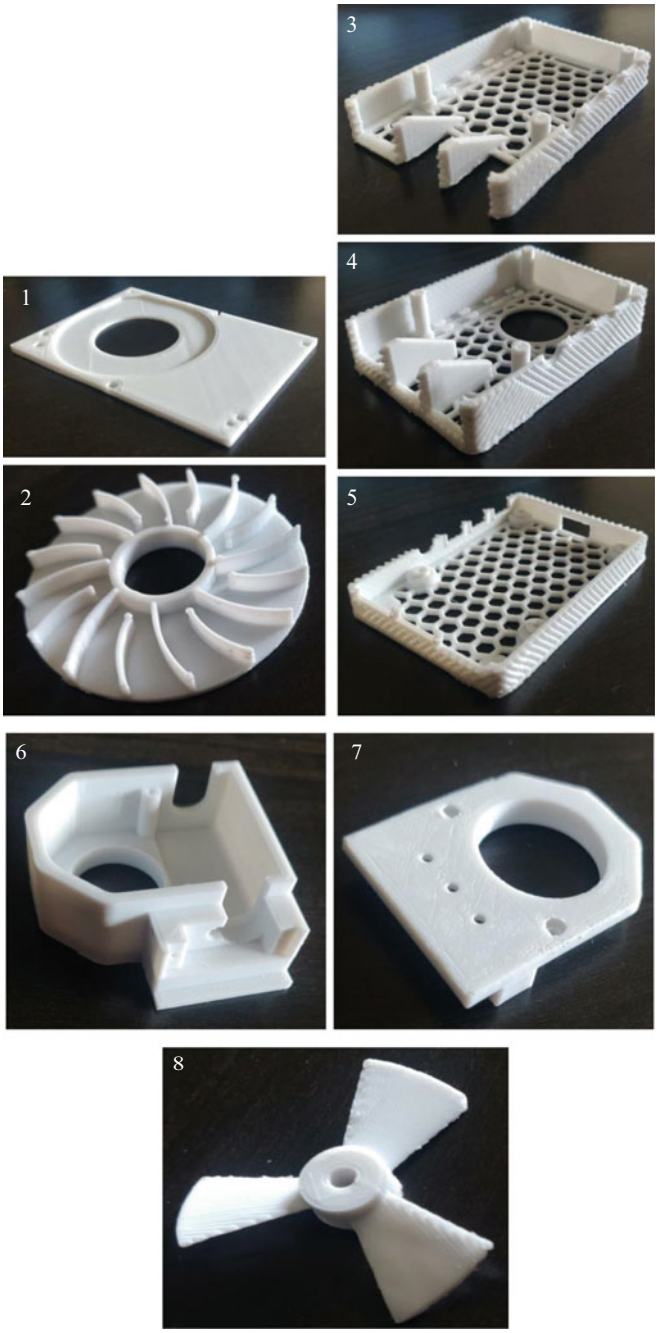

Fig. 7.1 Representative components printed using H60. 1. Hard disk fan cover, 2. hard disk cooling fan, 3. external device connector—top case, 4. external device connector—cooling fan unit, 5. external device connector—lower case, 6. power pac—lower case, 7. power pac—top case and 8. thrust propeller

Table 7.1 Details of 3D printed components

No	Component name	Weight of HDPE component (g)	Weight of H60 component (g)	Weight-saving potential w.r.t HDPE (%)	Average weight-saving potential w.r.t HDPE (%)
1	Hard disk fan cover	236.24	184.03	22.10	21.81
2	Hard disk cooling fan	195.71	152.45	22.10	
3	External device connector—top case	846.73	659.56	22.11	
4	External device connector—cooling fan unit	456.92	355.92	22.10	
5	External device connector—lower case	548.73	440.26	19.77	
6	Power pac—lower case	962.69	749.89	22.10	
7	Power pac—top case	215.03	167.50	22.10	
8	Thrust propeller	268.66	209.27	22.11	

Each of these materials and the effect of manufacturing them with SFs are listed in Table 7.1. Using H60 filament, the parts are 3D printed to lower the component's weight. As demonstrated in Fig. 7.1, complex-shaped, thin-sectioned, delicate details can be produced in large quantities, resulting in lower prices. Apart from the original GMB blend, the main 3D printer settings and characteristics have been kept unchanged, enabling easy industrial adaptation of lighter components. In the eight sections chosen, an average weight-saving potential of 21.8% can be reached using H60 in HDPE.

HDPE is commonly employed in the production of consumer goods. It is possible to identify several present components where cenosphere-filled HDPE syntactic foams could be useful, providing lightweight or reducing HDPE usage to make the part more affordable and environmentally friendly. For some applications, reduction in failure strain is a constraint. Moreover, issues like the gap between the particle's and matrix's coefficients of thermal expansion, which can result in interfacial separation or material failure, might be significant factors. Consequently, choosing the prospective uses of such novel materials is important. These pieces are printed in syntactic foams utilizing 3DP and many existing HDPE components that have improved their process settings. Figure 7.2 shows the 3DP parts using HDPE blended with cenosphere. Figure 7.3 shows close-up images of selected 3DP parts.

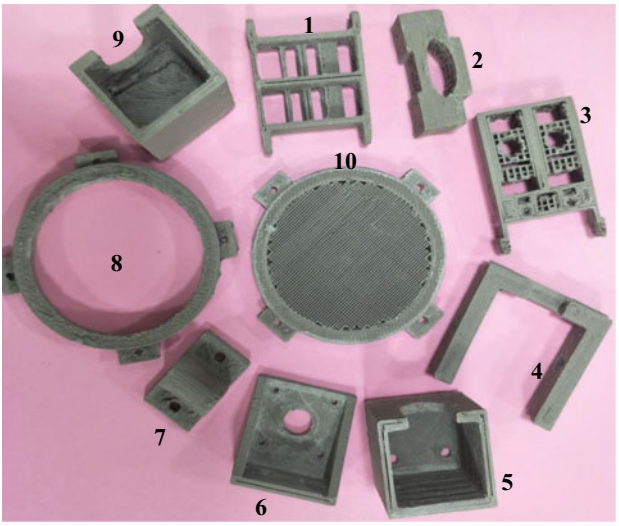

Fig. 7.2 Eco-friendly components printed using 3DP technique. 1. Arduino rack, 2. bearing holder, 3. Arduino rack upper head, 4. support channel, 5. motor mount with filet, 6. motor mount, 7. rod end holder, 8. filter ring, 9. motor cover, 10. filter end cap

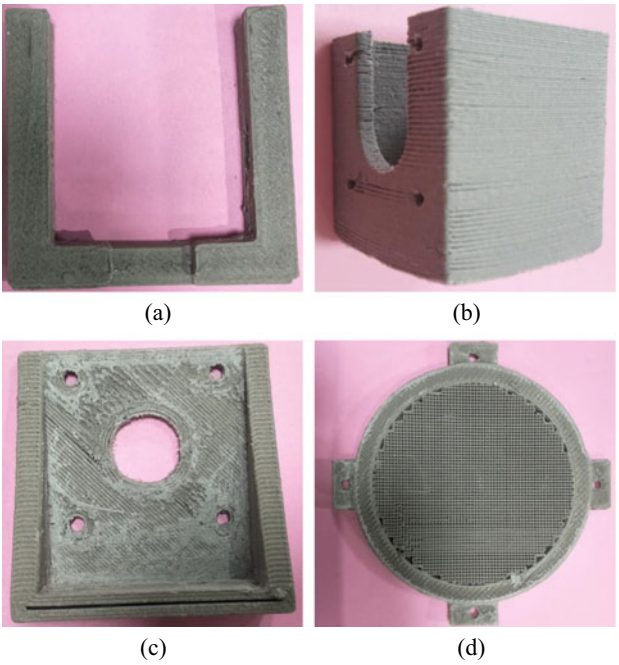

Fig. 7.3 Prototype components printed in the study: **a** Support channel, **b** motor mount with filet, **c** motor mount, **d** filter end cap

Table 7.2 describes each element and the effects of manufacturing them with syntactic foams. The components are 3DP, with the goal of using H60 filament to reduce the product's weight by 8%. Figure 7.3 makes it abundantly evident that complicated parts with complex shapes, and thin sections can be produced in large quantities at cheaper costs. Because of the usage of fly ash, the product is also more environmentally friendly. It should be observed that, except from mixing cenospheres in the initial feed, all other 3D printer options and parameters have been kept unchanged to make it easier for enterprises to adopt lighter components. According to an estimate of the amount of HDPE used in the ten parts, cenosphere utilization can save 4.64 million tons of HDPE globally.

Table 7.2 Details of 3DP syntactic foam components

No.	Component name	Wt. of HDPE component (g)	Wt. of composite component (g)	Wt. saving (%)	Features	Component functionality	Annual total HDPE saving[a]
01	Arduino rack	15.4	14.2	7.8	Thin section, multiple slots in different planes	Fixture for electrical connectors	8%, 4.64 million tons
02	Bearing holder	18.1	16.7	7.7	Thick section, oval-shaped hole	Sustain better torque, support element	
03	Arduino rack upper head	24	22.1	7.9	Thick section, multiple slots in different planes	Connector for robot linkages	
04	Support channel	19.4	17.9	7.7	Thick section with holes	Dimensional stability, bending, and torsional strength	
05	Motor mount with filet	34.8	32.0	8.1	Thin section, with intricate holes	Close dimensional tolerance, fixture for motor	
06	Motor mount	16.72	15.4	7.9	Thin section, with intricate holes	Dimensional and load sustainability	

(continued)

Table 7.2 (continued)

No.	Component name	Wt. of HDPE component (g)	Wt. of composite component (g)	Wt. saving (%)	Features	Component functionality	Annual total HDPE saving[a]
07	Rod end holder	15.3	14.1	7.8	Thick section, with holes	Dimensional stability, good strength	
08	Filter ring	23.5	21.6	8.0	Thick section	Good compressive strength	
09	Motor cover	37.1	34.2	7.8	Thin section, U-shaped slot	Dimensional stability, Support element	
10	Filter end cap	31.2	28.7	8.0	Thin section, complex mesh structure	Dimensional stability, Filtering liquid	

[a]Report on Global HDPE demand to grow 4.2% annually through 2022, March 9, 2015 by Canadian plastics, Toronto, Canada. http://www.canplastics.com/materials/global-hdpe-demand-to-grow-4-2-annually-through-2022-report/1003434693.

Chapter 8
Challenges and Future Trends

When compared to conventional manufacturing methods, additive manufacturing (AM) gives a great deal of design flexibility. The study of AM methods' competitiveness in the industrial sector is gaining interest. Modern technology, such as the fused filament fabrication (FFF) method, provides dependable and affordable alternatives. More material flexibility and the ability to produce goods with geometrical restrictions at low cost and with shorter post-processing times are all benefits of the FFF technology. Because of all these benefits, researchers started looking at mechanical qualities such as part orientation, surface roughness, and dimensional accuracy. More specific stiffness in polymer products created using 3D printing technology based on FFF is available in weight-sensitive components. Hollow GMBs can be strengthened within polymer-based components to reduce their weight significantly. The significant weight reduction potential of SFs broadens its range of automotive and marine applications. Syntactic foams that have been functionally graded have been used in aeronautical structures. Syntactic or closed-cell foams are another name for hollow particle-reinforced composites. Syntactic foam composites were the focus of a lot of studies using various polymers and processing techniques like injection and compression molding. Syntactic foams provide good damping qualities while reducing the component weight by lowering the density.

The structural components gradually degrade through the buckling phenomena while being continuously exposed to compressive strain. The buckling is most frequently seen in thin structures where the yield strength of the composite beams is below. It is crucial to comprehend the buckling behavior of these beams since these constructions are subject to axial compressive stresses. Prestresses brought on by compressive force cause the beams' rigidity to alter. The dynamic behavior of the beams is affected by this variation in rigidity. Hence, a better understanding of mechanical buckling and the dynamic properties of concurrently printed graded syntactic foam under compressive load is required to design and create integrated (joint less/leakproof) structural parts for naval, automotive, and aeronautical applications.

M. Doddamani et al., *3D Printing of Composites*, Materials Horizons: From Nature to Nanomaterials, https://doi.org/10.1007/978-981-99-1730-3_8

GMB-based lightweight composite foam feedstock has been successfully manufactured for use in weight-sensitive applications on a commercial printer. Mechanical characterization tests are conducted on both to determine whether materials and 3D printed samples are adaptable and practical for 3DP applications. The printed sandwich is made from a GMB/HDPE core and HDPE skin. The production of SF filaments involves dispersing GMBs (20–60 vol.%) in HDPE. Investigated is the effect of filament on prints of GMB content. Using the proper extrusion conditions, more foam filaments can be produced with little to no filler breakage. Extruded filaments are put through various mechanical tests while being used as feedstock in a 3D printer to simultaneously create core and sandwich samples. In analyses of property structure and failure mechanism, extensive SEMs are taken. The thesis's findings are given as data comparisons of printed items with relevant printed components from the literature. The property map offered in this thesis is particularly helpful for industry professionals and acts as a reference for choosing the best technique or composition for the intended application.

The development of lightweight feedstock filament was successfully proven in the current work with the goal of increasing the variety of materials accessible for 3D printers that are currently on the market. Complex geometrical components with GMB/HDPE integration can be printed without experiencing warpage, as demonstrated in this work. Future research will concentrate on improving strength through surface modification of the constituent materials and the use of overlapping rasters.

Special composites termed functionally graded materials (FGMs) show property variation along the thickness direction. FGMs exhibit continuous stress distribution compared to laminated composites due to property variation. FGMs have shown their importance in producing beams, plates, and shells by the uniform modulation of material characteristics along the desired direction. These FGMs are frequently utilized in demanding industrial environments, such as gas turbines and aircraft components. Several manufacturing processes, such as solid, powder metallurgy, liquid, and gas-based, are used to process these FGMs. Yet, there has not been much research on creating closed-cell FGMs utilizing additive manufacturing (AM) techniques. While plain composites perform better in weight, strength, and design flexibility, they have the drawback of a sudden transition in their properties, which increases the likelihood of failure.

To address this problem, the Japanese developed functionally graded materials (FGMs) in 1984 as the primary material for aerospace projects. FGMs avoid abrupt property transitions by varying their thermal conductivity, modulus, tensile, flexural strength, density, Poisson's ratio, and other parameters continuously and smoothly. FGMs have specific uses in the automotive and aerospace industries where the material's characteristics must be adapted. For instance, a crash part in a car is set to malfunction at specific loads and energies, dissipating energy away from the occupants. These applications frequently call for the employment of two or more materials with various qualities to function effectively under a wider range of loading situations. FGMs are used in various industries, including aerospace and aeronautics, defense,

the energy sector, the medical industry, civil structures, turbine rotors, nuclear reactors, flywheels, thermal barrier systems, gears, nuclear projects, and electronics and optoelectronics.

A brand-new class of materials known as functionally graded materials (FGMs) was first conceptualized in connection with creating extremely heat-resistant materials for spacecraft. The applications of FGMs have been broadened to various sectors, such as sensor technology, optics, electronics, and magnetics, in addition to enhanced thermal stress relaxation and adhesive capabilities. FGMs have an isotropic thermosetting or thermoplastic polymer matrix with a continuous spatial distribution of one or more components with unique qualities. In this manner, a specific gradient, for instance, in mechanical qualities such as wear resistance or electrical conductivity, can be produced. Functionally graded composite materials fall under a brand-new category of contemporary materials suited for multiple applications due to their specific nature of operational characteristic transition within the material. The spatial direction of the FGM microstructure is always changing. In order to create FGMs, the plasma spray method, electrophoresis, vapor deposition, and powder metallurgy were all extensively employed. Few researchers have generated graded composites of graphite-epoxy resin using the centrifugation approach. This method has proven successful in creating continuous gradient composites. In technical and biomedical applications, composites have a significant potential to raise living standards and productivity. Multiphase structures are frequently categorized as composite materials because they have a matrix, high strength, and high modulus reinforcing fiber. These days, composites are made so that repositioning the nano/microstructure enhances the product's distinctive features. This establishes a foundation for the concept of creating functionally graded materials. FGM has been placed in this category of modern engineering composites where the gradient in contexture/morphology is purposefully created to accommodate a specific application and to attain improved results than the original components.

The improvement of material characteristics and assistance for optimum structural design is currently the main goals of material development operations for FGM and composite materials. There is a pressing need for materials with specialized properties that vary with thickness. FGM can be categorized into continuous or discontinuous gradual changes in composition, depending on the composition stage distribution. Corresponding to that, it can be separated into thin and overall FGM based on production technology. Sandwich structures are frequently employed in the industry of micro-auxiliary frames because of their excellent performance and high strength/weight ratio. Thus, it is essential to investigate more personnel's static and dynamic behavior with FGM, such as beams and plates, in the widespread application of functionally graded materials.

The FGM can function as a more effective core material than the conventional homogenous material since it can modify its mechanical properties with thickness. Using functionally graded cores in sandwich constructions made of composites might lessen impact damage. Modifications to FGMS with gradients in chemical composition, porosity, and microstructure are being made. Functionally graded foam materials (FGFMs) are popular in developing impact and crash resistance systems because

of their lightweight design and exceptional energy absorption capabilities. Naturally, modifying pore size or porosity density produces functionally graded materials. Functionally graded (FG) cores are rapidly being used in sandwich panels because they can lower thermal and residual stresses created between the face sheet and the core material compared to conventional sandwich panels. As a result, FG sandwich structure applications in real-world settings are expanding. The 3DP of HDPE- and GMB-based FGM core, and sandwich composites is the future of the current study.